

**UNIVERSIDADE DE SÃO PAULO
ESCOLA DE ENGENHARIA DE SÃO CARLOS**

Marlon Sproesser Mathias

**Instability analysis of compressible flows over open
cavities by a Jacobian-free numerical method**

São Carlos

2017

Marlon Sproesser Mathias

**Análise de instabilidade de escoamentos compressíveis
sobre uma cavidade aberta por um método numérico sem
formação de Jacobiano**

Dissertação apresentada à Escola de Engenharia de São Carlos da Universidade de São Paulo, para obtenção do título de Mestre em Ciências - Programa de Pós-Graduação em Engenharia Mecânica.

Área de concentração: Aeronaves

Supervisor: Prof. Dr. Marcello Augusto Faraco de Medeiros

| |
|--|
| ESTE EXEMPLAR TRATA-SE DA VERSÃO CORRIGIDA. A VERSÃO ORIGINAL ENCONTRA-SE DISPONÍVEL JUNTO AO DEPARTAMENTO DE ENGENHARIA MECÂNICA DA EESC-USP. |
|--|

**São Carlos
2017**

AUTORIZO A REPRODUÇÃO TOTAL OU PARCIAL DESTE TRABALHO,
POR QUALQUER MEIO CONVENCIONAL OU ELETRÔNICO, PARA FINS
DE ESTUDO E PESQUISA, DESDE QUE CITADA A FONTE.

M431a Mathias, Marlon Sproesser
Análise de instabilidade de escoamentos
compressíveis sobre uma cavidade aberta por um método
numérico sem formação de Jacobiano / Marlon Sproesser
Mathias; orientador Marcello Augusto Faraco de
Medeiros. São Carlos, 2017.

Dissertação (Mestrado) - Programa de Pós-Graduação
em Engenharia Mecânica e Área de Concentração em
Aeronaves -- Escola de Engenharia de São Carlos da
Universidade de São Paulo, 2017.

1. Escoamento compressível. 2. Cavidade aberta. 3.
Método de Arnoldi. 4. Simulação numérica direta. 5.
Modos de Rossiter. I. Título.

FOLHA DE JULGAMENTO

Candidato: Engenheiro **MARLON SPROESSER MATHIAS**.

Título da dissertação: "Análise de instabilidade de escoamentos compressíveis sobre uma cavidade aberta por um método numérico sem formação de Jacobiano".

Data da defesa: 24/11/2017.

Comissão Julgadora:

Resultado:

Prof. Associado **Marcello Augusto Faraco de Medeiros**
(Orientador)
(Escola de Engenharia de São Carlos/EESC)

Aprovado

Prof. Dr. **Bruno Souza Carmo**
(Escola Politécnica/EP-USP)

Aprovado

Prof. Dr. **Daniel Rodriguez Alvarez**
(Universidade Federal Fluminense/UFF)

Aprovado

Coordenador do Programa de Pós-Graduação em Engenharia Mecânica:
Prof. Associado **Gherhardt Ribatski**

Presidente da Comissão de Pós-Graduação:
Prof. Associado **Luís Fernando Costa Alberto**

Acknowledgements

Gostaria de agradecer a todos que tornaram este trabalho possível e contribuíram em seu desenvolvimento, direta ou indiretamente.

À minha família, João Carlos, Sônia e Marcel, que me apoiaram nesta etapa e em todas que a precederam. À minha namorada e melhor amiga, Ana Carolina, que esteve sempre ao meu lado.

Ao meu orientador, Marcello, pelas produtivas conversas e pela orientação que se iniciou com minha IC e continuou até este momento. Aos colegas de laboratório, Christian, Fernando, Filipe, Juan e Mateus, pela companhia no desenvolvimento do trabalho e pelas conversas relacionadas, ou não, à pesquisa. Aos amigos da pós-graduação no Departamento de Engenharia Aeronáutica.

Aos professores Daniel, Elmer, Sávio e Vassilis, que deram valiosas dicas para a continuação da pesquisa.

Ao Conselho Nacional de Desenvolvimento Científico e Tecnológico (CNPq), pelo apoio financeiro por meio do projeto número 134722/2016-7.

E a todos os demais que, de alguma forma, contribuíram para este trabalho.

ABSTRACT

MATHIAS, M. S. **Instability analysis of compressible flows over open cavities by a Jacobian-free numerical method.** 2017. 138p. Dissertação (Mestrado) - Escola de Engenharia de São Carlos, Universidade de São Paulo, São Carlos, 2017.

The influence of the Mach number and the boundary layer thickness over the stability of Rossiter-like modes in a subsonic compressible flow over an open rectangular cavity is studied. This work describes the implementation and use of the relevant computational methods. The most straight-forward way of accessing the stability of a flow is to build the Jacobian matrix of its governing equations and to compute its eigenvalues and eigenvectors. The so called matrix forming methods explicitly compute this matrix and use numerical algorithms to solve its eigenproblem. When the flow grows more complex, the Jacobian matrix may become unfeasibly large. The algorithm implemented here is of the Jacobian-free type, which means that this matrix is not explicitly needed. Therefore, the Arnoldi iteration method is used as all it needs is the ability of multiplying the Jacobian by an arbitrary vector. The algorithm is built in a way that a call to a flow solver is equivalent to this multiplication. The development of this solver is also covered by this work, it is a DNS (Direct Numerical Solver) for the compressible Navier-Stokes equations, which means that no turbulence models are used. High numerical precision is an important requirement as small disturbances, many orders of magnitude smaller than the base flow, must be well resolved. High order spectral like differentiation methods are employed. A validation work is performed for both the DNS and the instability analysis algorithm. Finally, this code becomes a tool to access the effect of a cavity on a boundary-layer flow. Two-dimensional cases are run for various incoming boundary layer thicknesses and Mach numbers. This work focuses on Rossiter modes and the physical phenomena that cause them to be either stable or unstable. Three types of phenomena are checked for their influence in the Rossiter modes: resonance with standing waves; spatial amplification at the mixing layer; and transfer from the flow disturbances to acoustic energy. Finally, the linear stability results are compared to DNS runs, which include non-linear effects. In the current parametric space, it was concluded that the instability at the mixing layer has an important role in selecting the Rossiter modes, while the increased flow to acoustic energy transfer caused by higher Mach numbers influence the mode amplification rate. The resonance with standing waves only plays a small role in this case.

Keywords: Compressible flow. Open cavity. Arnoldi iteration. Direct Numerical Solver. Rossiter modes.

RESUMO

MATHIAS, M. S. **Análise de instabilidade de escoamentos compressíveis sobre uma cavidade aberta por um método numérico sem formação de Jacobiano.**

2017. 138p. Dissertação (Mestrado) - Escola de Engenharia de São Carlos, Universidade de São Paulo, São Carlos, 2017.

A influência do número de Mach e da espessura da camada limite sobre a estabilidade de motos tipo Rossiter no escoamento subsônico sobre uma cavidade aberta retangular é estudada. Este trabalho descreve a implementação e o uso dos métodos computacionais relevantes. O método mais direto para se fazer esta análise de estabilidade se resume a encontrar os autovalores e autovetores da matriz Jacobiana das equações governantes do escoamento. Métodos conhecidos como *matrix-forming* montam essa matriz e usam técnicas numéricas para resolver seu autoproblema. No caso deste escoamento, esta matriz se torna muito grande, a ponto de ser impraticável usá-la, ainda mais considerando os métodos de diferenciação numérica utilizados, que a tornariam uma matriz cheia. Para evitar a formação desta matriz, o método da iteração de Arnoldi é utilizado, uma vez que ele não precisa explicitamente da matriz, mas apenas da capacidade de multiplicar o Jacobiano por vetores arbitrários. O algoritmo é construído de forma que uma chamada do código de simulação do escoamento equivale a esta multiplicação. O desenvolvimento deste código também é mostrado neste trabalho. Se trata de um DNS (*Direct Numerical Solver*) para as equações compressíveis de Navier-Stokes. Para este uso, o código deve ter uma alta ordem de precisão pois perturbações várias ordens de grandeza menores que o escoamento base devem ser resolvidas com precisão. Métodos de diferenciação espacial com alta resolução espectral são usados para que a malha não precise ser tão grande, reduzindo o custo computacional. Um trabalho de validação é realizado, para se ter a certeza de que todos os parâmetros tanto do DNS quanto do método de análise de instabilidade estão bem escolhidos e para se saber quais os passos a serem tomados caso uma precisão maior seja necessária. Por fim, estes códigos são utilizados para se estudar o efeito de uma cavidade sobre a estabilidade do escoamento sobre uma placa plana. Casos bidimensionais são rodados com várias espessuras de camada limite no bordo de ataque da cavidade e com diversos números de Mach. Este trabalho foca nos modos de Rossiter e nos fenômenos físicos que os tornam estáveis ou instáveis. Três tipos de fenômeno são analisados: ressonância com ondas estacionárias; amplificação espacial na camada de mistura; e transferência das perturbações no escoamento para energia acústica. Por fim, os resultados da instabilidade linear são comparados com dados do DNS, que incluem os efeitos não lineares. No espaço paramétrico atual, a instabilidade na camada de mistura age de forma a selecionar os modos de Rossiter presentes, enquanto a maior transferência de energia do escoamento para o campo acústico causada pelo aumento do

número de Mach influencia a taxa de amplificação dos modos. A ressonância com ondas estacionárias tem um papel pequeno neste caso.

Palavras-chave: Escoamento compressível. Cavidade aberta. Método de Arnoldi. Simulação numérica direta. Modos de Rossiter.

LIST OF FIGURES

| | |
|--|----|
| Figure 1 – Illustration of the open cavity flow. | 20 |
| Figure 2 – Neutral stability curves for a $L/D = 2$ and $L/\theta_0 = 52.8$ open cavity as a function of Mach and Reynolds. | 21 |
| Figure 3 – The various regions of a boundary layer transition. | 24 |
| Figure 4 – Illustration of TS waves evolution before transition to turbulence. . . . | 25 |
| Figure 5 – Illustration of the energy flow rate in TS waves. | 26 |
| Figure 6 – Schlieren image of the cavity flow showing its acoustic output. | 30 |
| Figure 7 – Cavity acoustic directivity at Mach 0.05 and Mach 0.1. | 32 |
| Figure 8 – Cavity acoustic directivity at Mach 0.1 for various frequencies. | 32 |
| Figure 9 – Illustration of a mesh, only one node for every four is shown. | 38 |
| Figure 10 – Positions of nodes and their spacing in an example mesh. | 38 |
| Figure 11 – Illustration of the domain and its boundaries. | 39 |
| Figure 12 – Modified wave number for various numerical differentiation schemes. . . | 42 |
| Figure 13 – Close-up of the corner nodes in the domain and the regions considered for derivatives. | 43 |
| Figure 14 – Spectral function for the tenth order low-pass filter. | 47 |
| Figure 15 – Scheme of a three dimensional domain decomposed for a grid of 3x4 processes. | 49 |
| Figure 16 – Flowchart to obtain derivatives of the decomposed domain. | 50 |
| Figure 17 – Flowchart of the Jacobian-free method for computing the flow modes. . | 55 |
| Figure 18 – Flowchart of the interface between the spectral and the spatial parts of the code. | 58 |
| Figure 19 – Flowchart of the Jacobian-free instability analysis implementation. . . . | 59 |
| Figure 20 – Overview of code parallelization. | 59 |
| Figure 21 – Example results from the Residual Algorithm. | 61 |
| Figure 22 – Velocity magnitude and streamlines of the unsteady flow at an arbitrary time. | 65 |
| Figure 23 – Velocity plotted against time at a fixed point in an unsteady case. . . . | 65 |
| Figure 24 – Velocity magnitude and streamlines of the lid-driven cavity baseflow. . | 66 |
| Figure 25 – Velocity magnitude and streamlines of the baseflow. | 66 |
| Figure 26 – Mesh spacing for the convergence analysis. | 68 |
| Figure 27 – Eigenvalues computed for the mesh convergence analysis. | 68 |
| Figure 28 – Eigenfunction of mode 1 for mesh convergence analysis. | 69 |
| Figure 29 – Eigenvalues computed for the domain convergence analysis. | 70 |
| Figure 30 – Eigenfunction of the 9 th mode for different domains. | 71 |
| Figure 31 – Eigenfunction of the 12 th mode for different domains. | 71 |

| | |
|---|----|
| Figure 32 – Eigenfunction modulus of modes 1, 4, 8 and 12 at a fixed height. Dashed lines are for Domain 1 and full lines are for Domain 4. | 72 |
| Figure 33 – Eigenvalues computed for the independence analysis of the disturbance magnitude. | 73 |
| Figure 34 – Eigenfunction of mode 1 for the convergence analysis of the disturbance magnitude. | 74 |
| Figure 35 – Eigenfunction of mode 3 for the convergence analysis of the disturbance magnitude. | 74 |
| Figure 36 – Eigenvalues computed for the convergence analysis of the number of DNS steps. | 75 |
| Figure 37 – Eigenfunction of mode 1 for the convergence analysis of the number of DNS steps. | 75 |
| Figure 38 – Eigenvalues computed for the convergence analysis of the number of Arnoldi iterations. | 76 |
| Figure 39 – Evolution of eigenvalues as the Arnoldi method is iterated. | 77 |
| Figure 40 – Eigenfunction of mode 2 for the convergence analysis of the number of Arnoldi iterations. | 77 |
| Figure 41 – Eigenvalues computed for the domain convergence analysis with more Arnoldi iterations. | 78 |
| Figure 42 – Eigenfunction of the 12 th mode for different domains with more Arnoldi iterations. | 78 |
| Figure 43 – Eigenfunction modulus of mode 12 at a fixed height for two domains and two numbers of Arnoldi iterations. | 79 |
| Figure 44 – Relative eigenvalue error versus total number of time steps for modes 1 to 9. | 81 |
| Figure 45 – Eigenvalues computed for the mesh convergence analysis for various counts of span-wise nodes. | 82 |
| Figure 46 – Eigenfunction of mode 1 for mesh convergence analysis in 3D. | 83 |
| Figure 47 – Isosurfaces of density fluctuation of mode 1 at $\beta = 5.62$ | 84 |
| Figure 48 – Isosurfaces of density fluctuation of modes 12 and 14 at $\beta = 5.62$ when the phase in the span-wise direction is not fixed. | 84 |
| Figure 49 – Evolution of eigenvalues as the Arnoldi method is iterated for the 3D case. | 85 |
| Figure 50 – Evolution of eigenvalues as the Arnoldi method is iterated for the 3D spectral case. | 86 |
| Figure 51 – Least stable eigenvalue as computed by the residual algorithm. | 87 |
| Figure 52 – The first eigenfunction as computed by the residual algorithm. | 87 |
| Figure 53 – Least stable eigenvalue as computed by the residual algorithm for the 3D case. | 88 |
| Figure 54 – The first eigenfunction as computed by the residual algorithm. | 89 |

| | |
|---|-----|
| Figure 55 – Isosurfaces of density of mode 1, comparing the Arnoldi method to the Residual Algorithm | 89 |
| Figure 56 – Isosurfaces of stream-wise velocity of mode 1, comparing the Arnoldi method to the Residual Algorithm | 90 |
| Figure 57 – Isosurfaces of wall-normal velocity of mode 1, comparing the Arnoldi method to the Residual Algorithm | 90 |
| Figure 58 – Isosurfaces of span-wise velocity of mode 1, comparing the Arnoldi method to the Residual Algorithm | 90 |
| Figure 59 – Eigenvalues computed for the square lid-driven cavity at $Re = 1000$ and $Ma = 0.1, 0.2$ | 91 |
| Figure 60 – Evolution of the modes computed by the residual algorithm. | 92 |
| Figure 61 – The first eigenfunction of the lid-driven cavity. | 93 |
| Figure 62 – The second eigenfunction of the lid-driven cavity. | 94 |
| Figure 63 – The third eigenfunction of the lid-driven cavity. | 94 |
| Figure 64 – The first eigenfunction of the static cavity. | 95 |
| Figure 65 – The second eigenfunction of the static cavity. | 96 |
| Figure 66 – Eigenvalues computed for the three dimensional square lid-driven cavity at $Re = 900$, $Ma = 0.1$ and $\beta = 7.35$ | 97 |
| Figure 67 – Eigenvalues computed for the $\beta = 5.62$ case and compared to the reference. | 98 |
| Figure 68 – Eigenvalues computed for the $\beta = 1, 2$ and 4 cases and compared to the references. | 98 |
| Figure 69 – Parametric space investigated. | 102 |
| Figure 70 – Eigenvalues of the open cavity flow for various Mach numbers. | 102 |
| Figure 71 – Effect of Mach number on the eigenvalues of both Rossiter modes. | 103 |
| Figure 72 – Real and imaginary parts of internal energy eigenfunction of branch 1 at Mach 0.6. | 104 |
| Figure 73 – Real and imaginary parts of internal energy eigenfunction of branch 2 at Mach 0.6. | 104 |
| Figure 74 – Multiple phases of the pressure eigenfunction of Rossiter mode 1 at Mach 0.6 | 105 |
| Figure 75 – Multiple phases of the pressure eigenfunction of Rossiter mode 2 at Mach 0.6 | 105 |
| Figure 76 – Eigenvalues of the open cavity flow for various Mach numbers (thinner boundary layer). | 106 |
| Figure 77 – Effect of Mach number on the eigenvalues of the Rossiter modes (thinner boundary layer). | 107 |
| Figure 78 – Rossiter modes compared to standing wave modes and to the global modes. | 108 |

| | |
|--|-----|
| Figure 79 – Eigenfunction phases for pressure for various Rossiter modes and Mach numbers. | 109 |
| Figure 80 – Eigenvalues of the open cavity flow for various incoming boundary layer thicknesses. | 110 |
| Figure 81 – Effect of the incoming boundary layer thickness on the eigenvalues of the Rossiter modes. | 111 |
| Figure 82 – Scheme of energy transfer phenomena in a Rossiter mode and its sensitivity to Mach number and mixing layer thickness. | 112 |
| Figure 83 – Flowchart of mixing layer spatial instability analysis. | 114 |
| Figure 84 – Mixing layer thickness for various incoming boundary layer thicknesses. | 115 |
| Figure 85 – Mixing layer profile and its hyperbolic tangent approximation for an incoming boundary layer thicknesses of $D/\theta = 10, 25, 100$ | 115 |
| Figure 86 – Mixing layer spatial amplification compared to the global instability results. | 116 |
| Figure 87 – Wall-normal velocity isocontours of Rossiter modes 1 to 5 from the global stability analysis at $Ma = 0.5$ and $D/\theta = 100$ | 117 |
| Figure 88 – Placement of probes for the acoustic receptivity analysis. | 118 |
| Figure 89 – Far field acoustic receptivity measured for various Mach numbers for Rossiter modes 1 and 2. | 119 |
| Figure 90 – Acoustic pressure spectrum for Mach 0.1. | 119 |
| Figure 91 – Near field acoustic receptivity measured for various Mach numbers for Rossiter modes 1 and 2. | 120 |
| Figure 92 – Time series of stream-wise velocity for various Mach numbers. | 121 |
| Figure 93 – Close up at the beginning of the time series of stream-wise velocity for various Mach numbers. | 122 |
| Figure 94 – Close up of time series of stream-wise velocity for various Mach numbers. | 122 |
| Figure 95 – Snapshots of the pressure fluctuation in the DNS for various Mach numbers. | 123 |
| Figure 96 – Spectra of the stream-wise velocity for various Mach numbers. | 124 |
| Figure 97 – Mean mixing layer thickness for various Mach numbers. | 125 |
| Figure 98 – Mean mixing layer profile and its hyperbolic tangent approximation for various Mach numbers and the respective base flow. | 126 |
| Figure 99 – Mixing layer spatial amplification compared to the global instability results for mean flows of various Mach numbers. | 126 |

LIST OF TABLES

| | |
|--|-----|
| Table 1 – Parameters of the mesh example. | 37 |
| Table 2 – Meshes for the DNS convergence analysis. | 64 |
| Table 3 – Meshes for convergence analysis. | 67 |
| Table 4 – Eigenvalues from mesh convergence analysis. | 69 |
| Table 5 – Domains for convergence analysis. | 70 |
| Table 6 – Eigenvalues from the disturbance magnitude convergence analysis. | 73 |
| Table 7 – Eigenvalues from the 3D mesh convergence analysis. | 83 |
| Table 8 – Eigenvalues computed for the square lid-driven cavity. | 91 |
| Table 9 – Eigenvalues computed for the three dimensional square lid-driven cavity at $Re = 900$, $Ma = 0.1$ and $\beta = 7.35$ | 96 |
| Table 10 – Computation time for the two-dimensional case. | 99 |
| Table 11 – Computation time for the three-dimensional case. | 99 |
| Table 12 – Peaks from the Fourier transform of DNS data compared to Rossiter modes and global modes | 124 |

CONTENTS

| | | |
|----------|--|-----------|
| 1 | INTRODUCTION | 19 |
| 1.1 | Proposal of this study and motivation | 19 |
| 1.2 | Problem description | 19 |
| 1.3 | Scope | 21 |
| 1.4 | Summary of this work | 21 |
| 2 | REVIEW | 23 |
| 2.1 | Flow instability | 23 |
| 2.1.1 | Instabilities in cavities | 26 |
| 2.1.2 | Jacobian-free instability analysis | 28 |
| 2.2 | Aeroacoustics | 29 |
| 2.2.1 | Cavity aeroacoustics | 29 |
| 2.2.2 | Linking to stability analysis | 32 |
| 3 | METHODS | 35 |
| 3.1 | Summary of methods | 35 |
| 3.2 | Flow simulation | 35 |
| 3.2.1 | Governing equations | 36 |
| 3.2.2 | Meshing and domain | 37 |
| 3.2.3 | Boundary and initial conditions | 39 |
| 3.2.4 | Spatial derivatives | 40 |
| 3.2.5 | Time integration | 44 |
| 3.2.6 | Anti-aliasing filtering | 45 |
| 3.2.7 | Artificial damping | 46 |
| 3.2.8 | Domain decomposition and parallel execution | 49 |
| 3.3 | Instability Analysis | 51 |
| 3.3.1 | Arnoldi iteration | 52 |
| 3.3.2 | Jacobian-free instability analysis | 53 |
| 3.3.3 | Initial disturbance | 57 |
| 3.3.4 | Spectral treatment for the span-wise direction | 58 |
| 3.3.5 | Implementation | 58 |
| 3.3.6 | Residual algorithm | 60 |
| 4 | VALIDATION | 63 |
| 4.1 | DNS validation | 64 |
| 4.2 | Two-dimensional mesh independence | 66 |

| | | |
|--------|--|-----|
| 4.3 | Domain convergence | 70 |
| 4.4 | Arnoldi method convergence in two-dimensional analysis | 72 |
| 4.4.1 | Disturbance magnitude | 72 |
| 4.4.2 | Flow simulation time at each iteration | 73 |
| 4.4.3 | Number of Arnoldi iterations | 77 |
| 4.5 | DNS time steps and Arnoldi iterations trade-off | 79 |
| 4.6 | Three-dimensional mesh independence | 82 |
| 4.7 | Arnoldi method convergence in three-dimensional analysis | 85 |
| 4.8 | Comparison with the residual algorithm | 86 |
| 4.9 | Two-dimensional lid-driven cavity | 91 |
| 4.10 | Three-dimensional lid-driven cavity | 96 |
| 4.11 | Comparison to the literature for open cavities | 97 |
| 4.12 | Code performance | 98 |
| 4.12.1 | Flow simulation | 99 |
| 4.12.2 | Instability analysis | 99 |
| 5 | RESULTS | 101 |
| 5.1 | Influence of Mach number | 102 |
| 5.2 | Influence of the boundary layer thickness | 110 |
| 5.3 | Relation to mixing layer instability | 111 |
| 5.3.1 | Spatial instability analysis | 112 |
| 5.3.2 | Numerical implementation | 113 |
| 5.3.3 | Comparison to the global instability | 114 |
| 5.4 | Cavity aeroacoustic emissions | 117 |
| 5.5 | Comparison to simulation results | 120 |
| 6 | DISCUSSION | 127 |
| 6.1 | Conclusion | 127 |
| 6.1.1 | Method implementation | 127 |
| 6.1.2 | Main findings | 128 |
| 6.2 | Suggestion for future works | 129 |
| | BIBLIOGRAPHY | 131 |

Chapter 1

Introduction

1.1 Proposal of this study and motivation

The flow over an open cavity is modeled and its instability modes are computed. This is done in a computational framework with a Direct Numerical Simulation (DNS) code and a Jacobian-free eigenproblem solver.

An open cavity can be used to represent several different parts of an aircraft in flight. For example, the gap between the slats or flaps and the wing main element, the landing gear wells, gaps at doors and windows, as well as other non-aeronautical applications, such as gaps between train cars and windows and sun roofs in cars. Better understanding the flow mechanics over this simplified case can aid designers to predict the effects these geometries have over the flow stability, as well as the related acoustic emissions. (COLONIUS, 2001)

A good prediction of the transition location on a wing, or on any other aerodynamic surface, is essential to improve its performance.

Tools for linear instability analysis are developed, validated and run. The main goal is to better understand the effect of both the Mach number and the incoming boundary layer thickness to the overall instability.

1.2 Problem description

In this work, an open cavity in a flat plate is modeled and simulated. This geometry was chosen as it is relatively simple and can be used to model more complex situations, as mentioned earlier.

Figure 1 illustrates the situation. There is a uniform flow coming from the left-hand side, a boundary layer is formed on the flat plate and there is a rectangular cavity in this plate after a certain distance. The geometry is considered uniform and infinite in the span-wise direction, as is the downstream to the cavity.

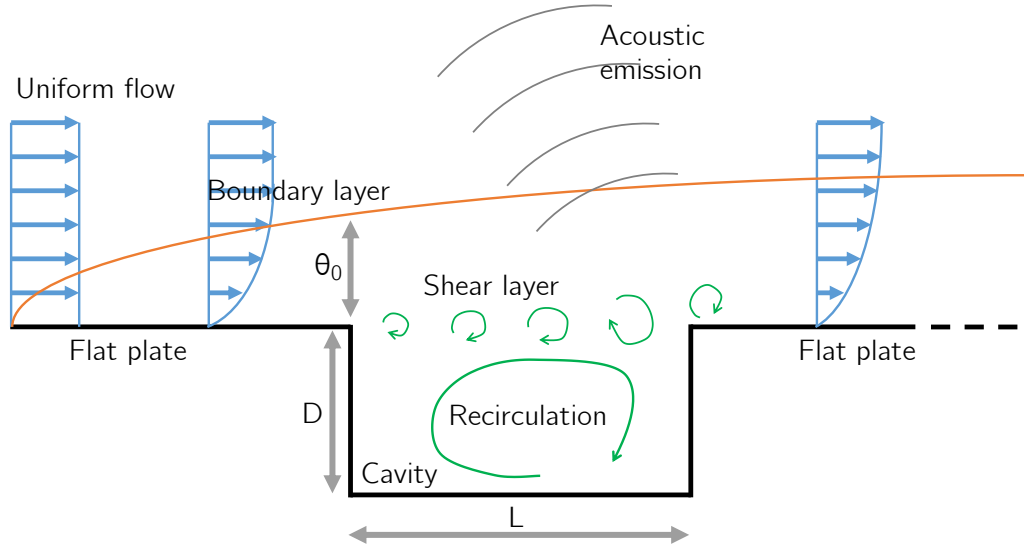


Figure 1 – Illustration of the open cavity flow.

In the usual case, the flow circulates inside the cavity and a shear layer is formed on the opening. If the flow is unsteady, sound is also emitted.

All values are non-dimensional and the parameters to be chosen are:

- L/D - Cavity aspect ratio (length by depth)
- θ_0 - Boundary layer momentum thickness at the cavity leading edge
- Re - Reynolds number
- Ma - Mach number

Depending on these parameters, the flow might be either stable or unstable. A stable flow will be steady, while an unstable flow will develop into an oscillating regime.

Figure 2 brings a diagram with neutral stability curves by Brès and Colonius (2008) for a fixed cavity aspect ratio of $L/D = 2$ and a boundary layer thickness given by $L/\theta_0 = 52.8$. At low Mach numbers, increasing the Reynolds number triggers three-dimensional instabilities, while two-dimensional instabilities tend to appear first if the Mach number is higher. For this length to depth ratio, flows above a Re_D of roughly 1300 are 3D unstable. The minimum Re for a 2D unstable flow is reduced as the Mach number increases, becoming lower than the 3D instability threshold above around Mach 0.4. These

disturbances eventually saturate to become periodic oscillations in the flow. Some of their runs are indicated in this diagram.

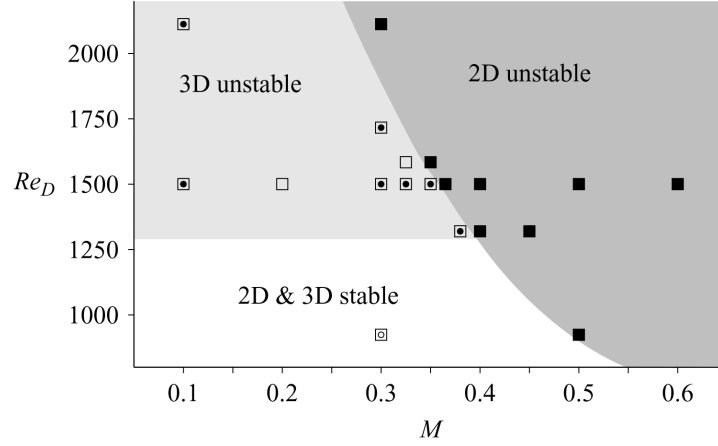


Figure 2 – Neutral stability curves for a $L/D = 2$ and $L/\theta_0 = 52.8$ open cavity as a function of Mach and Reynolds. The symbols indicate results by Brès and Colonius (2008), filled markers indicated unstable cases, squares for two-dimensional and circles for three-dimensional. (BRÈS; COLONIUS, 2008)

1.3 Scope

A computational model of this geometry is created and used to study the flow stability. Both two and three-dimensional cases are considered. The simulation is always compressible, even at low Mach numbers.

In a two-dimensional case, the flow is considered uniform in the span-wise direction. While in a three-dimensional case, the flow is periodical in this direction.

Most modern jet aircraft fly at mid to high subsonic speeds, in which compressibility plays an important role as can be seen in Fig. 2. This work will focus on this range of Mach numbers. The effect of both the Mach number and the incoming boundary layer thickness on Rossiter modes is studied.

1.4 Summary of this work

After this introduction, Chapter 2 brings a review of papers and other relevant works that have contributed to our knowledge in this area. It is divided into two sections, the first one reviews the history of flow instability studies, while the second one is about aeroacoustics and how it relates to the instabilities in cavities.

Chapter 3 describes the methods and algorithms used and the reason they were chosen, as well as detailing the computational implementation. After a quick summary, the flow simulation routine is explained. Later, the instability analysis method is described.

Chapter 4 bring data on the code validation and on its performance.

In chapter 5, the code is used to evaluate the influence of two parameters, the Mach number and the incoming boundary layer thickness on the Rossiter modes. Finally, three types of physical phenomena are discussed as for their influence on the global stability: resonance with standing wave modes; mixing layer instability; and acoustic energy transfer ratio. Full DNS runs, with non-linear effects are also performed and compared to the linear results.

Chapter 6 reviews the results and lists some possible future works.

Chapter 2

Review

2.1 Flow instability

Flow transition from laminar to turbulent regimes has been largely studied for the past century. Despite great advances in these last decades, it remains an open problem.

Among the first studies for this phenomenon, Osbourne Reynolds' work stands out. In his first publication in this matter, Reynolds (1883) classifies two types of flow: "Direct" and "Sinuous", referring to both the flow surface and the shape of a colored marker he would add to the water. His following publication Reynolds (1894) brought a new, non-dimensional parameter that relates to the transition location, accounting for the flow velocity, the fluid's viscosity and a characteristic length, taken as the tube diameter. This would later be known as the Reynolds number.

Prandtl (1904) brought the concept of the boundary layer above a flat plate, already mentioning the phenomenon of transition from laminar to turbulent flow and boundary layer separation. His students continued his work, Walter Tollmien and Hermann Schlichting were among them. (SCHLICHTING; GERSTEN, 2000)

Earlier, Rayleigh (1879) studied the stability of a parallel, inviscid flow, concluding that a necessary condition for instability was the existence of an inflection point in the velocity profile. Orr (1909) and Sommerfeld (1908) derived the equation used to determine the stability modes of a parallel, viscous flow. It would, later, be known as the Orr-Sommerfeld equation. Tietjens (1925) has investigated the transition in a boundary layer, concluding the viscosity would play a destabilizing role.

Tollmien (1929) (translated in Tollmien (1932)) and Schlichting (1933) have studied the effects of a small perturbation in a Blasius profile by modeling them as waves that are attenuated or amplified, depending on the flow stability, known today as the Tollmien-

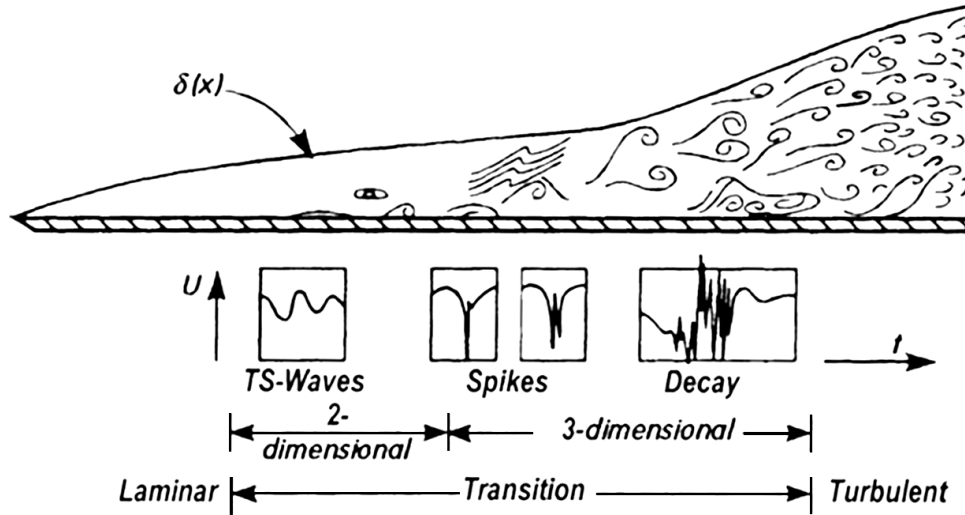


Figure 3 – The various regions of a boundary layer transition. (SCHLICHTING; GERSTEN, 2000)

Schlichting (TS) waves. In summary, Tollmien has drawn the critical stability curve in the Reynolds number versus wave number plane; and Schlichting has computed the amplification levels in this plane.

For the next decade, this theory could not be reproduced due to the high turbulence in the wind tunnels of the time. Finally, Schubauer and Skramstad (1943) were able to use a low turbulence wind tunnel and successfully observe the amplification of periodic waves just upwind of the transitional region in a boundary layer, soon followed by Liepmann (1943). These observations matched Tollmien and Schlichting's theory.

Schubauer and Skramstad (1943) used a vibrating ribbon in the boundary layer to generate controlled TS waves and observed the spatial evolution of their amplitude, as illustrated in Fig. 4. This image also shows the stability diagram from the Orr-Sommerfeld equation.

According to Lin (1955), the disturbance kinetic energy in a two-dimensional boundary layer increases at a rate given by $-\rho u'v'u_y$, where ρ is the density, u and v are velocities parallel and normal to the flow, respectively. The prime denotes fluctuations and the subscript, a derivative. In an inviscid flow, u' and v' have a 90° phase difference, causing this product to be always null. Prandtl noticed that the viscosity tends to increase this phase difference, causing a positive energy flow rate, as illustrated in Fig. 5.

So far, the Navier-Stokes equations have been studied in their linearized form. Landau (1944) has begun investigating non-linear effects, followed by several researches in the next decades. Klebanoff and Tidstrom (1959) have linked these non-linear effects in a flat plate boundary layer to oscillations of TS waves amplitude in the span-wise direction, creating three-dimensional effects, which have previously been linked to the appearance of

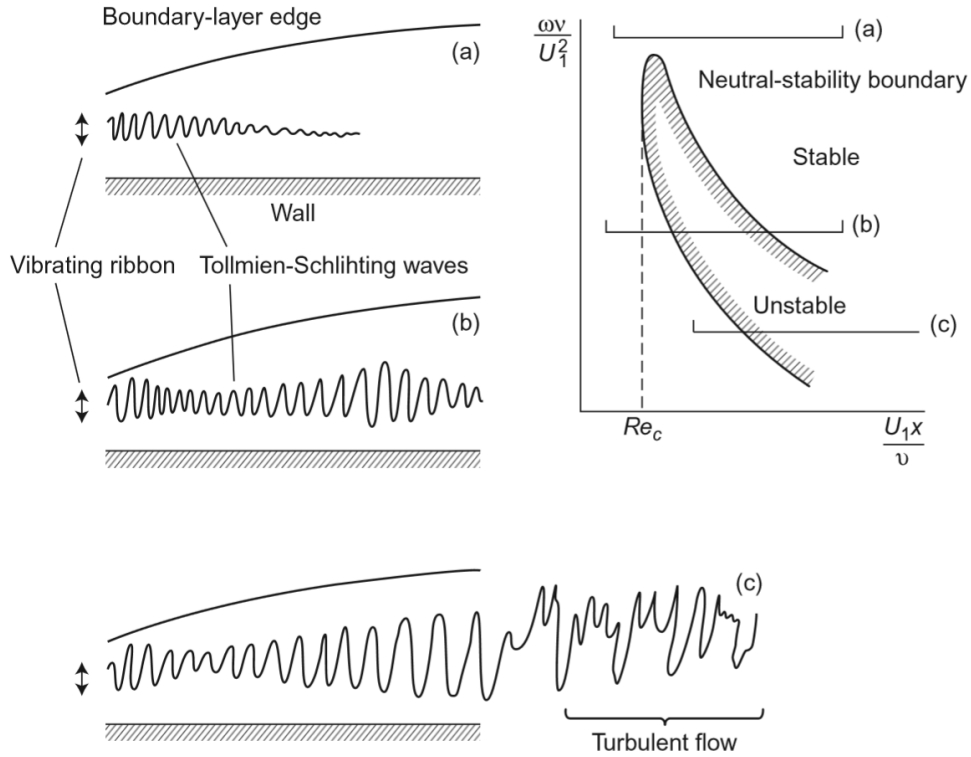


Figure 4 – Illustration of TS waves evolution before transition to turbulence. (HOUGHTON et al., 2012)

turbulent spots, which precede the fully turbulent flow. (EMMONS, 1951)

Gaster (1962) has connected the effects of temporal disturbance growth, that can also be predicted theoretically, to the spatial growth, observed experimentally, proposing the solution of the Orr-Sommerfeld equations for spatial modes (GASTER, 1965). Bouthier (1972) removes the parallel flow approximation that had been used so far, accounting for the spatial growth of the boundary layer.

Ingen (1956) has proposed a method to predict the transition location from the disturbance amplification rates, known as the e^n method. Its idea is to integrate the amplification rate through the boundary layer and to assume transition happens when this integral reaches a certain threshold, represented by the constant e^n . Usually, $e = 9$ is taken as an average value, in flight, lower or greater values may be used depending on the transition type and the environmental conditions.

The e^n method is used to this day to predict the transition position, for example, in airfoils. Drela and Giles (1987) used this theory in the very popular XFOIL and MSES codes for airfoil evaluation and design. It is worth noting that the pressure gradient in airfoils influences the stability and should be accounted in the Orr-Sommerfeld equation.

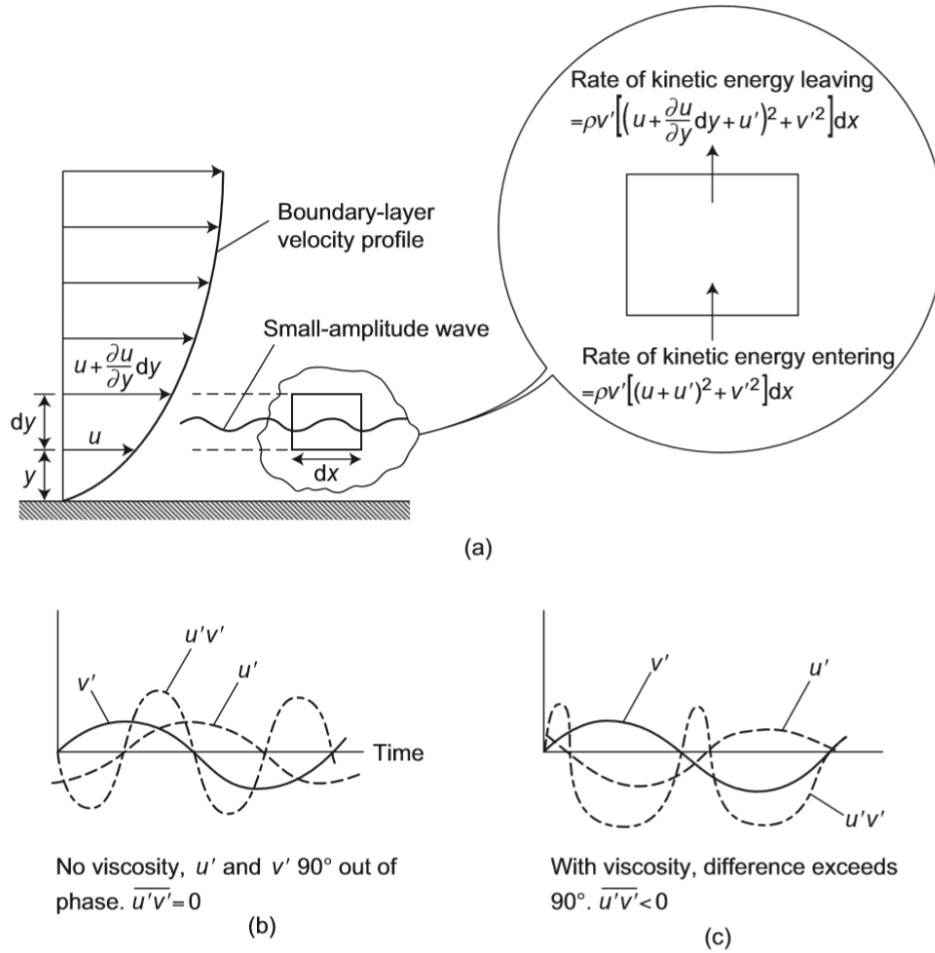


Figure 5 – Illustration of the energy flow rate in TS waves. (HOUGHTON et al., 2012)

2.1.1 Instabilities in cavities

Cavity flow studies were first motivated by both its acoustic emissions and pressure oscillations over surfaces such as gaps in wings or openings in fuselages, specially landing gear doors or spoilers. Krishnamurty (1956) has performed an experimental analysis on a two-dimensional gap in an airfoil. Owen (1958) has studied the pressure oscillations caused by these features and their effects on the aircraft structure.

Rossiter (1964) investigated the effects of instability in the flow over a cavity and related them to its aspect ratio, concluding that deeper cavities tend to have a cleaner and more periodical spectrum, while shallower cavities tend to have more relevant random frequencies. He has also proposed his famous empirical equation to predict the dominant frequencies, which will be further discussed in the aeroacoustics section.

Non-linear interactions between modes were investigated by Knisely and Rockwell (1982). Cattafesta et al. (1998) have experimentally observed a switching between Rossiter modes, which was later studied by Kegerise et al. (2004).

The disturbances amplification rates may be computed by the linear stability theory, Rowley, Colonius and Basu (2002) presents a diagram containing amplification rate as a function of the ratio between boundary layer thickness and cavity depth (D/θ), obtained numerically, with a DNS. Another option to obtain these values is by a global instability analysis, as done by Theofilis (2000a).

Besides the interactions between the flow and its acoustic field, there may also be purely hydrodynamic instabilities, as observed by Gharib and Roshko (1987) and, later by Rowley, Colonius and Basu (2002) in numerical simulations.

McGregor and White (1970) justified research on cavity instability by concluding that, in transonic and supersonic flows, aerodynamic drag in surfaces with cavities is greatly increased if there is an acoustic resonance. Dix and Bauer (2000) points out that pressure fluctuations due to cavities may reach great amplitudes that, besides the acoustic emission, might cause structural fatigue as they are specially correlated waves, causing repetitive stress on some structural points. Outside of the aeronautical scope, other justifications may be found. Kook and Mongeau (2002), for example, were motivated by automotive sunroofs.

More recently, cavity flow control came into the scope of researchers (HOWE, 1997; COLONIUS, 2001; ROWLEY; WILLIAMS, 2006). Control can be either passive, done by features such as grills, spoilers and ramps, or active, by using suction, jets, oscillators and piezoelectric components (CATTAFESTA et al., 2003; WILLIAMS; ROWLEY, 2006; THEOFILIS, 2011).

Brès and Colonius (2008) performed open cavity simulations with high order finite difference schemes Lele (1992) to investigate the interaction between two and three-dimensional modes. Mack and Schmid (2010) have studied the instability in a swept cavity in supersonic flows by using a combination of a DNS and Krylov subspace algorithms.

Yamouni, Sipp and Jacquin (2013) related modes from bi-global stability analysis to Rossiter and standing wave modes in a square cavity. They conclude that interactions between these two phenomena may affect the global mode, causing it to be more unstable when their frequencies match.

Meseguer-Garrido et al. (2014) investigated a range of parameters for span-wise periodic incompressible open cavities, documenting the neutral curves and the characteristics of the leading eigenmodes.

Sun et al. (2016) compared the effect of using a time-averaged three-dimensional flow as base-flow for a bi-global stability analysis against using a regular base-flow, which has a null time derivative. They conclude that in some cases, usually with longer cavities, the two-dimensional wake modes are absent due to this modified base-flow.

Qadri and Schmid (2017) investigated the effects of shallow cavities, with a depth

similar to the boundary layer thickness, as a frequency selection mechanism, as well as its effects on the flow stability. His reasoning is that small surface irregularities are unavoidable in a real situation and that understanding their influence on the flow stability is a step towards more robust designs.

2.1.2 Jacobian-free instability analysis

The most straight-forward approach to obtain the instability modes of any system is to compute its Jacobian matrix and to find its eigenvalues and eigenvectors. Unfortunately, this matrix grows very fast as the mesh becomes finer, causing the processor and memory requirements to quickly increase, especially if the matrix is full.

Arnoldi (1951) has developed an iterative algorithm to compute some of the eigenvalues of large matrices, based on the Krylov subspaces. One of the most interesting features of this method is that the matrix itself is not explicitly required, just the ability to compute vector multiplications with it.

Eriksson and Rizzi (1985) have implemented the Arnoldi iteration in to compute the steady state of an inviscid flow over an airfoil. Arnoldi's method was used to find the least stable eigenvalues of the flow, which were artificially damped, speeding up the convergence.

Edwards et al. (1994) have used it on a Couette-Taylor flow. First to find a steady state solution, then to speed up its time evolution by exponential propagation and, finally, to obtain the leading eigenvalues and corresponding modes of the flow.

Chiba (1998) has used this method on more complex geometries, such as a cylinder wake. Tezuka and Suzuki (2006) were the first to implement it for three-dimensional flows. Gómez, Gómez and Theofilis (2014) have used the open-source OpenFOAM (WELLER et al., 1998) code to perform the flow simulation, allowing for much more complex geometries.

Arnoldi's method finds the eigenvalues iteratively, first converging the ones that are further away from the complex plane's origin. Due to the exponential operations used, these outermost eigenvalues map to the most unstable modes. Gómez et al. (2015) have used a shift-invert strategy in the algorithm so one can control which region of the complex plane contains the first converged eigenvalues, this technique can be used, for example, to focus on the acoustic modes.

Most instability analyses involve first computing a base flow, which is used as the central point for the linearized equations. Barkley (2006), Sipp and Lebedev (2007) compare the modes in this base flow to the actual oscillations observed in the flow. Their studies focus on the flow around a cylinder very close to the critical Reynolds number and its wake modes. For the cylinder, they conclude that the frequencies found by the linear

stability analysis are very close to the ones observed in the limit-cycle when non-linearities are also considered. They mention that this is not valid for any type of flow, using the open cavity as a counter-example. One remark is that the mean flow from the non-linear equations coincides with the base flow for the instability analysis at the bifurcation, i.e. at critical stability conditions.

2.2 Aeroacoustics

Lord Rayleigh's work is often cited as the basis of acoustics Rayleigh (1877), Rayleigh (1878). It brought together various works from different authors under a single, unified theory, becoming the starting point for upcoming research.

In a similar way, the work of Lighthill is often considered the basis for aeroacoustics (LIGHTHILL, 1952; LIGHTHILL, 1954). He has focused on identifying the kinds of flows that generate sound and to understand how much of the flow's energy is transferred to the acoustic field. It is worth noting that the flow is the only sound source accounted for in this work, structure vibrations, for example, are not covered by it, but might be included as boundary conditions in some cases.

Generally speaking, Lighthill considered the acoustic field fluctuations to be much smaller than the base flow magnitude, causing non-linear terms relative to these fluctuations in the Navier-Stokes equations to be considered very small and, thus, removed.

He has also defined three basic types of acoustic sources. The monopole, equivalent to an oscillating source of mass in the flow, the most efficient way of generating sound. The dipole, equivalent to an oscillating force. And the quadrupole, equivalent to a fluctuating shear tension, the least efficient acoustic source.

With the increase of commercial jets in service after the 1960s, especially the supersonic Concorde, the necessity of more aeroacoustic research became evident (FFOWCS-WILLIAMS, 1977; FFWCS-WILLIAMS, 1996). These studies focused initially on jet noise, as the engines were, by a fair margin, the greatest acoustic sources.

2.2.1 Cavity aeroacoustics

Initially, open cavity research was motivated by their vibration modes, with special attention given to the frequencies. Acoustic intensity was not considered very relevant due to the much louder engines of the time. The concern of whether or not there would be oscillatory modes as what would be their frequencies was for structural reasons, as these oscillations could excite modes in the structure, speeding up fatigue. To a smaller extent,

there was also some concern on the increased drag caused by the oscillations. (OWEN, 1958).

Krishnamurty (1956), motivated by the buffeting observed in aircraft cavities such as open cockpits or landing gear doors, performed an experimental campaign and concluded that the minimum cavity size that generates sound is reduced as the Mach number increases and that this size is inversely proportional to the sound frequency observed. He has also reported that sound intensity grows quickly with the Mach number, roughly at its eighth power, as predicted by the existing theories. Acoustic waves were also visualized by Schlieren photography, qualitatively showing the sound directivity, as shown in Fig. 6.

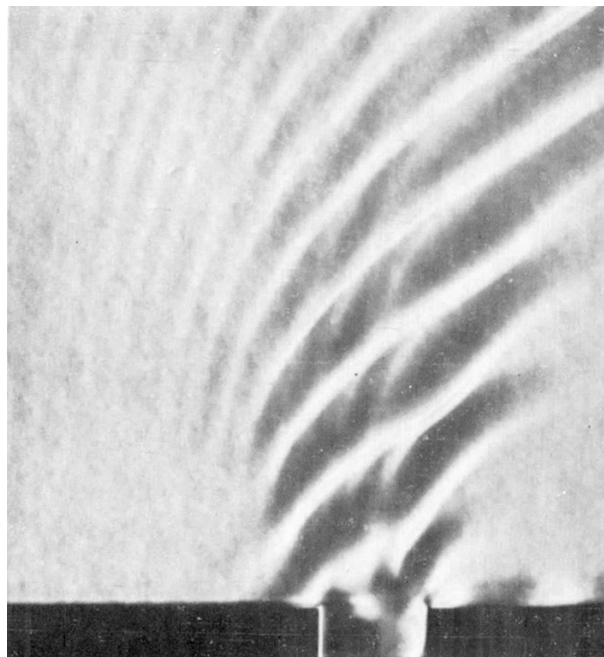


Figure 6 – Schlieren image of the cavity flow showing its acoustic output. (KRISHNAMURTY, 1956)

At the same time, Roshko (1955) performed experiments to generate more data on open cavity flow and to observe its structures, also looking to understand the relevance of the cavity aspect ratio. His work is focused on the mean flow over the cavity, not on the oscillations that, eventually, become sound waves.

Rossiter (1964) has performed an experimental campaign at subsonic and transonic velocities, resulting in his famous semi-empirical equation, which connects flow parameters, such as Mach number and cavity length to the observed sound frequencies. It is still largely used to this date (COLONIUS, 2001; GLOERFELT, 2009). His equation has some empirical constants, obtained experimentally.

This equation assumes that the unstable mode that generates sound is triggered by an acoustic feedback. In short, when a vortex reaches the cavity's downstream edge, it

generates acoustic waves that travel back to the upstream edge, triggering the shear layer modes that generate another vortex.

Rossiter's equation matches well with experimental results, despite a considerable dispersion, especially at lower Mach numbers. The saturation amplitudes of the modes present a much higher dispersion than the frequencies, due to the high sensitivity to disturbances in the shear layer. (COLONIUS, 2001)

Through the years, various corrections and adjustments of empirical values have been suggested to Rossiter's equation. (HELLER; HOLMES; COVERT, 1971; ROCKWELL; NAUDASHER, 1979)

Plumlee, Gibson and Lassiter (1962) have proposed another mode for sound generation in an open cubic cavity, later extended to other geometries by Tam (1976). In this mode, stationary waves normal to the flow receive energy from the shear layer over the cavity, modes are selected depending on their frequencies and this energy is sent back to the flow in acoustic form. In this work, the Navier-Stokes equations were simplified by several hypotheses. After the boundary conditions were applied, the resulting equation predicts the frequencies and modes and depends on no empirical constants, just on two integers, related to the mode number.

East (1966) linked aeroacoustic feedback mechanisms (Rossiter) to acoustic resonance mechanisms (Plumlee), concluding that they may interact with each other, amplifying the sound output if their frequencies match.

Comparing his results to experiments, Tam (1976) concluded that they are valid only for cavities with a depth greater than their length and above a certain Mach number, around 0.25. He argues that in shallow cavities or at lower Machs, the energy absorbed by the standing waves is much less than what is needed to generate sound, damping these waves until they are practically non-existent. This complements East's conclusions.

Block (1976) has also compared both mechanisms experimentally, reaching a similar conclusion. Deeper cavities tend to have stronger acoustic resonance modes while longer ones have stronger aeroacoustic feedback modes. Peaks in sound intensity were also observed when the modes matched in frequency. She has also noted that at higher velocities, only the feedback modes are seen, other modes appear at lower velocities, widening the spectrum. This mode interaction was also discussed by Rockwell and Naudasher (1979), Yamouni, Sipp and Jacquin (2013).

Howe (2004) identifies the sound generation mechanisms at low Mach numbers, roughly from 0.01 to 0.2. He has used a Green's function for this geometry and analytical models of the sources, treating them as monopoles and dipoles. The monopole source is associated with the net flux of mass entering or leaving the cavity, while the dipole is associated with an unsteady drag force caused by the interaction of the vorticity and the

cavity trailing edge, which happens due to the shear layer instability.

Howe has concluded that at very low Mach numbers the sound radiation is dominated by the dipole source caused by the unsteady drag force, while at slightly higher Mach numbers, the monopole source takes over. This is illustrated in Fig. 7, which compares the directivity at Mach 0.05 and at Mach 0.1.

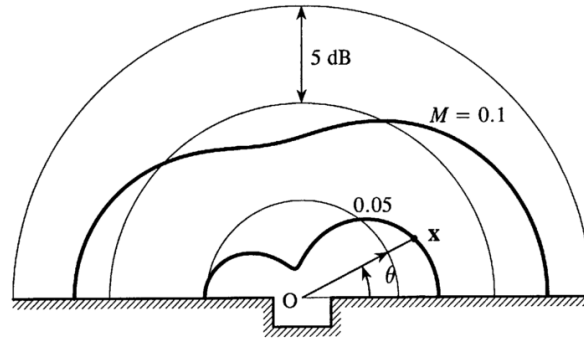


Figure 7 – Cavity acoustic directivity at Mach 0.05 and Mach 0.1. (HOWE, 2004)

He has also concluded that, at lower frequencies, the emission is dominated by the dipole and, at higher frequencies, by the monopole, as can be seen in Fig. 8.

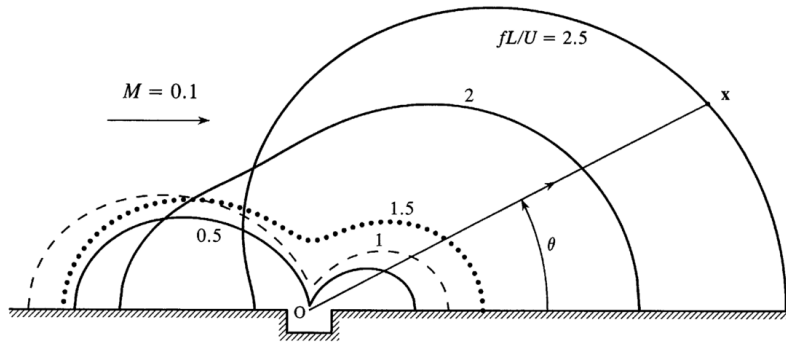


Figure 8 – Cavity acoustic directivity at Mach 0.1 for various frequencies. (HOWE, 2004)

The ever increasing computational power has allowed for numerical simulation of the cavity flow. This new tool allows better visualization of the flow. Several types of modeling can be used, from Direct Numerical Simulation (DNS) and Large Eddy Simulation (LES) for lower Reynolds numbers to Reynolds Averaged Numerical Simulation (RANS) for larger values. (COLONIUS, 2001; ROWLEY; COLONIUS; BASU, 2002)

2.2.2 Linking to stability analysis

The acoustic emission of a cavity is strongly linked to its oscillation modes and depends on the existence of unstable eigenvalues. Great advances were achieved in this

direction by bi-global instability analysis Theofilis (2003), Brès and Colonius (2008), Vicente et al. (2014). Eigenvalues in the complex plane can be mapped for the cavity flow, indicating the existence of unstable modes and their respective frequencies. These modes grow until non-linear effects cause them to reach a saturation point.

Most recent investigations on open cavities focus on the flow stability. Meseguer-Garrido et al. (2014) have performed a parametric study of the flow and its instability modes. Liu, Gómez and Theofilis (2016) have compared two-dimensional cavities, with an infinite span, to three-dimensional ones, with a finite span, concluding that most effects are shared by both geometries. These last results were obtained for incompressible flows and acoustic analogies might be done from them. A compressible flow would be needed if direct observation of the acoustic field is desired.

A limited number of papers were found in the literature about mid to high subsonic flows over a cavity, such as Brès and Colonius (2008), Yamouni, Sipp and Jacquin (2013), Sun et al. (2016), Sun et al. (2017), which mostly focus on how the Mach number affects the stability. This range of Mach numbers is certainly important for practical reasons as this is where most modern aircraft fly. This work is in the direction of expanding the current knowledge of open cavity flows in this sense, a focus will be given to the effect of the boundary layer thickness over the cavity, about which not much was found.

Chapter 3

Methods

3.1 Summary of methods

A Direct Numerical Solver (DNS) for the Navier-Stokes equations on an open cavity was developed. Special attention is given to the code's capability of operating at the high order of precision required for instability and acoustic analysis. Various numerical methods were implemented in the solver, including the spectral-like compact finite differences shown by Lele (1992).

This DNS is used to generate the base flow for the instability analysis. It is also part of the matrix-free instability analysis methods to compute the flow's eigenvalues and their respective eigenfunctions. Regular matrix-forming methods would demand an enormous amount of memory to compute the flow modes, in the order of the squared total number of nodes in the domain multiplied by the number of variables, which would easily scale into gigabytes or even terabytes of memory solely to store the required matrices (THEOFILIS, 2011).

This matrix-free method is based on the work of Eriksson and Rizzi (1985), who have implemented an algorithm based on Arnoldi (1951) to find the most unstable or least stable modes of an inviscid flow around an airfoil.

3.2 Flow simulation

The direct numerical simulation code was developed by a hydrodynamics instability research group in the São Carlos School of Engineering, University of São Paulo, for several uses, and was adapted for the open cavity flow. It is written in FORTRAN 90 language and uses a domain decomposition technique along with MPI and OpenMP for

parallelization. (BERGAMO, 2014; MARTINEZ; MEDEIROS, 2016; MARTINEZ, 2016)

3.2.1 Governing equations

The compressible Navier-Stokes equations are used to model the flow, along with mass and energy conservation equations. A compressible flow can be entirely defined by five variables: density (ρ), internal energy (e) and the three velocity components (u, v, w), in this case. Each variable depends on location (x, y, z) and time (t).

Equations are written in the non-conservative form, which solves for each individual variable mentioned above, simplifying the boundary conditions.

$$\frac{\partial \rho}{\partial t} = -\rho \frac{\partial u_i}{\partial x_i} - \frac{\partial \rho}{\partial x_i} u_i \quad (3.1)$$

$$\frac{\partial u_j}{\partial t} = -\frac{\partial u_j}{\partial x_i} u_i - \frac{1}{\rho} \frac{\partial p}{\partial x_j} + \frac{1}{\rho} \frac{\partial \tau_{ij}}{\partial x_i} \quad (3.2)$$

$$\frac{\partial e}{\partial t} = -\frac{\partial e}{\partial x_i} u_i - \frac{p}{\rho} \frac{\partial u_i}{\partial x_i} + \frac{1}{\rho} \tau_{ij} \frac{\partial u_j}{\partial x_i} - \frac{1}{\rho} \frac{\partial q_i}{\partial x_i} \quad (3.3)$$

Where the viscous tensor and the heat flux term are:

$$\tau_{ij} = \frac{\mu(T)}{Re} \left(\frac{\partial u_i}{\partial x_j} + \frac{\partial u_j}{\partial x_i} - \frac{2}{3} \delta_{ij} \frac{\partial u_k}{\partial x_k} \right) \quad (3.4)$$

$$q_i = -\frac{\mu}{(\gamma - 1) Re Pr M_\infty^2} \frac{\partial T}{\partial x_i} \quad (3.5)$$

Temperature and pressure, assuming an ideal gas, are given by:

$$T = e \gamma (\gamma - 1) M_\infty^2, \quad p = (\gamma - 1) \rho e \quad (3.6)$$

Viscosity is modeled by Sutherland's law:

$$\frac{\mu^*}{\mu_\infty} = \mu(T) = \frac{1 + C}{T + C} T^{\frac{3}{2}} \quad (3.7)$$

Defining $C = \frac{110K}{T_\infty^*}$ and $T_\infty^* = 300K$.

All values are non-dimensional, being normalized by the free flow speed, cavity depth and initial density. Reynolds, Prandtl and Mach numbers are given by:

$$Re = \frac{\rho_\infty^* U_\infty^* L_0}{\mu_\infty^*}, \quad Pr = \frac{\mu_\infty^* c_p^*}{k^*}, \quad M_\infty = \frac{U_\infty^*}{\sqrt{\gamma \frac{p_\infty^*}{\rho_\infty^*}}} \quad (3.8)$$

Dimensional (denoted with a *) and non-dimensional values are related by the following equations.

$$\rho = \frac{\rho^*}{\rho_\infty^*}, \quad p = \frac{p^*}{p_\infty^* U_\infty^{*2}}, \quad x_i = \frac{x_i^*}{L_0}, \quad T = \frac{T^*}{T_\infty^*}, \quad u_i = \frac{u_i^*}{U_\infty^*}, \quad t = \frac{t^* U_\infty^*}{L_0}, \quad e = \frac{e^*}{U_\infty^{*2}} \quad (3.9)$$

3.2.2 Meshing and domain

The code uses a structured mesh in a rectangular domain. The grid is much finer in the wall-normal direction close to the flat plate and the cavity. There is also stretching in the stream-wise direction, concentrating nodes on the cavity.

The following equation is used to obtain the node locations.:

$$\bar{x} = \eta - \frac{A}{B} \tanh(B(\eta - \eta_0)) \quad (3.10)$$

A and B are stretching parameters. η_0 controls the refinement location. η goes from 0 to 1 at equally spaced intervals. \bar{x} is linearly transformed to match the desired initial and ending points for the mesh.

A , B and η_0 have to be carefully chosen so that there are nodes positioned exactly at the cavity edges in both x and y directions and at the flat plate leading edge. An algorithm was developed with this goal, it takes desired values for the stretching parameters as inputs and slightly modifies them to meet these criteria. This algorithm is also allowed to slightly change the inlet x coordinate. Note that, as will be explained in the next subsection, this does not affect the flat plate, which always begins at $x = 0$.

Table 1 shows parameters for an example mesh with a cavity at $2.96 \leq x \leq 4.96$ with unitary depth.

Table 1 – Parameters of the mesh example.

| | x | y |
|------------------|-------|-------|
| Number of nodes | 400 | 150 |
| Initial position | -3.04 | -1 |
| Final position | 12 | 5 |
| A | 0.99 | 0.995 |
| B | 0.5 | 0.3 |
| η_0 | 0.488 | 0.316 |

Figure 9 illustrates this mesh, note that only one node for every four in each direction is shown. Figure 10 shows the nodes' positions and spacings for this mesh.

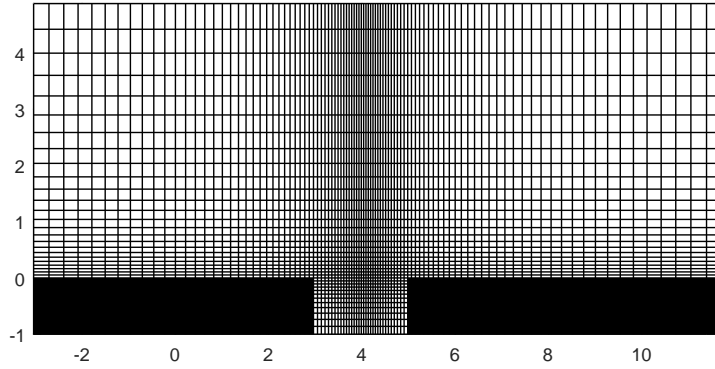


Figure 9 – Illustration of a mesh, only one node for every four is shown.

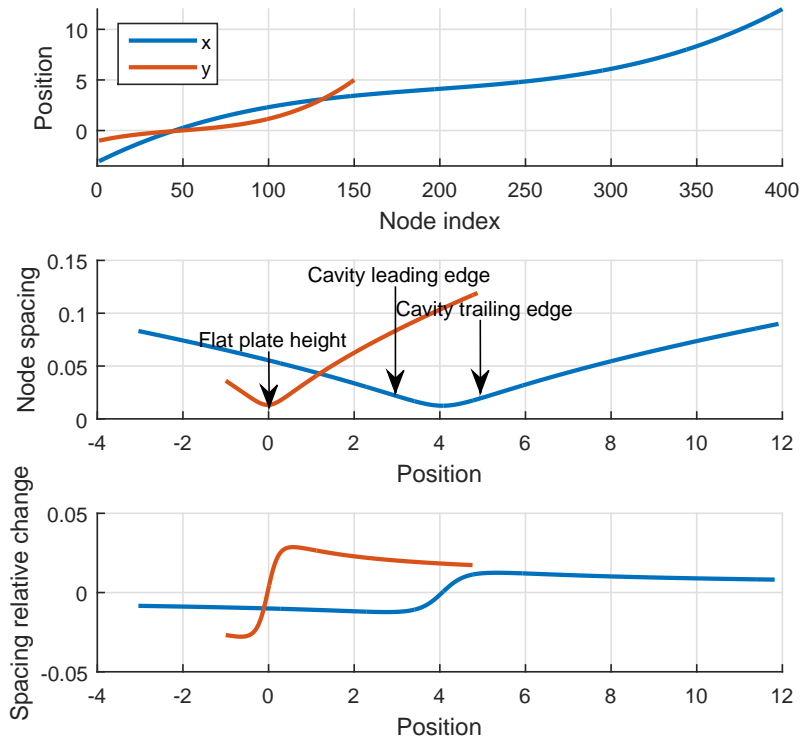


Figure 10 – Positions of nodes and their spacing in an example mesh.

In this example, there are 131 nodes out of 400 in x inside the cavity and 48 out of 150 in y .

Closer to the open boundaries, in both directions, the spacing is greatly increased, as part of the buffer zone. No multidomain technique is used in this case, grid points inside the wall are ignored by the solver. Figure 11 illustrates the domain, the buffer zone is shown in blue, while points inside the wall are orange, darker colors indicate a finer grid.

For 3D cases, in the span-wise direction, the mesh is equally spaced and the domain

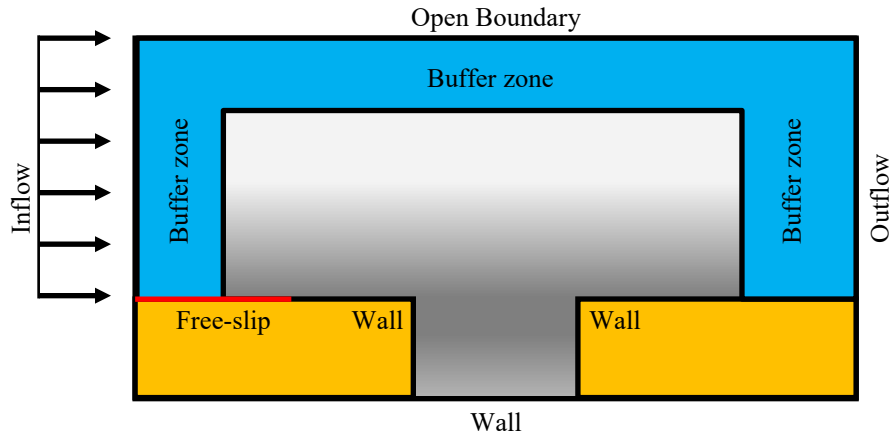


Figure 11 – Illustration of the domain and its boundaries. Buffer zone is shown in blue, points inside the wall are orange, darker grays indicate a finer grid.

is periodical. The domain size in this direction defines the possible span-wise wave numbers in the simulation.

3.2.3 Boundary and initial conditions

The inflow boundary is defined as a uniform flow at constant temperature and a Neumann condition is placed for the pressure so that its derivative is null in the flow direction. In the outflow, pressure is kept constant and Neumann homogeneous conditions are used for temperature and velocities.

Walls have no-slip and no-penetration conditions for velocity, the pressure gradient is set to zero in the normal direction and the temperature is fixed. Just downstream of the inflow, there is a free-slip region in the wall, it is necessary to accommodate the flow before the boundary layer starts forming.

It is worth noting that pressure and temperature are not directly available as variables in the code and they should be computed from the density and energy values. The temperature depends solely on the energy and pressure depends on both density and energy. This way, the boundary conditions routine first changes the energy to observe the temperature conditions and, later, the density to keep the pressure conditions.

The two top corners on the cavity were points of particular attention for the boundary conditions. The Neumann homogeneous condition for pressure in other points is observed by computing the density at each point of the boundary so that the pressure's derivative is null in the normal direction on the wall. Both corner nodes present a problem as walls in distinct directions meet and the density that observes the Neumann condition in one direction might violate it for the other. The pressure in both nodes is set to the mean of the pressures that meet the boundary condition for each direction.

The initial condition is defined as free-flow velocity above the flat plate and zero velocity in the cavity, at constant pressure and temperatures. Results from previous runs can also be used as initial condition as long as they share the same mesh; Reynolds and Mach numbers and the numerical methods may be changed.

For the lid-driven cavity case, simply setting the tangential velocity to unity at the lid would cause issues at the corners, as this condition is not compatible to the neighboring walls. As done by Vicente et al. (2011) and Bergamo (2014), the tangential velocity at this boundary is given by:

$$u = \left(1 - (2x - 1)^{18}\right)^2 \quad (3.11)$$

This profile is very close to a uniform unitary flow, but smoothly reduces the velocity to zero at the edges. This equation is valid if the edges are located at $x = 0$ and $x = 1$.

In this case, the initial condition is a static flow.

3.2.4 Spatial derivatives

Spatial derivatives are computed by a finite differences method chosen before runtime. Explicit second and fourth order methods are implemented, as well as compact fourth order spectral-like and sixth order schemes described by Lele (1992). It is possible to use a distinct differentiation method for the buffer zone, usually of a lower order, the transition from one method to the next happens smoothly.

The following equation has to be solved when the derivative is needed:

$$\beta u'_{i-2} + \alpha u'_{i-1} + u' + \alpha u'_{i+1} + \beta u'_{i+2} = a \frac{u_{i+1} - u_{i-1}}{2h} + b \frac{u_{i+2} - u_{i-2}}{4h} + c \frac{u_{i+3} - u_{i-3}}{6h} \quad (3.12)$$

α , β , a , b and c are adjustable coefficients, h is the mesh spacing, f_i is the function value at node i and f'_i , its approximated derivative.

Close to the boundaries, the stencil is shifted and coefficients are adjusted accordingly.

If both α and β are null, there is no need to solve a linear system as the derivative is given explicitly. The simplest scheme is the explicit second order, in which $a = 1$ and all other parameters are null. An explicit fourth order scheme has $a = 4/3$ and $b = -1/3$.

The order of accuracy of a scheme is given by which of the following equations hold true for its coefficients.

$$\text{2nd order: } a + b + c = 1 + 2(\alpha + \beta) \quad (3.13)$$

$$\text{4th order: } a + 2^2b + 3^2c = 6(\alpha + 2^2\beta) \quad (3.14)$$

$$\text{6th order: } a + 2^4b + 3^4c = 10(\alpha + 2^4\beta) \quad (3.15)$$

$$\text{8th order: } a + 2^6b + 3^6c = 14(\alpha + 2^6\beta) \quad (3.16)$$

Despite being able to achieve high orders of formal accuracy, explicit schemes quickly lose precision at higher wave numbers, due to the increased high-order derivatives.

The difference in amplitude from the exact differentiation to the numerical approximation for each wave number, also known as the modified wave number, is given by:

$$\omega'(\omega) = \frac{a \sin(\omega) + b \sin(2\omega)/2 + c \sin(3\omega)/3}{1 + 2\alpha \cos(\omega) + 2\beta \cos(2\omega)} \quad (3.17)$$

Lele (1992) uses this relation to derive some spectral-like derivative schemes. Ideally, the modified wave number would always match the original wave number.

Besides both explicit schemes, a spectral-like derivative routine was implemented. The restrictions are as follow:

1. Fourth order accuracy
2. Tridiagonal system
3. 5-point stencil
4. $\omega'(1.8) = 1.8$

For the first item, Eqs. 3.13 and 3.14 must hold true. For the second and third items, chosen to reduce the computational cost, $\beta = 0$ and $c = 0$. For the fourth item, Eq. 3.17 must hold true for $\omega' = \omega = 1.8$.

Therefore, there are five equations for the five variables, fully defining the system and resulting in $\alpha = 0.364957272268410$, $\beta = 0$, $a = 1.57663818151227$, $b = 0.153276363024547$ and $c = 0$.

Figure 12 shows the modified wave number for some numerical schemes. Note how the spectral-like method stays closer to the exact value even at higher wave numbers.

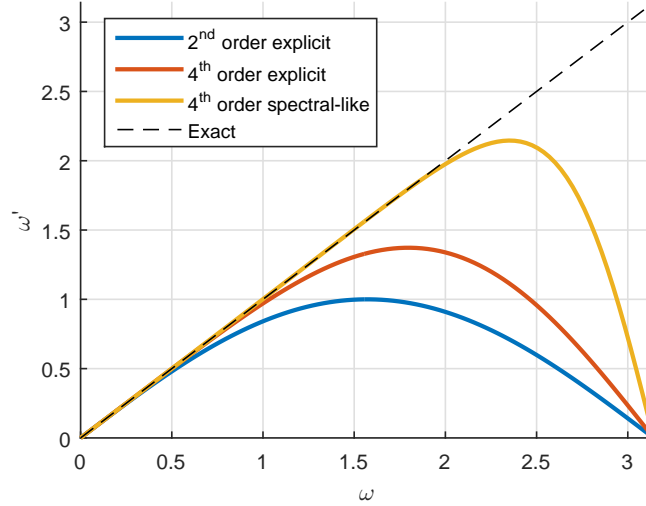


Figure 12 – Modified wave number for various numerical differentiation schemes.

It is important to note that these finite difference methods only work for equally spaced meshes. Therefore, the well know chain rule for derivatives must be used, as shown in the following equation.

$$\frac{\partial u}{\partial x} = \frac{\partial u}{\partial \phi} \frac{\partial \phi}{\partial x} \quad (3.18)$$

u is the function value and x is the actual mesh dimension. ϕ is the dimension in an intermediate mesh which corresponds node to node with the actual mesh. This intermediate mesh is equally spaced with $h = 1$. Therefore, both terms on the right-hand side of Eq. 3.18 can be obtained by standard finite difference methods. Note that the second term only needs to be computed once as it depends only on the mesh.

Once more, both corner nodes presented a challenge for these methods when computing the derivative. Fig. 13 illustrates the Regions considered. In an inner node, i.e. away from the boundaries, finite differences method uses the nodes around it to approximate the derivative. If no other changes were made to the code, corners nodes 1 and 2 would be considered as inner nodes and, thus, derivatives computed for them would account for both points on the wall and points immersed in the flow, which would not be correct and cause the solution to fail. Because of this, both these nodes only consider values in Region 2 of Fig. 13.

This has solved the problem for both corner nodes and for the region between them. But nodes in Regions 1 and 3 of the figure would still have its derivatives miscalculated, causing discontinuities in the domain close to the corner, which would later cause the

simulation to fail. This was solved by considering both the last node in Region 1 and the first node in Region 3 as inner nodes for the finite differences method, which makes the derivative a continuous function again.

In sum, derivatives in Region 2 depend only on values in it. Derivatives in Regions 1 and 3 depend on values both in their respective regions and on values in Region 2. The approach for wall-normal derivatives is analogous.

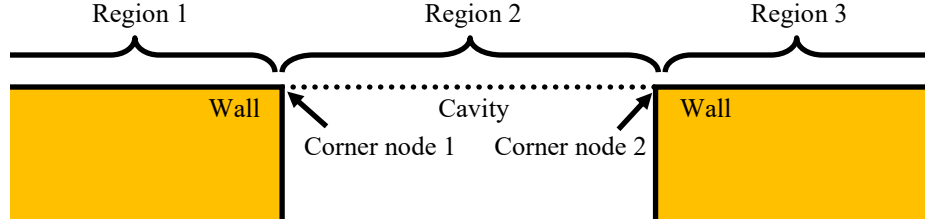


Figure 13 – Close-up of the corner nodes in the domain and the regions considered for derivatives.

Equation 3.19 illustrates how the derivatives would be computed close to corner node 1, with index c_1 . α , a , b and c are the finite differences coefficients, note that they are different for the corner nodes and more coefficients may be added depending on the derivative scheme chosen. D and f are vectors containing the derivatives and the function values for each node, respectively.

$$\begin{aligned}
 & \begin{bmatrix} 1 & \alpha & & & \dots & 0 \\ \alpha & 1 & \alpha & & & \vdots \\ & \ddots & \ddots & \ddots & & \\ & & \alpha & 1 & \alpha & \\ & & & 1 & \alpha & \\ \vdots & & & \alpha & 1 & \alpha \\ 0 & \dots & & & \ddots & \ddots & \ddots \end{bmatrix} \begin{bmatrix} D_1 \\ D_2 \\ \vdots \\ D_{c_1-1} \\ D_{c_1} \\ D_{c_1+1} \\ \vdots \end{bmatrix} = \\
 & = \begin{bmatrix} a & b & c & & & \dots & 0 \\ -a & 0 & a & & & & \vdots \\ & \ddots & \ddots & \ddots & & & \\ & & -a & 0 & a & & \\ & & & a & b & c & \\ \vdots & & & -a & 0 & a & \\ 0 & \dots & & & \ddots & \ddots & \ddots \end{bmatrix} \begin{bmatrix} f_1 \\ f_2 \\ \vdots \\ f_{c_1-1} \\ f_{c_1} \\ f_{c_1+1} \\ \vdots \end{bmatrix} \quad (3.19)
 \end{aligned}$$

These matrices are analogous at to the second corner index, c_2 .

It can be seen that, as seen above, the linear system for nodes c_1 to c_2 can be decoupled from the others, while nodes from 1 to $c_1 - 1$ and from $c_2 + 1$ to n still depend on the central region. An analogous approach is taken in the wall-normal direction.

The code allows the buffer zones to use different schemes for spatial derivatives, usually lower orders are desired. A smooth cosine-shaped transition happens from the main scheme to the lower order one in this region.

3.2.5 Time integration

Time integration is performed at a fixed time step by either an explicit Euler, a second order or a forth order Runge-Kutta scheme.

The simplest method is the explicit Euler, shown in the following equation. \mathbf{U}^n is the flow state at time step n and \mathbf{f} is the time derivative of this flow.

$$\mathbf{U}^{n+1} = \mathbf{U}^n + \Delta t \mathbf{f}(\mathbf{U}^n) \quad (3.20)$$

The fourth order Runge-Kutta method is given by the equations below. Despite its higher computational cost at each step, it pays off by being able to take much larger steps without losing stability or precision.

$$\mathbf{U}^{n+1} = \mathbf{U}^n + \frac{\Delta t}{6} (\mathbf{K}_1 + 2\mathbf{K}_2 + 2\mathbf{K}_3 + \mathbf{K}_4) \quad (3.21)$$

$$\mathbf{K}_1 = \mathbf{f}(\mathbf{U}^n) \quad (3.22)$$

$$\mathbf{K}_2 = \mathbf{f}\left(\mathbf{U}^n + \frac{\Delta t}{2}\mathbf{K}_1\right) \quad (3.23)$$

$$\mathbf{K}_3 = \mathbf{f}\left(\mathbf{U}^n + \frac{\Delta t}{2}\mathbf{K}_2\right) \quad (3.24)$$

$$\mathbf{K}_4 = \mathbf{f}(\mathbf{U}^n + \Delta t \mathbf{K}_3) \quad (3.25)$$

The boundary conditions routine is called after each sub-step of the method.

The largest time step possible is defined by the method's numerical stability. For the flow's diffusive characteristics, Eq. 3.26 must be observed, and for the flow's convective characteristics, Eq. 3.27 must be observed. The maximum CFL value depends on the time

integration method chosen. For the fourth order Runge Kutta, a CFL under around 1.3 is stable.

$$\Delta t \leq \frac{Re}{\left(\frac{1}{\Delta x_{min}^2} + \frac{1}{\Delta y_{min}^2} + \frac{1}{\Delta z_{min}^2} \right)} \quad (3.26)$$

$$\Delta t \leq \frac{CFL_{max}}{\left(\frac{1/M+u_{max}}{\Delta x_{min}} + \frac{1/M+v_{max}}{\Delta y_{min}} + \frac{1/M+w_{max}}{\Delta z_{min}} \right)} \quad (3.27)$$

The diffusive stability does not depend on the flow state, only on the mesh and on the Reynolds number, so it is only computed once. The convective stability depends on the flow velocity field and is computed at every step. Equation 3.27 also shows that for very low Mach numbers, closer to an incompressible flow, the time step would have to be significantly reduced due to the increased speed of sound waves compared to the flow velocity, considerably increasing the computational cost.

At very low Mach numbers, the incompressible Navier-Stokes equations would yield a much faster solution at the cost of not being able to identify any acoustic phenomena or the instability modes related to it.

3.2.6 Anti-aliasing filtering

In this type of simulation, high-frequency numerical noise may quickly build up, causing the simulation to diverge from the physical solution.

In a real flow, some mechanisms transport energy from long wavelengths to shorter ones, until the molecular viscosity becomes strong enough to dissipate this energy. In a fully turbulent flow, this is known as the Kolmogorov cascade (KOLMOGOROV, 1991). Simulations down to this scale would require extremely fine meshes and are outside the scope of this work and have a huge computational cost, outside the reach of modern computers for most geometries, even one as simple as an open rectangular cavity.

Eriksson and Rizzi (1985) state that, due to aliasing effects, the motion in the shortest wave length resolved by the mesh is numerically transferred to long wavelengths, which causes the solution to diverge from the physical system.

A numerical low-pass filter attenuates this noise (GAITONDE; VISBAL, 1998). The filter strength can be adjusted before runtime and, ideally, should be as low as possible, minimizing its effect on results. Filtering was turned off close to the boundaries due to the large derivatives present.

This filtering should be enough to dissipate the motion in short wavelengths before they reach the Nyquist frequency limit, which states that a mesh can only resolve wave

lengths of, at least, twice the node spacing and that shorter oscillations would cause aliasing issues.

Filtering is done at the end of each time step and requires solving a tridiagonal linear system for each direction.

It is implemented in a very similar manner to the spatial derivatives. The matrices for the linear system are formed and solved at the end of each time step. The treatment for border and corner nodes is the same as described in Fig. 13 and Eq. 3.19.

The system to be solved is the following:

$$\alpha_f \bar{u}_{i-1} + \bar{u}_i + \alpha_f \bar{u}_{i+1} = \sum_{n=0}^N \frac{a_n}{2} (u_{i-n} + u_{i+n}) \quad (3.28)$$

For this tenth order scheme, the coefficients are:

$$\begin{aligned} a_0 &= \frac{193 + 126\alpha_f}{256}, & a_1 &= \frac{105 + 302\alpha_f}{256}, & a_2 &= \frac{-15 + 30\alpha_f}{64} \\ a_3 &= \frac{45 - 2\alpha_f}{512}, & a_4 &= \frac{-5 + 10\alpha_f}{256}, & a_5 &= \frac{1 - 2\alpha_f}{512} \end{aligned} \quad (3.29)$$

α_f is an adjustable parameter from -0.5, which is maximum filtering, to 0.5, which is no filtering. u_i is the function value at node i and \bar{u}_i denotes this value after filtering.

The spectral function of the filter shows the attenuation for each wavenumber. It is given by:

$$SF(\omega) = \frac{\sum_{n=0}^N a_n \cos(n\omega)}{1 + 2\alpha \cos(\omega)} \quad (3.30)$$

Figure 14 is a plot of this spectral function for various values of α for this tenth order scheme.

3.2.7 Artificial damping

This DNS is used in two distinct parts of this work. Besides being called during the instability analysis, it is also used to generate the base flow.

A fundamental requirement for this base flow to be used for instability analysis is to be steady, i.e., its derivatives with respect to time are null. Given that $\mathbf{f}(\mathbf{U})$ describes the time derivative of the flow \mathbf{U} , a steady state solution \mathbf{U}_0 suitable to be a base flow would yield

$$\mathbf{f}(\mathbf{U}_0) = \mathbf{0} \quad (3.31)$$

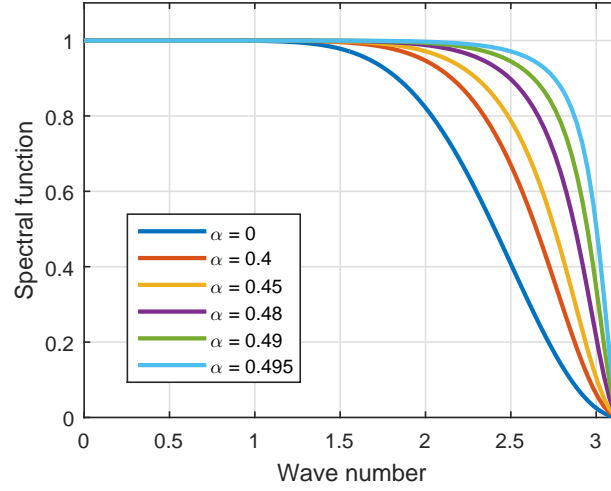


Figure 14 – Spectral function for the tenth order low-pass filter.

Two of the most straightforward methods to obtain \mathbf{U}_0 are:

1. Run the time evolution for a sufficient time to reach a steady flow within a certain tolerance.
2. Use a Newton iteration method to solve the non-linear system.

The first solution works only if all the base flow modes are stable and requires long simulations when close to critical stability conditions. An open cavity flow may not always meet this criterion, as it may be two dimensionally unstable, which would cause the simulation to reach a periodical solution.

At the critical stability condition, the time average of this periodical solution coincides with the base flow, but this is not true for unstable conditions. (SIPP; LEBEDEV, 2007)

The second solution would require a considerable amount of recoding of the DNS and also depends on a good initial guess.

Åkervik et al. (2006) propose a solution based on the first method, called the Selective Frequency Damping (SFD). It works as a low pass filter in the time domain, which damps the unstable modes present in the flow so that a physical steady state is reached by the simulation, even if it is physically unstable.

It is based on a proportional feedback control and works by adding a forcing term to the governing equations.

$$\frac{\partial \mathbf{U}}{\partial t} = \mathbf{f}(\mathbf{U}) - \chi(\mathbf{U} - \mathbf{w}) \quad (3.32)$$

Where \mathbf{w} , ideally, would be the target steady flow, but as it is not available at run time, it is substituted by a time filtered flow obtained by the convolution of \mathbf{U} with a time filtering kernel T .

$$\mathbf{w} = \bar{\mathbf{U}}(t) = \int_{-\infty}^t T(\tau - t, \Delta) \mathbf{U}(\tau) d\tau \quad (3.33)$$

The filtering kernel can be defined as:

$$T(\tau - t, \Delta) = \frac{1}{\Delta} \exp\left(-\frac{\tau - t}{\Delta}\right) \quad (3.34)$$

The cutoff frequency is given by:

$$\omega_c = \frac{1}{\Delta} \quad (3.35)$$

For the implementation, Eqs. 3.33 and 3.34 as rewritten in the equivalent differential form:

$$\frac{\partial \bar{\mathbf{U}}}{\partial t} = \frac{\mathbf{U} - \bar{\mathbf{U}}}{\Delta} \quad (3.36)$$

This equation can be solved along with the actual flow, with few changes to the code and a small increase in the computational cost. Both χ from Eq. 3.32 and Δ from Eq. 3.36 are adjustable parameters.

χ controls the strength of the artificial damping. Low values may cause the system to remain unstable or very close to the critical condition. High values add too much damping, causing the system to take a very long time to converge.

Δ controls the cutoff frequency, which should be lower than the unstable mode's frequency. On the other hand, high values of Δ , therefore low cutoff frequencies, cause a similar effect to a strong damping, increasing the time needed for the solution to reach the steady state.

In summary, the following system of equations is solved through time:

$$\frac{\partial \mathbf{U}}{\partial t} = \mathbf{f}(\mathbf{U}) - \chi(\mathbf{U} - \bar{\mathbf{U}}) \quad (3.37)$$

$$\frac{\partial \bar{\mathbf{U}}}{\partial t} = \frac{\mathbf{U} - \bar{\mathbf{U}}}{\Delta} \quad (3.38)$$

When this system reaches a steady state, \mathbf{U} and $\bar{\mathbf{U}}$ will be equal and the second term of the first equation will vanish. Therefore, \mathbf{U} will represent the physical flow \mathbf{U}_0 , which is steady.

To reduce the computational cost, a fourth order Runge-Kutta scheme may be used to solve for the physical part of the flow, which is only the first term of the right hand side of Eq. 3.37, for its increased stability. While the other parts are solved by the simpler explicit Euler method. Hence, Eq. 3.21 is replaced by:

$$\mathbf{U}^{n+1} = \mathbf{U}^n + \frac{\Delta t}{6} (\mathbf{K}_1 + 2\mathbf{K}_2 + 2\mathbf{K}_3 + \mathbf{K}_4) - \Delta t \chi(\mathbf{U} - \bar{\mathbf{U}}) \quad (3.39)$$

With Eqs. 3.22 to 3.25 still used for the sub steps \mathbf{K}_1 to \mathbf{K}_4 . Equation 3.38 is solved through time by:

$$\bar{\mathbf{U}}^{n+1} = \bar{\mathbf{U}}^n + \Delta t \frac{\mathbf{U}^n - \bar{\mathbf{U}}^n}{\Delta} \quad (3.40)$$

It is worth noting that the goal of using this Selective Frequency Damping method is simply obtaining a steady state flow as quickly as possible. Therefore, there is no need for high precision algorithms for the time stepping. The Runge-Kutta algorithm is used because of its excellent stability properties, allowing larger time steps.

It is also possible to use this method only in the buffer zone to mitigate problems at the boundary conditions such as reflections. In this case, χ is multiplied by a parameter η that depends on the position, which varies smoothly from zero at the beginning of the buffer zone to one at the domain boundary.

3.2.8 Domain decomposition and parallel execution

For the parallel execution, the domain is decomposed in slices and each one is sent to a different process. Figure 15 illustrates this decomposition, as done by the 2DECOMP&FFT library, which uses the MPI protocol (LI; LAIZET, 2010).

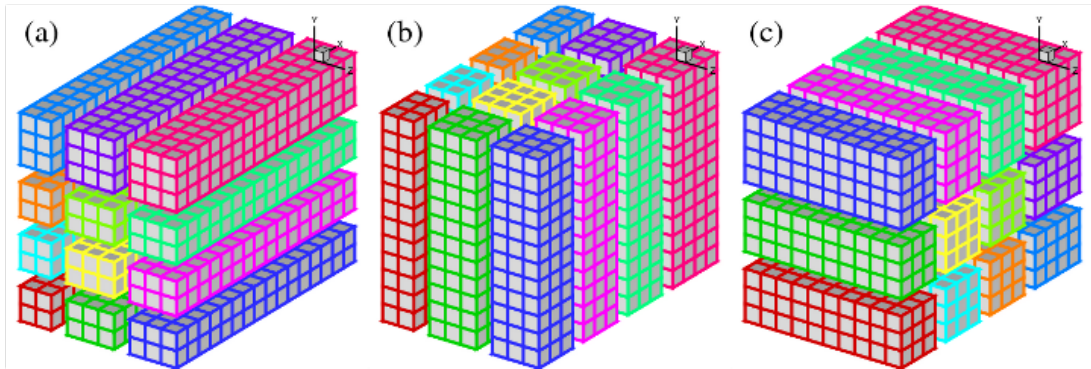


Figure 15 – Scheme of a three dimensional domain decomposed for a grid of 3x4 processes (LI; LAIZET, 2010).

Each slice can be further parallelized by using OpenMP, which allows multiple iterations of loops to be run concurrently.

Each MPI process holds all points of the domain in one direction, but not in the others. For most operations, the decomposition in x is used, i.e., each process can access all points in x for their values of y and z . Which means that for the derivatives and filters in all directions to be computed, the domain has to be transposed once for each direction. This process is illustrated in Fig. 16. An analogous routine is used for the noise filtering in each direction.

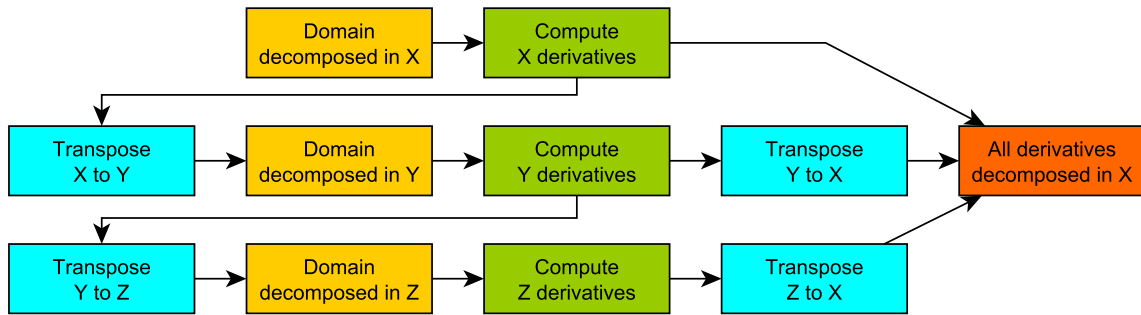


Figure 16 – Flowchart to obtain derivatives of the decomposed domain.

Even though each domain transposition is a memory intensive operation the MPI parallel execution was found to be more efficient.

The number of MPI processes is limited by the geometry. The subroutine for the boundary conditions is called when the domain is decomposed in the stream-wise x direction, i.e. no program instance has access to all values of y and z in the domain. This becomes an issue when computing wall-normal Neumann boundary conditions, as a number of points in the y direction are needed at this step and all these nodes should be contained in the same instance, to avoid communication overhead.

Therefore, care has to be taken so that all points needed for the Neumann conditions are contained in a single instance.

The routines were mostly executed in a computer with 40 physical cores (each providing two logical threads) and 128 GB of RAM. In terms of performance, it was noted that parallelizing the execution by decomposing the domain was usually more efficient than using multiple OpenMP workers, this difference was increased as the mesh grew.

Multiple OpenMP workers were only used when the domain could not be decomposed in many parts due to the geometry. This was usually the case for two-dimensional runs, when the domain could only be decomposed in two or three slices. Three dimensional runs can also be decomposed in the span-wise direction, therefore, OpenMP was rarely used.

It was also noted that it is more efficient to run multiple cases at once, each using fewer processors, than running fewer cases with more processors each. More details are given in Section 4.12.

3.3 Instability Analysis

In order to obtain the oscillation modes of a certain flow, one has to compute the eigenvalues and eigenvectors of its Jacobian matrix. It is, given that the Navier-Stokes equations and all boundary conditions are described by a function \mathbf{f} such that:

$$\frac{\partial \mathbf{U}}{\partial t} = \mathbf{f}(\mathbf{U}) \quad (3.41)$$

Where \mathbf{U} is a vector that contains all flow variables for each node in the mesh, the Jacobian is given by

$$\mathbf{A} = \frac{\partial \mathbf{f}(\mathbf{U})}{\partial \mathbf{U}} \quad (3.42)$$

It can be used to linearize the Navier-Stokes around a given base flow \mathbf{U}_0 . The flow \mathbf{U} , in this case, is given by the base flow plus a disturbance: $\mathbf{U} = \mathbf{U}_0 + \mathbf{u}$. After linearizing, the time evolution of \mathbf{u} is given, analytically, by

$$\mathbf{u}_t = e^{t\mathbf{A}}\mathbf{u}_0 \quad (3.43)$$

\mathbf{u}_0 and \mathbf{u}_t represent the flow state at the initial condition and at time t , respectively.

By computing the eigenvalues \mathbf{L} and eigenvectors \mathbf{V} of \mathbf{A} , it can be rewritten as

$$\mathbf{u}_t = \mathbf{V}e^{t\mathbf{L}}\mathbf{V}^{-1}\mathbf{u}_0 \quad (3.44)$$

By solving the eigenproblem, one can obtain the flow modes and their respective amplification rates and oscillation frequencies. Each column \mathbf{v}_i of \mathbf{V} corresponds to a flow mode and is associated to a value σ_i in \mathbf{L} .

The real part of σ_i represents the amplification rate of each mode. Negative values mean that the mode is stable and will be attenuated; positive values relate to an unstable mode, that will be amplified. In a perfectly linear system, this amplification would happen indefinitely; in real systems, after reaching a certain amplitude, non-linear effects would appear and cause it to saturate.

An interesting way of looking at Eq. 3.44 is to read it from right to left. The last two terms, $\mathbf{V}^{-1}\mathbf{u}_0$, compute how much of each mode is present in the initial disturbance.

The term $e^{t\mathbf{L}}$ shows how much each mode is amplified or attenuated through time. Thus, $e^{t\mathbf{L}}\mathbf{V}^{-1}\mathbf{u}_0$ means how much of each mode is present in the flow at any given time. Finally, by multiplying it by \mathbf{V} , the modes are combined and transformed into the actual flow.

3.3.1 Arnoldi iteration

The size of the Jacobian matrix is $4N \times 4N$ for two-dimensional flows and $5N \times 5N$ for three-dimensional. 4 and 5 are the numbers of variables for each node in a compressible flow, respectively. N being the number of nodes in the domain.

The mesh size is usually in the order of hundreds of points in both the stream-wise and wall-normal directions and a few dozens of points in the span-wise direction. Therefore, the total number of variables to solve for is in the order of 10^5 to 10^6 in two-dimensional cases and 10^6 to 10^7 when accounting for the third dimension.

Due to the implicit differentiation methods used, in which each node in the domain influences every other at all steps, the Jacobian of this system would be a full matrix. At the double precision used by this code, which takes 8 bytes of memory per scalar value, simply storing the Jacobian for a system with 10^6 variables, for example, would take 8×10^{12} bytes, or 8 terabytes of memory.

Because of this, it is not feasible to directly compute the Jacobian matrix. It is also not necessary, as the vast majority of its modes are very stable and not in the scope of this work, only some of the most unstable modes are needed.

The Arnoldi iteration is an algorithm to obtain the eigenvalues and eigenvectors of a system iteratively, it has the very interesting property of not explicitly needing the matrix in order to solve the eigenproblem, all it needs is the capability of multiplying the matrix by arbitrary vectors. (ARNOLDI, 1951)

As implemented, this method has the memory usage scale linearly with the mesh size, instead of quadratically. For the same system with 10^6 variables, if 1000 iterations are used, 8×10^9 bytes, or 8 gigabytes, of memory would be needed for the largest matrix.

The concept behind this method is that by repeatedly multiplying a matrix \mathbf{M} by a vector \mathbf{v} , the eigenvectors of \mathbf{M} that are present in \mathbf{v} will be filtered out depending on their eigenvalues.

After enough iterations, only the eigenvectors corresponding to eigenvalues with the greatest absolute value will remain.

This simple algorithm, known as the power iteration, would be capable of finding a single eigenvector and would take a considerable amount of iterations to converge.

The Arnoldi iteration differs in a way that, after each multiplication, the resulting

vector is projected to be orthonormal to all previous vectors before being multiplied again. This allows multiple eigenvectors to be retrieved. Eigenvalues with the greatest modules tend to converge with fewer iterations.

For further improving results and speeding up convergence, some numerical techniques may be used. The method may be restarted after a fixed number of iterations, using the most unstable mode of a run as the initial disturbance for the next.

Another option for further improvement is the implementation of the Implicitly Restarted Arnoldi method (IRA). (LEHOUCQ; SORENSEN, 1996; RADKE, 1996).

Shift-invert strategies may also be used in conjunction with this method, as done by Gómez et al. (2015). This allows Arnoldi's method to retrieve modes in a specific Region of the complex plane, for example, it could retrieve modes related to acoustic of the flow, which may be more stable than other modes.

3.3.2 Jacobian-free instability analysis

This method was proposed and implemented by Eriksson and Rizzi (1985) for the Euler equations, Edwards et al. (1994) and Chiba (1998) are among the first to implement it for the incompressible Navier-Stokes equations. It is based on Arnoldi's method for solving the eigenproblem. The DNS itself is embedded into the method instead of the Jacobian matrix.

A matrix \mathbf{B} is defined as $e^{t\mathbf{A}}$ from Eq. 3.43, thus, the system becomes

$$\mathbf{u}_t = \mathbf{B}\mathbf{u}_0 \quad (3.45)$$

The Arnoldi iteration is used to obtain the eigenvalues and eigenvectors of \mathbf{B} , which can be easily related to those of \mathbf{A} .

Numerically integrating \mathbf{f} from Eq. 3.41 for a time t is equivalent to multiplying the initial flow by \mathbf{B} , excluding the non-linear terms. It is important to note that the linearized system operates on the disturbance \mathbf{u} around the equilibrium point \mathbf{U}_0 , while \mathbf{f} operates on the whole flow $\mathbf{U} = \mathbf{U}_0 + \mathbf{u}$.

$$\mathbf{U}_0 + \mathbf{u}_t = \mathbf{U}_0 + \mathbf{B}\mathbf{u}_0 = \mathbf{U}_0 + \int_0^t \mathbf{f}(\mathbf{U}_0 + \mathbf{u}_0) dt - N.L.T. \quad (3.46)$$

This is only valid if the base flow \mathbf{U}_0 is an equilibrium point, it is, $\mathbf{f}(\mathbf{U}_0) = \mathbf{0}$. Which, given the numerical nature of this work, may not be completely true, as there are usually some residuals involved when computing the base flow.

To overcome this problem, as well as to reduce the errors from non-linear terms, two numerical integrations are performed, with symmetrical disturbances, as shown in the following equations. To simplify the notation, from now on the integral of \mathbf{f} from 0 to t will be written as \mathbf{F} , which is equivalent to a DNS call.

Equation 3.46 is rewritten as:

$$\mathbf{U}_0 + \mathbf{B}\mathbf{u}_0 \approx \mathbf{U}_0 + \mathbf{F}(\mathbf{U}_0 + \mathbf{u}_0) \quad (3.47)$$

Analogically, by using the opposite disturbance:

$$\mathbf{U}_0 - \mathbf{B}\mathbf{u}_0 \approx \mathbf{U}_0 + \mathbf{F}(\mathbf{U}_0 - \mathbf{u}_0) \quad (3.48)$$

Therefore, subtracting Eq. 3.48 from Eq. 3.47:

$$2\mathbf{B}\mathbf{u}_0 \approx \mathbf{F}(\mathbf{U}_0 + \mathbf{u}_0) - \mathbf{F}(\mathbf{U}_0 - \mathbf{u}_0) \quad (3.49)$$

In this analysis, the initial disturbance \mathbf{u}_0 is given by a normalized vector $\boldsymbol{\zeta}$ multiplied by a scaling factor ε . Equation 3.49 becomes:

$$2\varepsilon\mathbf{B}\boldsymbol{\zeta} \approx \mathbf{F}(\mathbf{U}_0 + \varepsilon\boldsymbol{\zeta}) - \mathbf{F}(\mathbf{U}_0 - \varepsilon\boldsymbol{\zeta}) \quad (3.50)$$

$$\mathbf{B}\boldsymbol{\zeta} \approx \frac{1}{2\varepsilon} (\mathbf{F}(\mathbf{U}_0 + \varepsilon\boldsymbol{\zeta}) - \mathbf{F}(\mathbf{U}_0 - \varepsilon\boldsymbol{\zeta})) \quad (3.51)$$

Small values of ε reduce the non-linear terms, providing better approximations in terms of the truncation error, but are likely to increase the round-off error caused by the computer's precision, which is already critical in this situation, as the disturbances are orders of magnitude smaller than the base flow.

Eriksson and Rizzi (1985) have noted that the error in Eq. 3.51 scales with ε^2 and developed a similar equation, but with fourth order accuracy:

$$\mathbf{B}\boldsymbol{\zeta} \approx \frac{1}{12\varepsilon} [-\mathbf{F}(\mathbf{U}_0 + 2\varepsilon\boldsymbol{\zeta}) + 8\mathbf{F}(\mathbf{U}_0 + \varepsilon\boldsymbol{\zeta}) - 8\mathbf{F}(\mathbf{U}_0 - \varepsilon\boldsymbol{\zeta}) + \mathbf{F}(\mathbf{U}_0 - 2\varepsilon\boldsymbol{\zeta})] \quad (3.52)$$

Note that Eq. 3.52 requires four DNS calls for the numerical integration, instead of just two.

Both Eqs. 3.51 and 3.52 can be used by the Arnoldi iteration as the form to obtain $\mathbf{B}\boldsymbol{\zeta}$. In this work, only the former is used, as it nearly halves the computational cost. Tezuka and Suzuki (2006) have also used this lower order method and noted that the

difference in results from $\varepsilon = 0.01$ to $\varepsilon = 1$ is negligible, leading to the conclusion that even at this lower order of accuracy, the truncation error is very small.

After the iterations are concluded, the eigenvalues and eigenvectors of \mathbf{A} are finally computed. Arnoldi's method converges faster on the eigenvalues that are further away from the origin of the complex plane, which, after the exponential transform, translate into the most unstable modes of the flow.

In summary, the method adds small disturbances to the steady-state flow and uses the DNS to observe how the flow reacts to them. After a series of orthogonal disturbances, the Hessenberg matrix in Arnoldi's method is obtained, which is several orders of magnitude smaller than the flow's Jacobian matrix would be. The eigenvalues and eigenvectors of this matrix are computed and, finally, used to approximate the flow's modes and their respective amplification or attenuation rates. This is shown in the flowchart in Fig. 17.

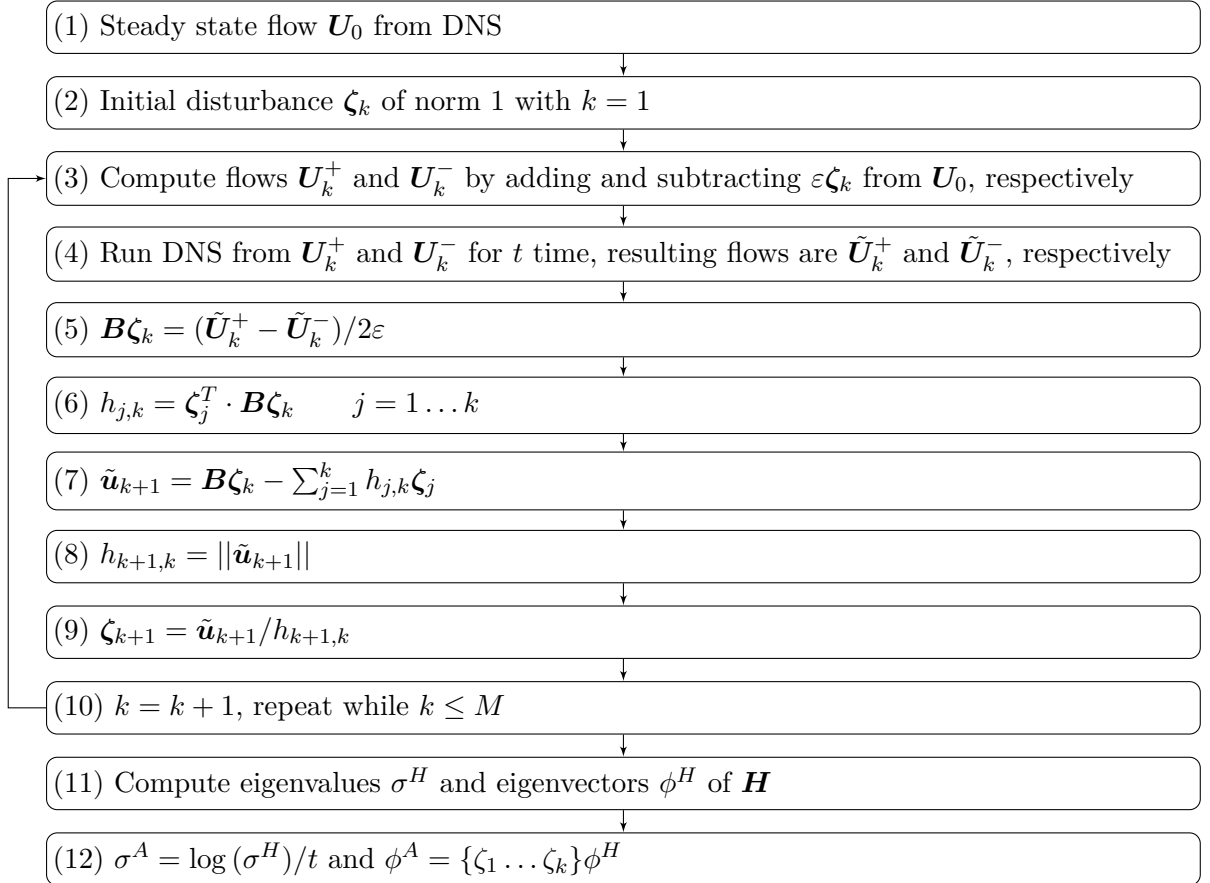


Figure 17 – Flowchart of the Jacobian-free method for computing the flow modes.

In step (3) of Fig. 17, ε controls the perturbation's norm, as noted above. It is worth noting that the number of mesh nodes influences the perturbation's module in each one. In this work, to overcome this issue, the perturbation norm is defined as a fixed parameter multiplied by the square root of the number of nodes in the mesh: $\varepsilon = \varepsilon_0 \sqrt{N}$.

This is done so the RMS of the disturbance is kept constant for any number of variables in the system.

If higher order schemes are used, as Eriksson and Rizzi (1985) have noted, step (5) should be changed accordingly and previous steps should include the extra DNS runs required.

It should also be noted that in step (12), the equation for eigenvalues is not fully reversible for the imaginary part, as the exponential function of a complex number is not injective. This means that the method brings a correct approximation only for the real part of the eigenvalues, related to the amplification rate.

The imaginary part, related to the frequency, must be checked by other means if t is too large, for example by using the DNS to simulate each of the modes identified and observing the oscillation frequencies. The difference between the imaginary part found by the code and the actual value is an integer multiplied by $2\pi/t$.

According to Gómez, Gómez and Theofilis (2014), the time each simulation is run is limited by:

$$\left| \frac{1}{\lambda_i - \lambda_m} \right| < t < \frac{\ln\left(\frac{\varepsilon_{DNS}}{\varepsilon_0}\right)}{\lambda_i} \quad (3.53)$$

Where λ_i is the most stable mode to be accurately retrieved. λ_m is the most stable eigenvalue from the Hessemberg matrix. ε_0 is the magnitude of the disturbance added to the baseflow and ε_{DNS} is the method's truncation error.

This means that the simulation time is limited from below by the separation of the eigenvalues. One can overcome this limitation by simply running more Arnoldi iterations, increasing the Krylov span and, therefore, lowering the value of the most stable mode of the Hessemberg matrix. On the other hand, this increases the size of the Hessemberg matrix, increasing the method's memory usage.

On the other side, the upper limit of this simulation time is given by the code's truncation error, as the disturbances must still be observable after the run is done. Note that this limit only applies for stable modes. One downside of increasing the simulation time, as noted before, is that the imaginary part of the eigenvalues would have to be checked by other means.

Therefore, a choice has to be made: Short simulation times yield more reliable imaginary parts for the eigenvalues but increase the memory footprint of the code as larger Hessemberg matrices are needed. Longer simulation times reduce the memory footprint but would require checking the imaginary parts.

3.3.3 Initial disturbance

The Arnoldi method depends on an arbitrary initial disturbance (ζ_1 from Fig. 17) and there is no single solution for this. Eriksson and Rizzi (1985) use a random vector for the initial disturbance. Chiba (1998) computes it as a random vorticity field, for which the Poisson equation is solved numerically, resulting in the disturbance's stream function.

A good choice for this disturbance is important as the algorithm can only find modes that are contained in it. Modes which are more present initially tend to converge faster. Three types of disturbances were considered: a random vector all over the domain; a random vector multiplied by a weighting function that concentrates it close to the cavity; a known function such as a Gaussian distribution centered close to the cavity.

Random functions such as white noise have a flat spectrum, which may initially be seen as an advantage, but they excite high-frequency modes, which are soon damped out by the numerical low-pass filters, resulting in a quick loss of disturbance energy. Also, they are not deterministic, i.e., might yield multiple results if run multiple times, adding to the complexity of the problem. A Gaussian distribution is deterministic and, if well scaled, may excite all the modes in the scope of this work.

In the span-wise direction, another approach is also possible: sine and cosine functions can be used so that a single span-wise wave number is considered.

For the final code, the Gaussian distribution over the stream-wise (x) and wall-normal (y) directions and a combination of cosines and sines was chosen for the span-wise direction (z). This is shown by the following equations.

$$\rho_1(x, y, z) = \exp\left(-\alpha_x(x - x_0)^2 - \alpha_y(y - y_0)^2\right) \cos(\beta z) \quad (3.54)$$

$$u_1(x, y, z) = \exp\left(-\alpha_x(x - x_0)^2 - \alpha_y(y - y_0)^2\right) \cos(\beta z) \quad (3.55)$$

$$v_1(x, y, z) = \exp\left(-\alpha_x(x - x_0)^2 - \alpha_y(y - y_0)^2\right) \cos(\beta z) \quad (3.56)$$

$$w_1(x, y, z) = \exp\left(-\alpha_x(x - x_0)^2 - \alpha_y(y - y_0)^2\right) \sin(\beta z) \quad (3.57)$$

$$e_1(x, y, z) = \exp\left(-\alpha_x(x - x_0)^2 - \alpha_y(y - y_0)^2\right) \cos(\beta z) \quad (3.58)$$

$$\zeta_1 = [\rho_1, u_1, v_1, w_1, e_1]^T \quad (3.59)$$

α_x , α_y , x_0 and y_0 are adjustable parameters, always chosen in a way to center the disturbance close to the cavity opening. β is the desired wave number in z as will be explained in the next subsection.

Notice that for the span-wise velocity (w), the cosine in z is changed to a sine, causing a phase shift of 90° in this variable. This was done because the flow modes are also expected to present this phase shift. Therefore, the initial disturbance is more likely to excite the desired modes.

3.3.4 Spectral treatment for the span-wise direction

As mentioned before, the span-wise direction is considered periodical, and thus, the initial disturbance is given by sines and cosines. In this implementation, a single wave number in this direction is used each time, allowing for smaller meshes, considerably reducing the computational cost.

There is also the option for the instability analysis code to consider the span-wise direction as spectral, this considerably reduces the number of variables in the system, as all values in z for each x and y are Fourier transformed, and just the value corresponding to the desired wave-number is stored. This is illustrated in Fig. 18.

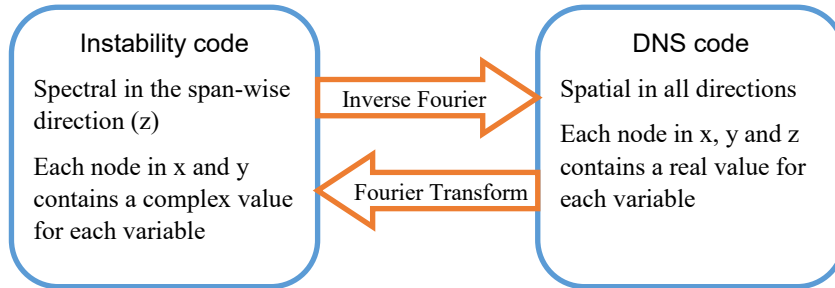


Figure 18 – Flowchart of the interface between the spectral and the spatial parts of the code.

It is also possible to fix the span-wise phase, causing the Fourier transform to return only a real value for each x and y . Note that in this case, for the span-wise velocity, only the imaginary part is kept, causing the 90° phase shift expected from the modes.

3.3.5 Implementation

A code for this routine was implemented in MATLAB[®] and it calls the FORTRAN DNS as necessary. An important perk of this method is that it can be programmed in a very modular manner. The DNS could be easily replaced or updated with only minor changes to the MATLAB[®] code. All parallel processing capabilities of this DNS are kept.

Figure 19 brings a flowchart that illustrates the working of this instability analysis.

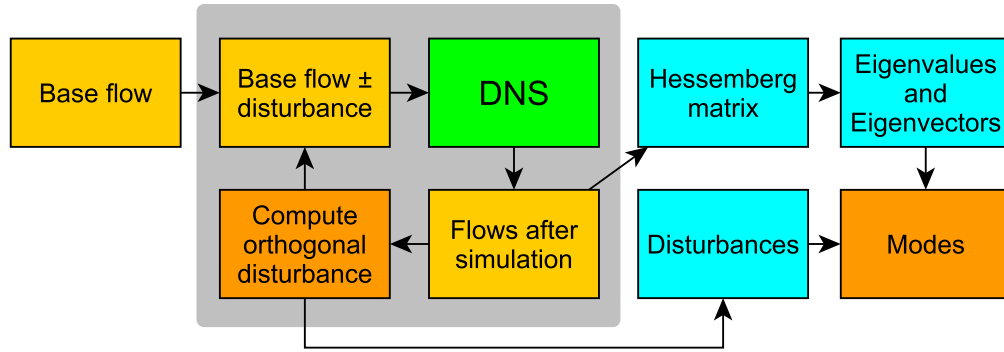


Figure 19 – Flowchart of the Jacobian-free instability analysis implementation.

For each Arnoldi iteration, the DNS is called twice, once for the positive disturbance and once for the negative. Both these calls can be done concurrently, further increasing the code's parallel execution capabilities. Figure 20 illustrates the parallelization scheme of both the instability analysis and the DNS.

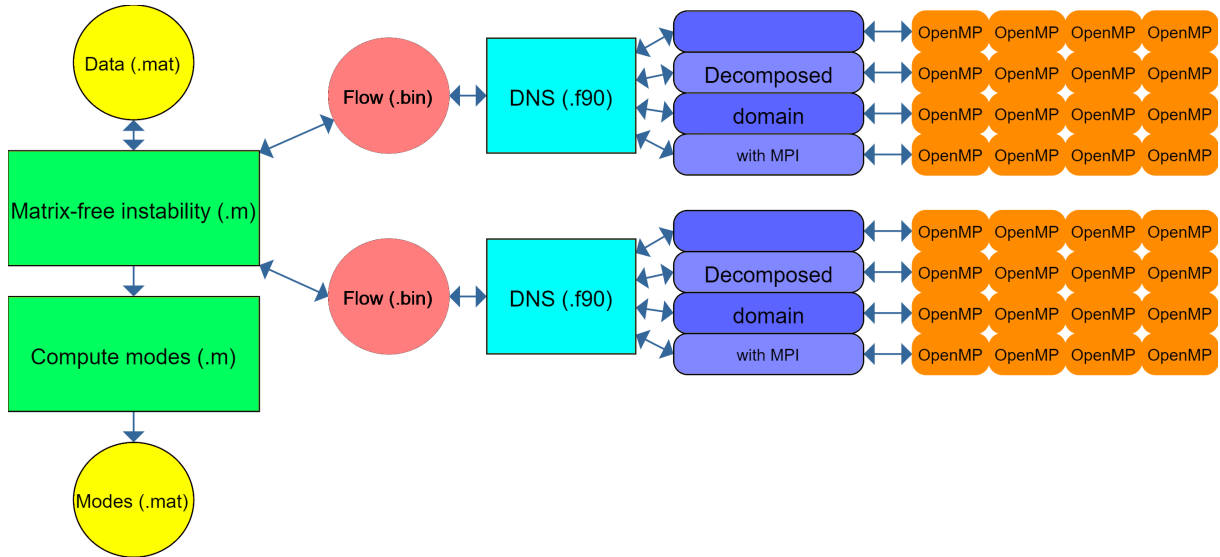


Figure 20 – Overview of code parallelization.

Overall, a 2D instability analysis would take from a few hours to a day, using around 3 GB of RAM, considering the domain sliced in two parts, each with four OpenMP workers. A 3D analysis would take up to a week and consume up to 20 GB of RAM for the largest cases, considering eight slices in the domain, each one run sequentially. The meshes in this example had a few hundred nodes in the stream wise and wall normal directions and 8 span wise nodes, the same order of magnitude as used in the validation and results chapters.

3.3.6 Residual algorithm

For validation purposes, a second method was also used, the Residual Algorithm, which is capable of retrieving the least stable mode. (THEOFILIS, 2000b; THEOFILIS; COLONIUS, 2003; GÓMEZ et al., 2012)

This method consists on placing probes in the domain as the simulation is run from an initial condition towards a steady state. These probes record flow variables as a function of time.

The concept behind this method is that only the least stable mode will remain in the flow after some time, all other modes would have already decayed.

Given that q is the signal obtained by a probe in the domain, one has to observe whether it is a zero-frequency decay or not. A zero-frequency decay happens when the most unstable mode has a real eigenvalue, while an oscillating decay comes from a complex eigenvalue.

In the simpler case, which is the zero-frequency decay, the following equation can be used to obtain the corresponding eigenvalue:

$$\sigma = \frac{\partial^2 q / \partial t^2}{\partial q / \partial t} \quad (3.60)$$

If there is a single frequency present in the signal, then the following equation is valid:

$$\frac{\partial^3 q}{\partial t^3} - 2\sigma \frac{\partial^2 q}{\partial t^2} + (\sigma^2 + \omega_r^2) \frac{\partial q}{\partial t} = 0 \quad (3.61)$$

If evaluated at points when $\partial q / \partial t = 0$, it can be simplified to:

$$\sigma = \frac{1}{2} \frac{\partial^3 q / \partial t^3}{\partial^2 q / \partial t^2} \Big|_{\partial q / \partial t = 0} \quad (3.62)$$

The frequency ω_r can be obtained by other means, such as measuring the signal's peak to peak time.

Many probes are placed on the domain to make sure at least one of them is in a region where the mode's eigenfunction has a considerable magnitude.

One of the challenges of this method is that all other modes in the flow must have decayed enough before the most unstable mode can be retrieved. On the other hand, if the simulation is run for too long, the signal of the most unstable mode will be too small and will not be well resolved due to the computer's rounding errors.

Figure 21 illustrates σ as computed by Eq. 3.60 as the flow is simulated through time. Four probes are present in this example. Two of them were placed where the eigenfunction has a significant magnitude and two, yielding good results; and the other two, where it is close to zero, yielding bad results.

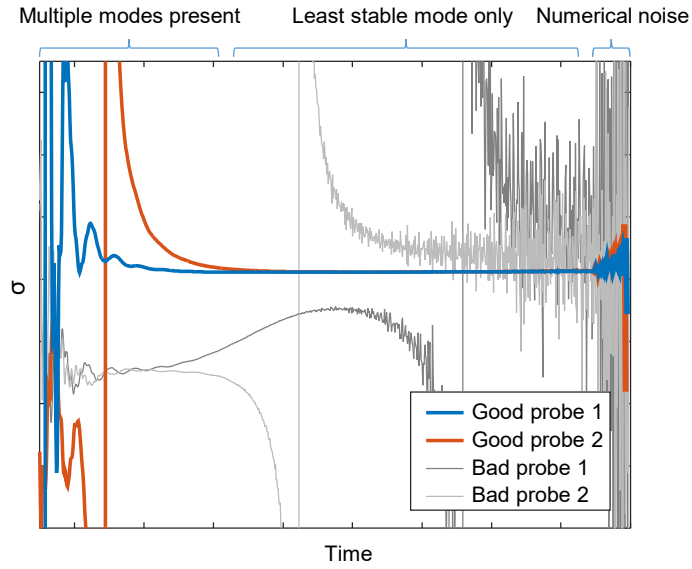


Figure 21 – Example results from the Residual Algorithm.

It can be seen that both probes that were well placed have converged to a single value of σ for most of the simulation, while the value from the other two probes has not converged at all.

Chapter 4

Validation

The validation in this work is divided into four parts. First, the DNS is checked for mesh and domain convergence by using an unsteady flow described by Colonius, Basu and Rowley (1999).

A square lid-driven cavity is also tested and has its base flow compared to the literature.

Second, the parameters in the stability analysis are checked for convergence both for 2D and 3D flows based on Vicente et al. (2014).

Later, the instability analysis is validated by comparing the modes found by the Arnoldi algorithm to the ones retrieved by the Residual Algorithm.

The same analysis is repeated for a lid-driven cavity and the results are compared to the literature.

Finally, open cavity results are compared to runs by Brès and Colonius (2008), Vicente et al. (2014), Sun et al. (2016).

The differentiation scheme used is the 4th compact spectral-like finite differences. Time stepping is done by the 4th order Runge-Kutta method. Buffer zones are placed on all open boundaries and have the finite differences changed to a explicit second order scheme, SFD is also turned on at these regions.

At the end of this chapter, some data on the code performance, run time and memory usage is presented.

4.1 DNS validation

The case used as a reference for the DNS validation is described by Colonius, Basu and Rowley (1999). The cavity's aspect ratio is $L/D = 4$, the boundary's layer thickness related to the cavity length at its leading edge is $L/\theta = 102$, Reynolds and Mach numbers are, respectively, $Re_\theta = 60$ and $Ma = 0.6$. The characteristic flow length is the depth of the cavity, free-flow velocity is also unitary. Note that for this base length, the cavity depth, the actual Reynolds number considered by the code is 1530.

Two meshes were used in this case, they are shown in Tab. 2. A and B are the stretching parameters from Eq. 3.10. The value of η_c was adjusted so that the mesh had its finest region over the cavity opening.

Table 2 – Meshes for the DNS convergence analysis.

| | Mesh 1 | Mesh 2 |
|---------------------|-----------------|-----------------|
| Nodes in x | 300 | 400 |
| Nodes in y | 150 | 200 |
| A_x | 0.99 | 0.99 |
| B_x | 0.5 | 0.5 |
| A_y | 0.995 | 0.995 |
| B_y | 0.3 | 0.3 |
| Nodes in the cavity | 144×52 | 192×70 |

Both meshes cover the same domain, from $x_i = -2$ to $x_f = 15$ and from $y_i = -1$ to $y_f = 4$. The cavity begins at $x_1 = 5.3367$ and ends at $x_2 = 9.3367$.

The cases also share the same parameters for the buffer zone, which adds 20 nodes to each direction in the domain, increasing the node spacing by 20 times from the first node to the last. In this region, the derivative scheme is also smoothly changed to explicit second order finite differences. SFD is also turned on in this region, with parameters $\Delta = 20$ and $\chi = 0.05$ for Eqs. 3.37 and 3.38.

Figure 22 shows this flow at an arbitrary time after the periodic flow has been established.

Figure 23 shows the wall-normal velocity plotted against time at a fixed point at $x = 8.3367$ and $y = 0$. It is, at the flat plate height, three quarters across the opening. The velocity obtained by the two meshes is plotted along with the reference data extracted from the paper by Colonius, Basu and Rowley (1999). Note that the phases were manually adjusted.

For further validation, a square lid-driven closed cavity was also run. The Reynolds number, based on lid length, was set to $Re = 1000$. The Mach number was set to $Ma = 0.1$, as the references found have used the incompressible equations. Two meshes were used,

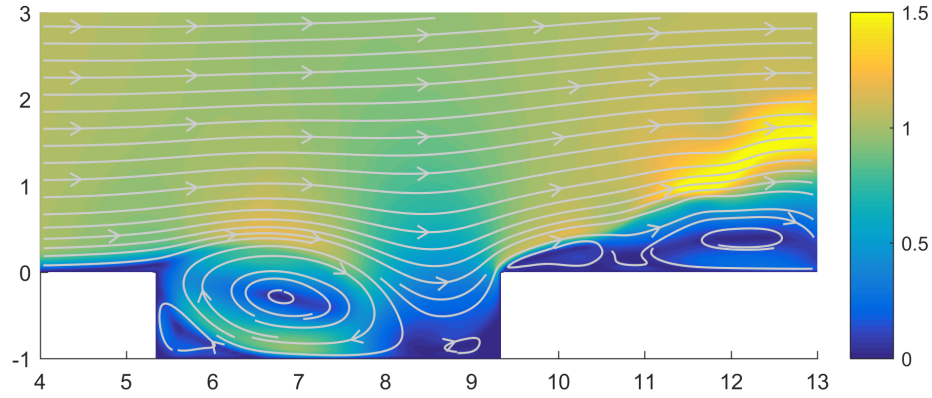


Figure 22 – Velocity magnitude and streamlines of the unsteady flow at an arbitrary time.

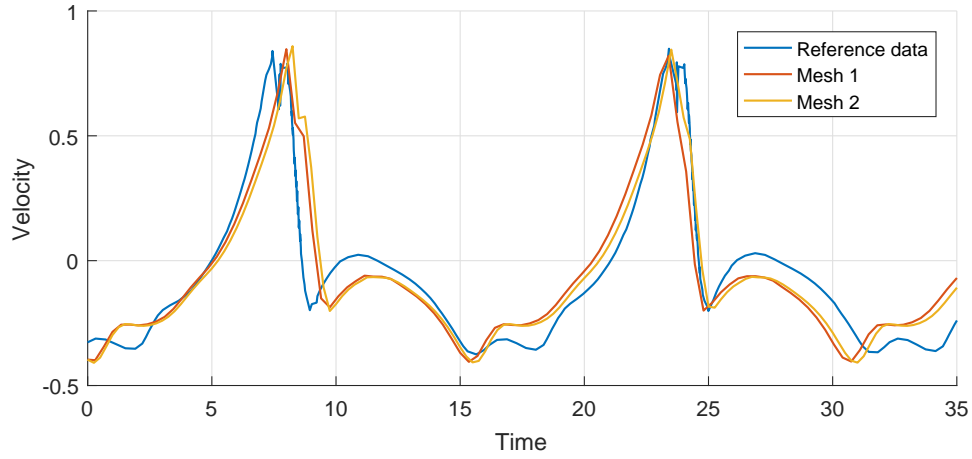


Figure 23 – Velocity plotted against time at a fixed point in an unsteady case.

one with 150 by 150 nodes and other with 250 by 250. The following results are from the finer grid. The steady-state for this case is shown in Fig. 24.

The main vortex has its center located at $(x, y) = (0.5317, 0.5654)$. Ghia, Ghia and Shin (1982) have found this center at $(x, y) = (0.5313, 0.5625)$, Schreiber and Keller (1983) locate it at $(x, y) = (0.5286, 0.5643)$, and Botella and Peyret (1998), at $(x, y) = (0.5308, 0.5625)$.

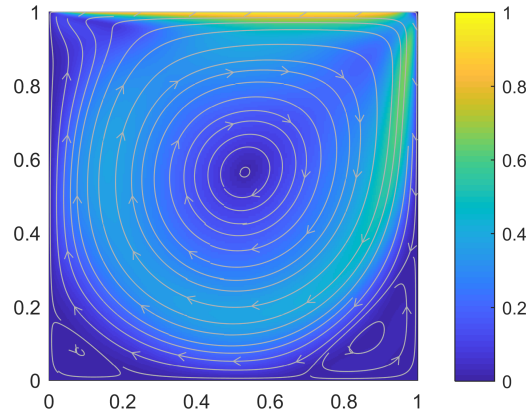


Figure 24 – Velocity magnitude and streamlines of the lid-driven cavity baseflow.

4.2 Two-dimensional mesh independence

To validate the instability analysis, a case described by Vicente et al. (2014) was used.

In this case, the cavity's aspect ratio is $L/D = 2$, the Reynolds number is $Re_D = 1149$ and the boundary layer thickness at the cavity's leading edge is $\theta = 0.0337$. As before, all lengths are normalized by the cavity depth and all velocities, by the inflow velocity.

The reference case has assumed the flow as incompressible. To approximate this assumption, the Mach number was set as $Ma = 0.1$. Low Mach numbers require a shorter time step to maintain numerical stability, which would considerably increase the computational cost. Figure 25 shows the baseflow for the stability analysis.

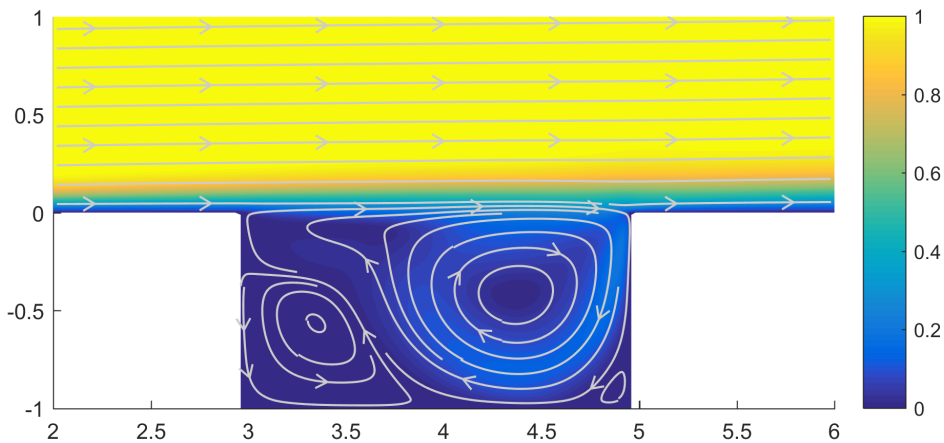


Figure 25 – Velocity magnitude and streamlines of the baseflow.

For the mesh convergence analysis, four meshes have been used, they are shown in Tab 3.

Table 3 – Meshes for convergence analysis.

| | Mesh 1 | Mesh 2 | Mesh 3 | Mesh 4 |
|---------------------|--------|--------|--------|---------|
| Nodes in x | 200 | 300 | 300 | 400 |
| Nodes in y | 150 | 150 | 225 | 300 |
| A_x | 0.99 | 0.99 | 0.99 | 0.99 |
| B_x | 0.5 | 0.5 | 0.5 | 0.5 |
| A_y | 0.995 | 0.995 | 0.995 | 0.995 |
| B_y | 0.3 | 0.3 | 0.3 | 0.3 |
| Nodes in the cavity | 76×52 | 114×52 | 114×79 | 152×105 |

All these meshes are for the same domain, which spans from $x_i = -2$ to $x_f = 10$ and from $y_i = -1$ to $y_f = 4$. The cavity is placed from $x_1 = 2.9597$ to $x_2 = 4.9597$.

Once more, the cases share the parameters for the buffer zone, adding 20 nodes to each direction, increasing the node spacing by 20 times from the first node to the last. The derivative scheme is also smoothly changed to explicit second order finite differences and SFD is also turned on in this region, with parameters $\Delta = 20$ and $\chi = 0.05$.

Figure 26 shows mesh spacing for all meshes in both x and y directions. Dashed lines indicate points of interest, such as the beginning of the flat plate, leading and trailing edges of the cavity for x and the flat plate height for y . Buffer zones are not shown in this figure.

All meshes were run by the instability analysis routine. 400 Arnoldi iterations were used for each run.

The number of time steps was adjusted for each case so that the physical run time was the same. For Meshes 1 to 4, the time steps used were 8.0e-4, 6.0e-4, 5.0e-4 and 4.0e-4, respectively. The number of steps were: 500, 667, 800 and 1000.

Figure 27 shows the eigenvalues obtained for all meshes in the complex plane. All meshes have resulted in similar values for the 12 least stable modes.

The values of the 15 least stable eigenvalues are shown in Tab. 4. Values for all meshes usually match for the first three or four decimal places.

The least stable modes found by each mesh also closely match each other. Figure 28 shows contours of the eigenfunctions found for mode 1 by each mesh. Other modes were also checked and did match, but in the case of complex modes, each mesh has computed them with different phases, which had to be adjusted for comparison.

Note that while this mode presents eigenfunctions with visually the same shape for both density and internal energy, this is not always the case.

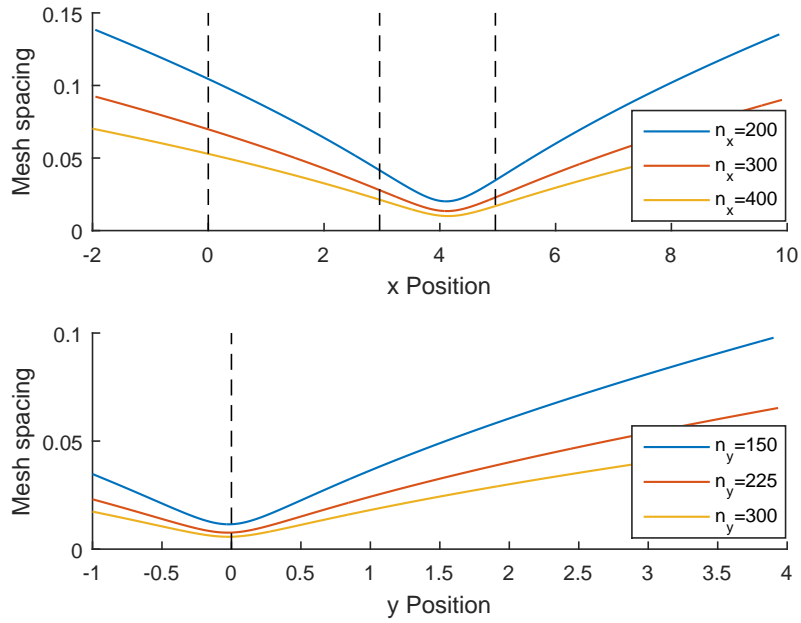


Figure 26 – Mesh spacing for the convergence analysis.

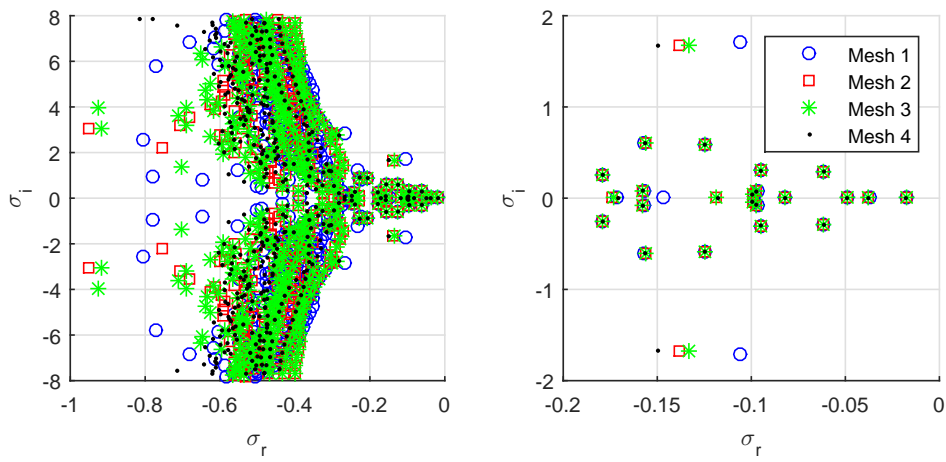


Figure 27 – Eigenvalues computed for the mesh convergence analysis.

Table 4 – Eigenvalues from mesh convergence analysis.

| Mode | Real part | | | | Imaginary part | | | |
|------|-----------|-----------|-----------|-----------|----------------|-----------|-----------|-----------|
| | Mesh 1 | Mesh 2 | Mesh 3 | Mesh 4 | Mesh 1 | Mesh 2 | Mesh 3 | Mesh 4 |
| 1 | -0.017783 | -0.017811 | -0.017819 | -0.017826 | - | - | - | - |
| 2 | -0.037405 | -0.037671 | -0.037696 | -0.037753 | - | - | - | - |
| 3 | -0.049209 | -0.049089 | -0.049176 | -0.049114 | - | - | - | - |
| 4 | -0.061377 | -0.061300 | -0.061370 | -0.061356 | 0.293135 | 0.292746 | 0.291815 | 0.292134 |
| 5 | -0.061377 | -0.061300 | -0.061370 | -0.061356 | -0.293135 | -0.292746 | -0.291815 | -0.292134 |
| 6 | -0.082059 | -0.082041 | -0.081997 | -0.082013 | - | - | - | - |
| 7 | -0.095062 | -0.094852 | -0.095024 | -0.094946 | 0.300320 | 0.300000 | 0.299059 | 0.299369 |
| 8 | -0.095062 | -0.094852 | -0.095024 | -0.094946 | -0.300320 | -0.300000 | -0.299059 | -0.299369 |
| 9 | -0.096846 | -0.097439 | -0.097109 | -0.097378 | 0.071643 | 0.072253 | 0.071825 | 0.072137 |
| 10 | -0.096846 | -0.097439 | -0.097109 | -0.097378 | -0.071643 | -0.072253 | -0.071825 | -0.072137 |
| 11 | -0.098625 | -0.099305 | -0.099338 | -0.099503 | 0.039301 | 0.039409 | 0.039239 | 0.039309 |
| 12 | -0.098625 | -0.099305 | -0.099338 | -0.099503 | -0.039301 | -0.039409 | -0.039239 | -0.039309 |
| 13 | -0.106347 | -0.118776 | -0.119008 | -0.117730 | 1.704951 | - | - | - |
| 14 | -0.106347 | -0.124620 | -0.124782 | -0.124740 | -1.704951 | 0.587605 | 0.585761 | 0.586391 |
| 15 | -0.124803 | -0.124620 | -0.124782 | -0.124740 | 0.588443 | -0.587605 | -0.585761 | -0.586391 |

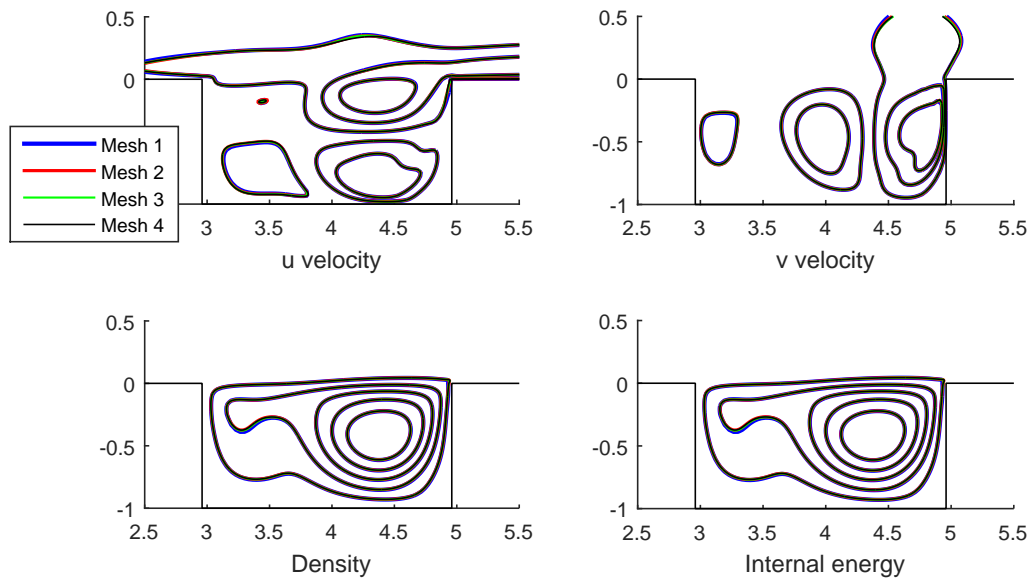


Figure 28 – Eigenfunction of mode 1 for mesh convergence analysis.

4.3 Domain convergence

To make sure the domain size was not influencing the results, three other sizes were used to reproduce the results.

This analysis is based on Mesh 3 of the mesh convergence tests, which is considered as Domain 1. The other domains are enlarged and the mesh is also increased in order to maintain node spacing. All domains have 114 by 52 nodes in the cavity. The parameters for the buffer zone are also shared.

Table 5 brings the details of the domains considered.

Table 5 – Domains for convergence analysis.

| | Domain 1 | Domain 2 | Domain 3 | Domain 4 |
|--------------|----------|----------|----------|----------|
| Initial x | -2 | -3 | -2 | -3 |
| Final x | 10 | 15 | 10 | 15 |
| Initial y | -1 | -1 | -1 | -1 |
| Final y | 4 | 4 | 6 | 6 |
| Nodes in x | 300 | 394 | 300 | 394 |
| Nodes in y | 225 | 225 | 270 | 270 |

It is worth noting that a domain convergence analysis in the z direction is not necessary as the domain is periodical in this direction and the size chosen depends on the wavenumbers to be observed.

Figure 29 shows the eigenvalues obtained for all meshes in the complex plane. The first 8 modes of all domains match.

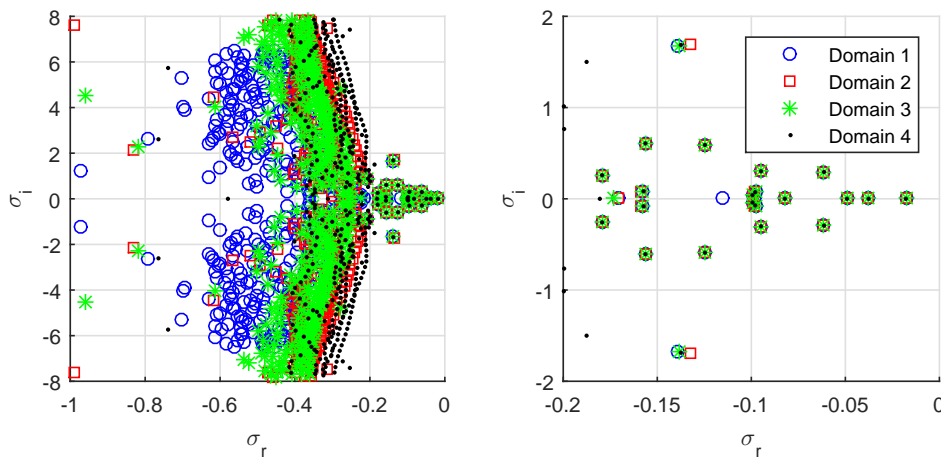


Figure 29 – Eigenvalues computed for the domain convergence analysis.

The 11th mode of Domain 1 matches the eigenfunction of the 9th mode of the other

domains, meaning that the smaller domain has miscalculated its eigenvalue as being more stable. See Fig. 30.

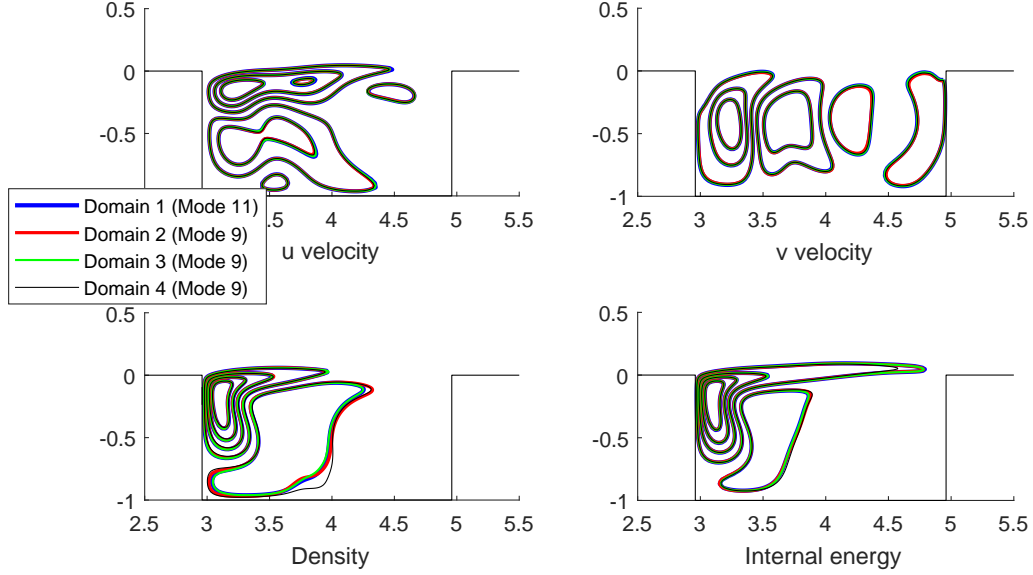


Figure 30 – Eigenfunction of the 9th mode for different domains.

From the 12th mode onwards, eigenfunction contours start reaching the end of the domain and beginning of the buffer zone, which explains the different results when the domain is changed.

Figure 31 shows the eigenfunction for u velocity of Mode 12. Note that, despite having roughly the same shape, the eigenfunction's absolute value is not close to zero at the outflow boundary. Note that as this is a complex mode, the phases had to be adjusted before the modes could be compared.

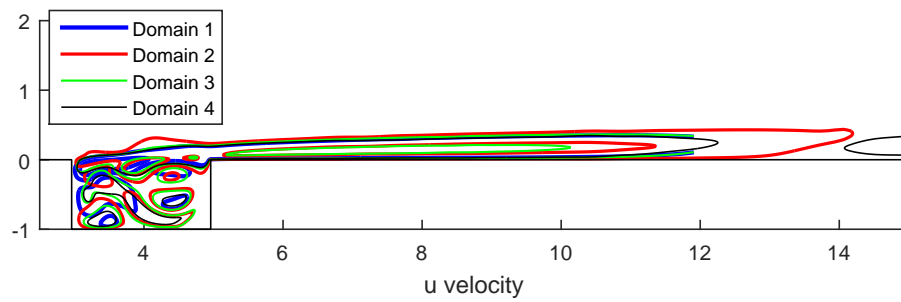


Figure 31 – Eigenfunction of the 12th mode for different domains.

Figure 32 shows the normalized absolute value of the u eigenfunction for modes 1, 4, 8 and 12 at a fixed $y = 0.01$. It can be seen that the eigenfunctions for the least

stable modes have already decayed considerably at the domain outflow, while it still has a considerable magnitude for mode 12.

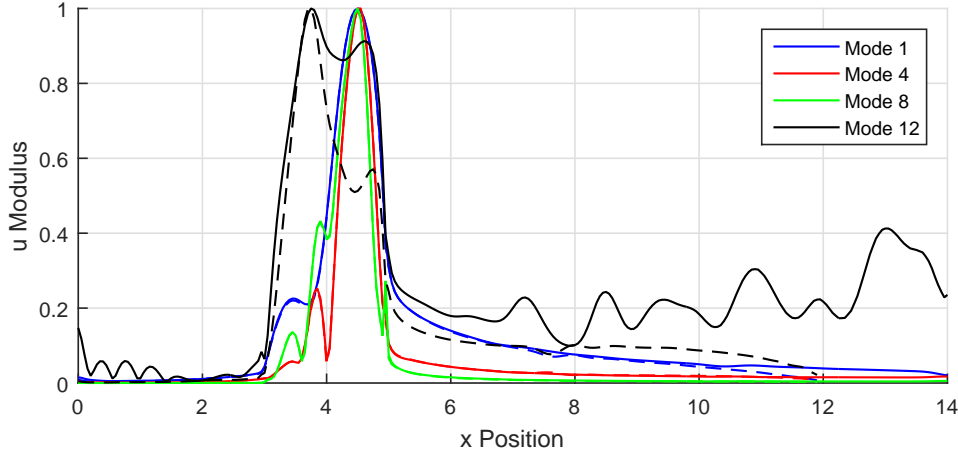


Figure 32 – Eigenfunction modulus of modes 1, 4, 8 and 12 at a fixed height. Dashed lines are for Domain 1 and full lines are for Domain 4.

At the end of the next subsection, this analysis is repeated with more Arnoldi iterations.

4.4 Arnoldi method convergence in two-dimensional analysis

After checking mesh and domain, the next step is to make sure the parameters chosen for the instability analysis algorithm are not significantly influencing the results. Three parameters are to be analyzed:

- ε_0 , which controls the magnitude of the disturbance at each Arnoldi iteration.
- nT , the number of time steps the DNS is run at each call.
- M , the number of Arnoldi iterations.

4.4.1 Disturbance magnitude

For this part of the analysis, Mesh 2 of Tab. 3 was chosen as base. Initially, this case was run with $\varepsilon_0 = 1e-5$. $1e-2$, $1e-3$, $1e-4$ and $1e-7$ were also used for validation purposes.

Figure 33 shows the resulting eigenvalues for the $1e-2$, $1e-3$, $1e-5$ and $1e-7$ cases. Most values were only slightly modified, even in the most stable part of the spectrum.

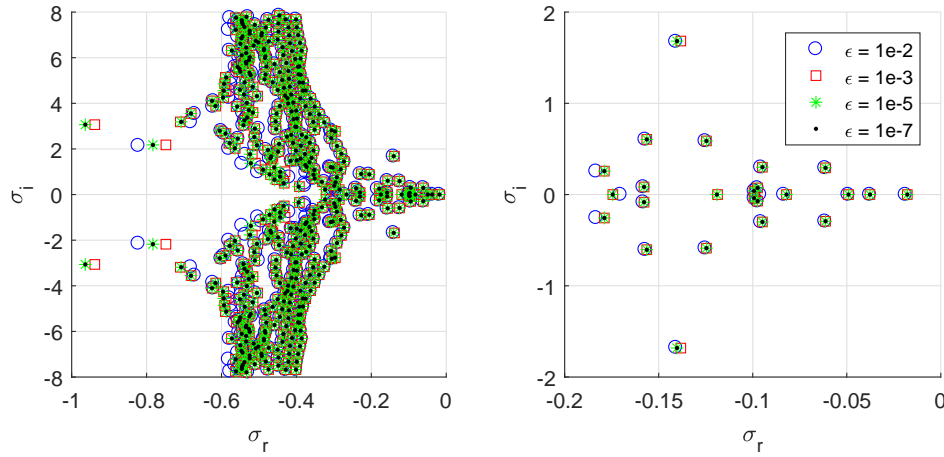


Figure 33 – Eigenvalues computed for the independence analysis of the disturbance magnitude.

Table 6 shows the 3 least stable eigenvalues. Note that the results from the two smallest disturbances match each other up to 7 decimal places in these cases, despite the difference of two orders of magnitude.

Table 6 – Eigenvalues from the disturbance magnitude convergence analysis.

| Mode | $\varepsilon_0 = 1e-2$ | $\varepsilon_0 = 1e-3$ | $\varepsilon_0 = 1e-4$ | $\varepsilon_0 = 1e-5$ | $\varepsilon_0 = 1e-7$ |
|------|------------------------|------------------------|------------------------|------------------------|------------------------|
| 1 | -0.0188047204 | -0.0178210232 | -0.0178117175 | -0.0178116163 | -0.0178116254 |
| 2 | -0.0377751452 | -0.0376719903 | -0.0376773347 | -0.0376773256 | -0.0376773526 |
| 3 | -0.0492358962 | -0.0490902776 | -0.0490870367 | -0.0490870253 | -0.0490870251 |

Figure 34 shows the eigenfunction of the least stable mode. Note that despite the similar eigenvalues, the eigenfunction retrieved by the greatest disturbance differs greatly from the others, especially in the velocity fields.

If the same image is plotted for mode 2, a similar effect happens. However, for mode 3 the eigenfunction retrieved is considerably similar for all cases, despite the five orders of magnitude gap, as can be seen in Fig 35.

4.4.2 Flow simulation time at each iteration

During the mesh convergence analysis, 667 DNS time steps were taken at each call. The algorithm was also run for 200, 400 and 1000 steps. Fig. 36 shows the spectra for these cases. All cases were run for 400 Arnoldi iterations.

It can be seen that the $nT = 200$ case is not converged, as it has resulted in a different set of eigenvalues. The $nT = 400$ case diverges at the 3rd mode. The other two

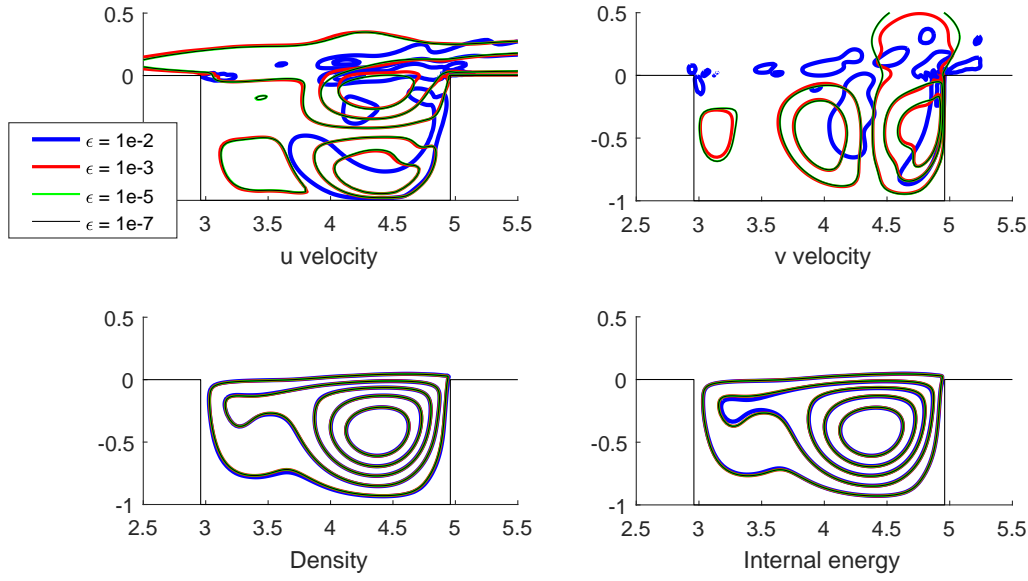


Figure 34 – Eigenfunction of mode 1 for the convergence analysis of the disturbance magnitude.

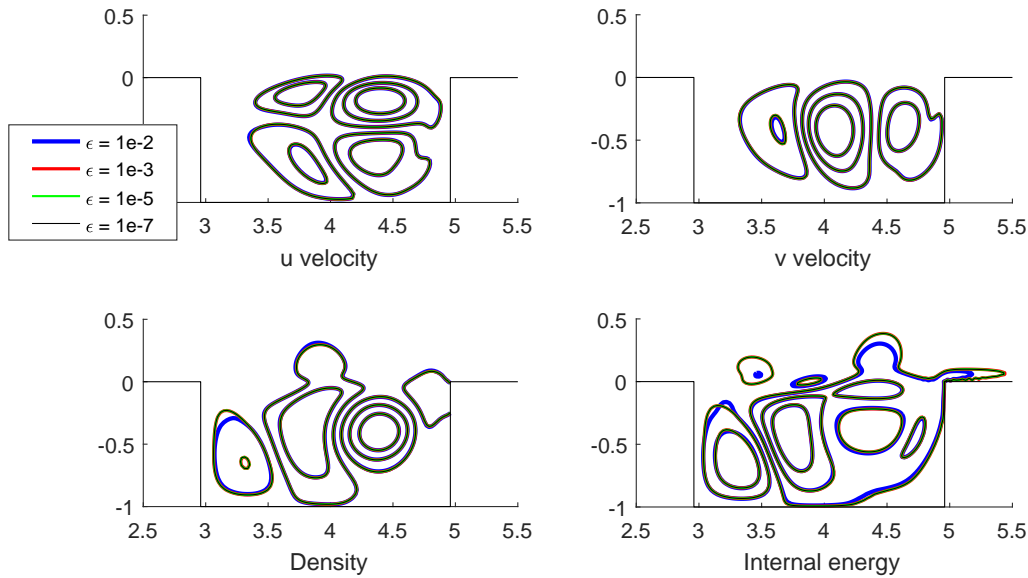


Figure 35 – Eigenfunction of mode 3 for the convergence analysis of the disturbance magnitude.

results match, usually up to the 8th decimal place for the first few eigenvalues. From the 13th mode onwards, the $nT = 667$ case also starts diverging.

By plotting the eigenfunctions in Fig. 37, it can be seen that, as in the ε_0 convergence analysis, despite correctly computing the first eigenvalue up to 4 decimal places, the $nT = 200$ case has failed to find the corresponding eigenfunction.

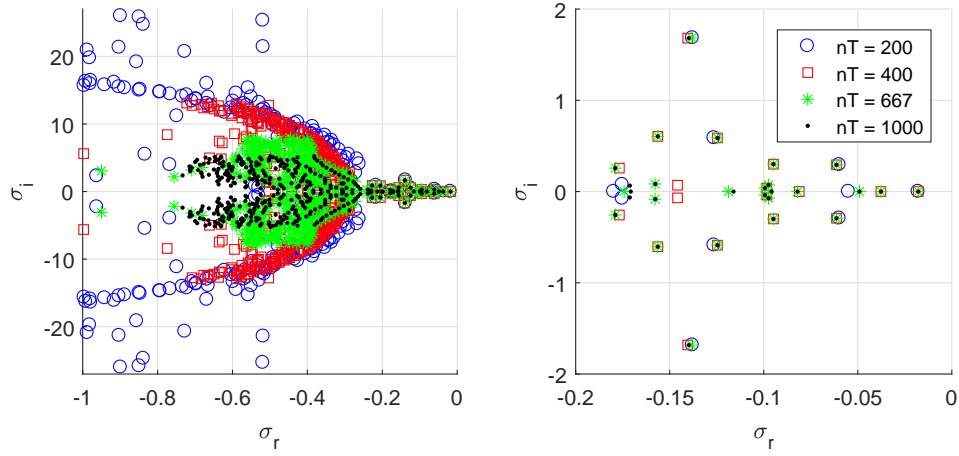


Figure 36 – Eigenvalues computed for the convergence analysis of the number of DNS steps.

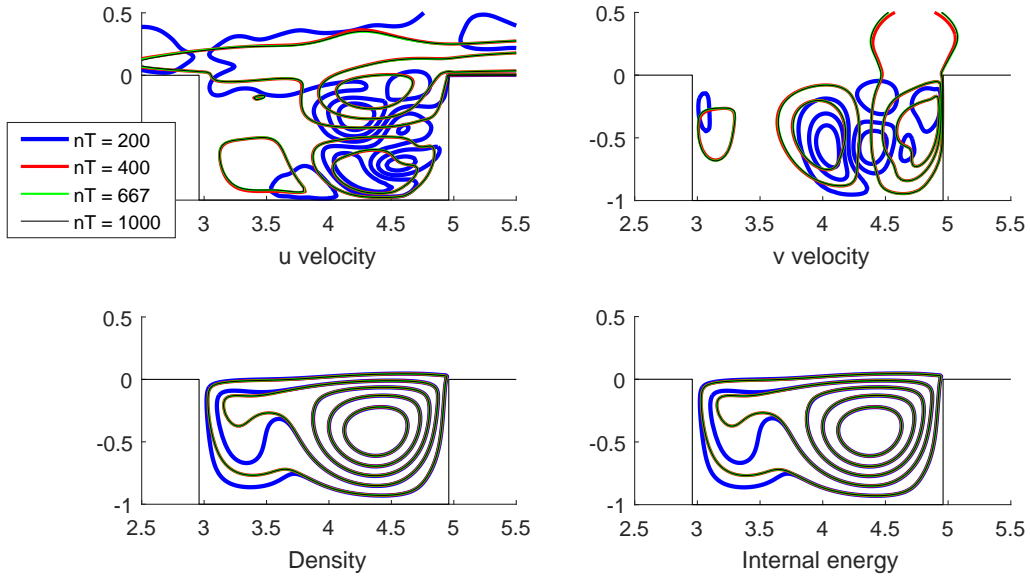


Figure 37 – Eigenfunction of mode 1 for the convergence analysis of the number of DNS steps.

The range of values for σ_i reduces as the number of steps is increased, due to the last equation in the flowchart of Fig 17. This means that smaller values of nT have the advantage of being able to resolve a wider spectrum of modes.

This case has a particularly short time step for the DNS due to the low Mach number. At higher Mach numbers, the amount of time steps can be significantly reduced due to the increased step length.

Back to the $nT = 667$ case, now the convergence of the number of Arnoldi iterations, M , was checked. Figure 38 shows the evolution of the first 30 eigenvalues as the iterations

are run.

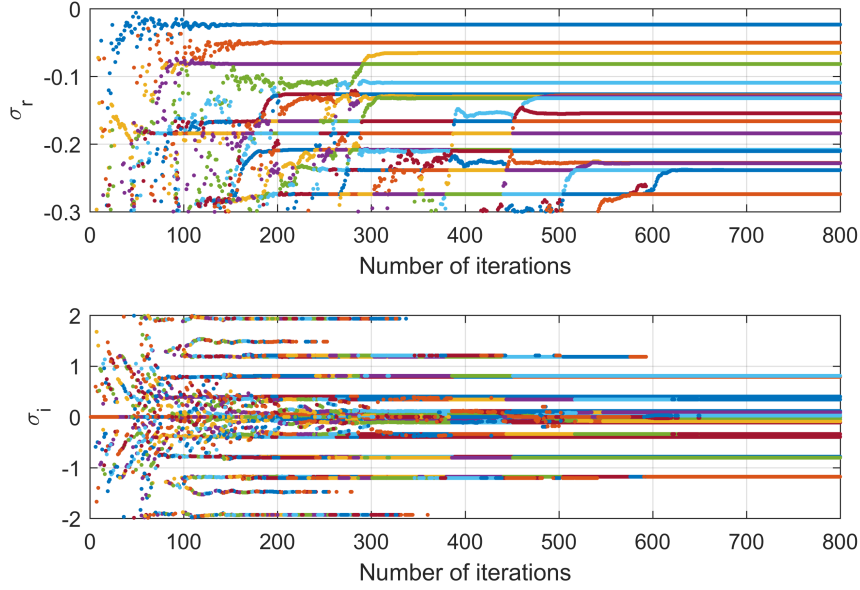


Figure 38 – Eigenvalues computed for the convergence analysis of the number of Arnoldi iterations.

At the end of 400 iterations, the 12 least stable eigenvalues are already converged. The first eigenvalue visually converges around the 150th iteration.

Figure 39 confirms the convergence of the first eigenfunction after 200 Arnoldi iterations. While Fig 40 shows that the second eigenfunction has converged after 300 iterations.

Note that the convergence of the number of Arnoldi iterations and the number of DNS time steps at each iteration are closely related, as seen in Eq. 3.53. Its lower boundary, which states that the shortest simulation time that yields accurate modes, is given by:

$$\left| \frac{1}{\lambda_i - \lambda_m} \right| < t \quad (4.1)$$

λ_i is the most stable mode to be accurately retrieved. λ_m is the most stable eigenvalue from the Hessemberg matrix. To meet this condition, two actions are possible:

1. Increase the physical time t by increasing the number of DNS time steps
2. Increase the Krylov span M , so that λ_m becomes more negative

These possibilities are discussed in the next section.

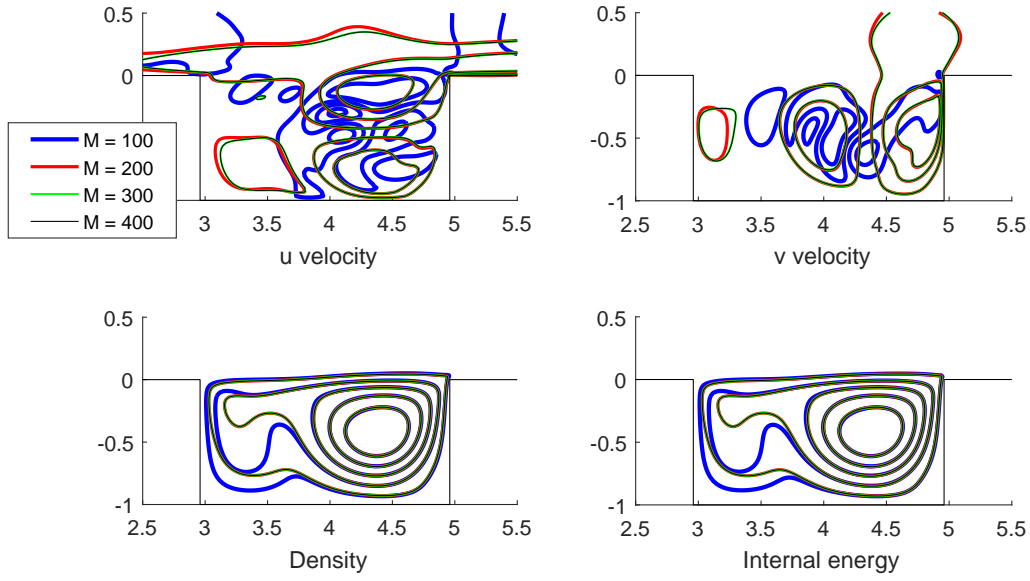


Figure 39 – Evolution of eigenvalues as the Arnoldi method is iterated.

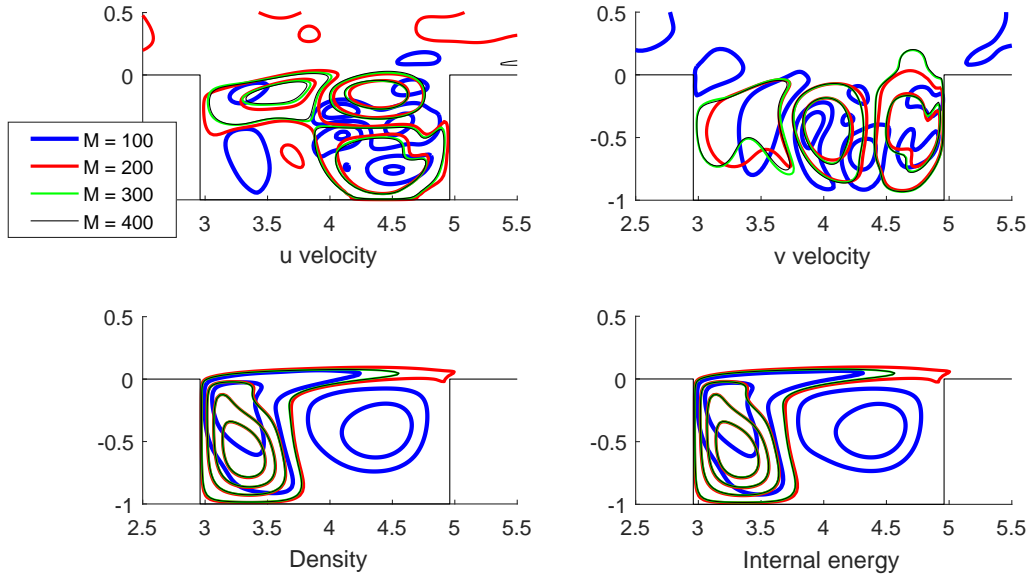


Figure 40 – Eigenfunction of mode 2 for the convergence analysis of the number of Arnoldi iterations.

4.4.3 Number of Arnoldi iterations

The cases from the domain convergence analysis were run again with more Arnoldi iterations. Previously, 400 iterations were used, these new results have used 600.

Figure 41 shows the eigenvalues obtained for all meshes in the complex plane. The

first 8 modes of all domains match.

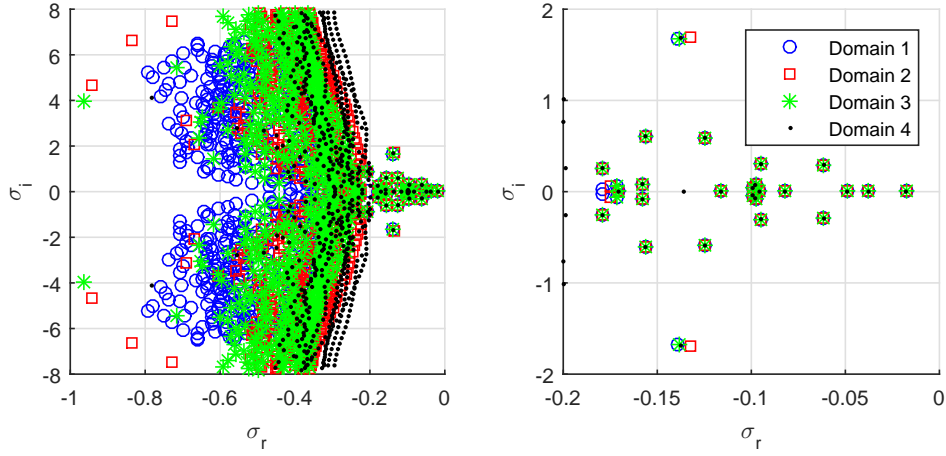


Figure 41 – Eigenvalues computed for the domain convergence analysis with more Arnoldi iterations.

It can be seen that more eigenvalues match when more iterations are used. Figure 42 shows the eigenfunction for u velocity of Mode 12. This time, the results are much closer, leading to the conclusion that the bottleneck for that analysis was not only the domain, but rather also the number of iterations.

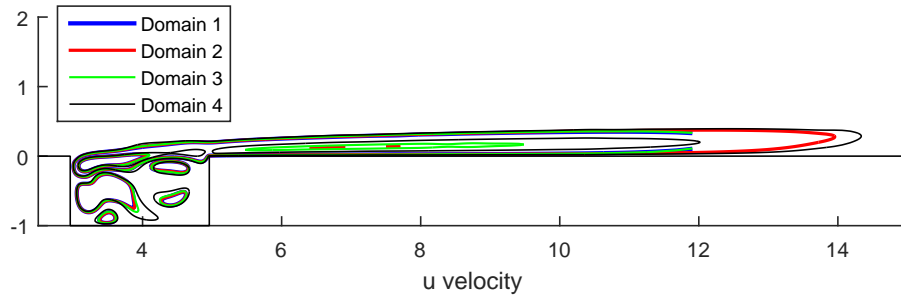


Figure 42 – Eigenfunction of the 12th mode for different domains with more Arnoldi iterations.

Figure 43 shows the normalized absolute value of the u eigenfunction for mode 12, comparing Domains 1 and 4 with both 400 and 600 iterations. The larger domain with the least iterations does not match the other results. It can be concluded that larger domains take longer to converge. This may be due to the relatively large absolute value of this eigenfunction close to the outflow boundary.

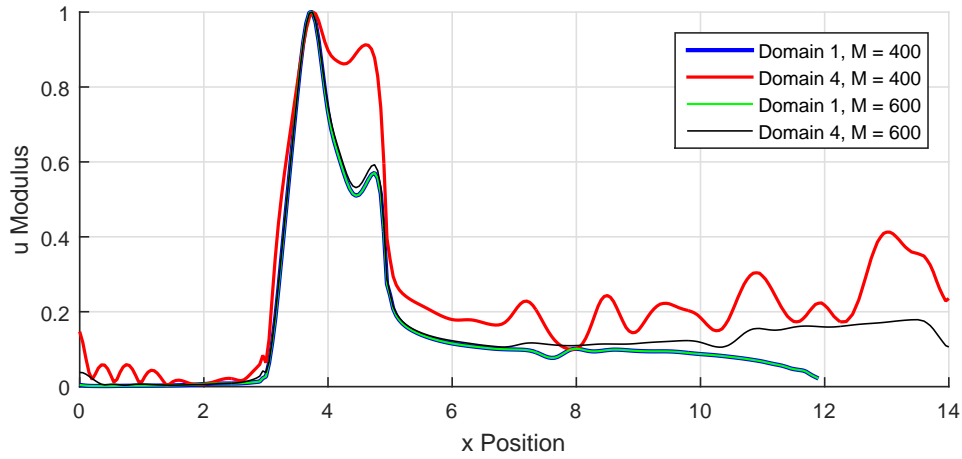


Figure 43 – Eigenfunction modulus of mode 12 at a fixed height for two domains and two numbers of Arnoldi iterations.

4.5 DNS time steps and Arnoldi iterations trade-off

As noted by Gómez, Gómez and Theofilis (2014) and mentioned in Chapter 3, there is a trade-off between the DNS run time and the number of Arnoldi iterations needed for convergence. Longer run times require less iterations for similar results at the most unstable modes.

Several combinations of these parameters were run to check for an optimal point. The open cavity from the two-dimensional validation was selected as base. The numbers of DNS time steps chosen were: 50, 100, 500, 1000, 5000 and 10000. The amount of Arnoldi iterations was chosen so that a total of a million time steps were performed at each case, accounting for both runs at each iteration.

Figure 44 shows the evolution of the relative eigenvalue error for each run as the method is iterated, the last value in each series is used as base. The convergence for both cases with a shorter time span stalls earlier than the other cases. Overall, the runs with 1000 and 500 time steps yielded the best performance. The first mode is shown in the largest plot, this trend is also observed in modes 2 to 9.

Overall, if longer run times at each iteration are used, the following upsides are obtained:

- Better convergence if enough steps are run
- Lower memory usage

On the other hand, shorter time spans present the following upsides:

- Faster convergence initially
- A larger span of imaginary parts is retrieved accurately

Once more, it is worth noting that these numbers of time steps are only valid for this specific flow and mesh combination. To make this analysis more general, the physical flow time must be considered. 500 and 1000 time steps correspond to 0.3 and 0.6 non-dimensional time units, respectively. This is the number to keep in mind when choosing the amount of time steps to be use.

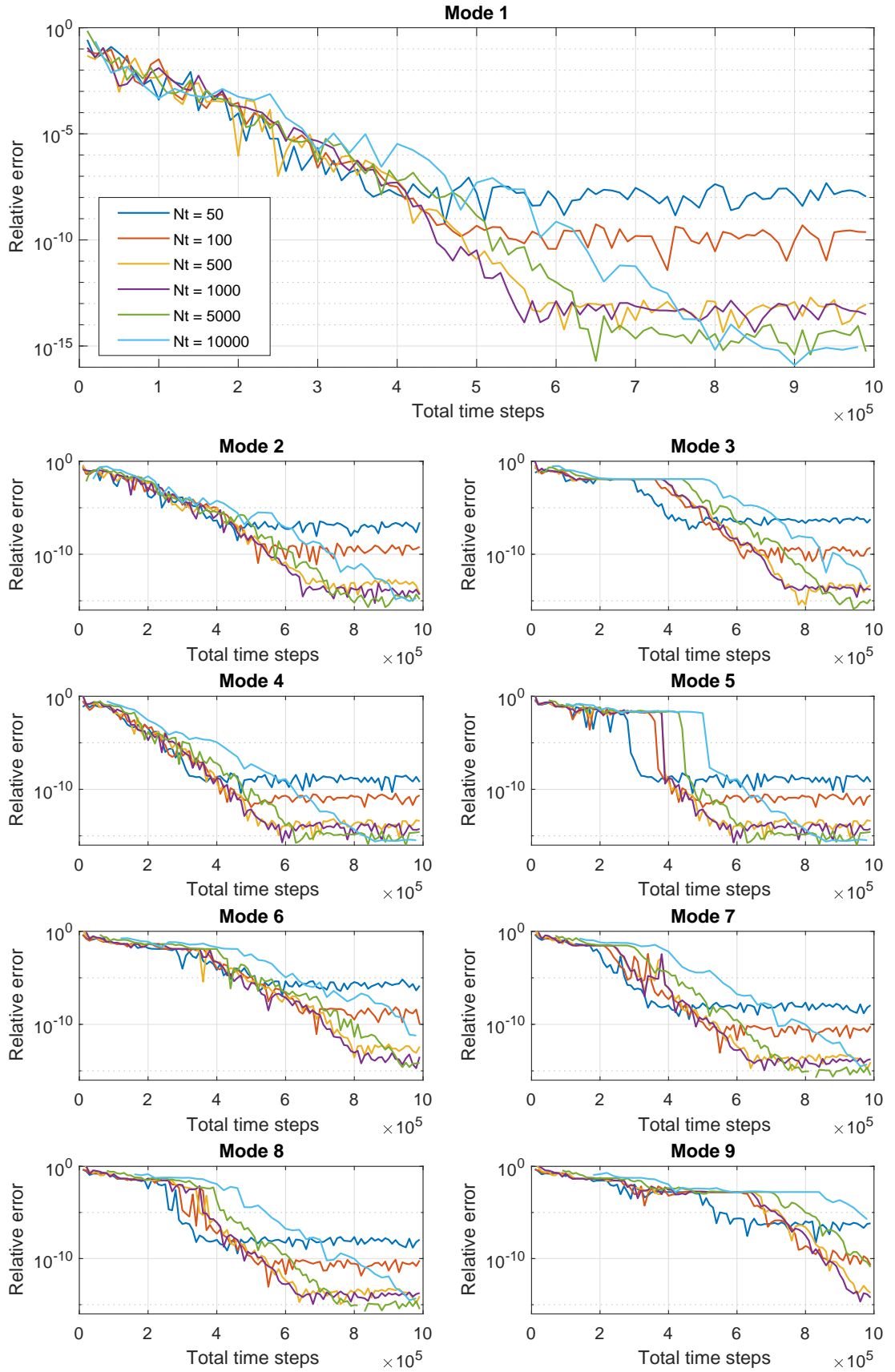


Figure 44 – Relative eigenvalue error versus total number of time steps for modes 1 to 9.

4.6 Three-dimensional mesh independence

For the three-dimensional convergence analysis, Mesh 2 from Tab. 3 was used in the stream-wise and wall-normal directions (x and y). The span-wise direction (z) was represented by a uniform mesh, with either 4, 8 or 12 nodes.

The span-wise direction was treated as both spatial and spectral by the instability code and the results were also compared. 800 Arnoldi iterations were used, each with 500 DNS time steps.

Figure 45 compares the eigenvalues retrieved with 4, 8 and 12 nodes in the z direction with the spectral treatment, the case with 8 nodes was also run without the spectral treatment for z , allowing harmonics to appear. The same data is shown in Tab. 7 for the first 10 modes. Vicente et al. (2014) place the first eigenvalue as $\lambda_1 = 0.00011 \pm 0.17208i$.

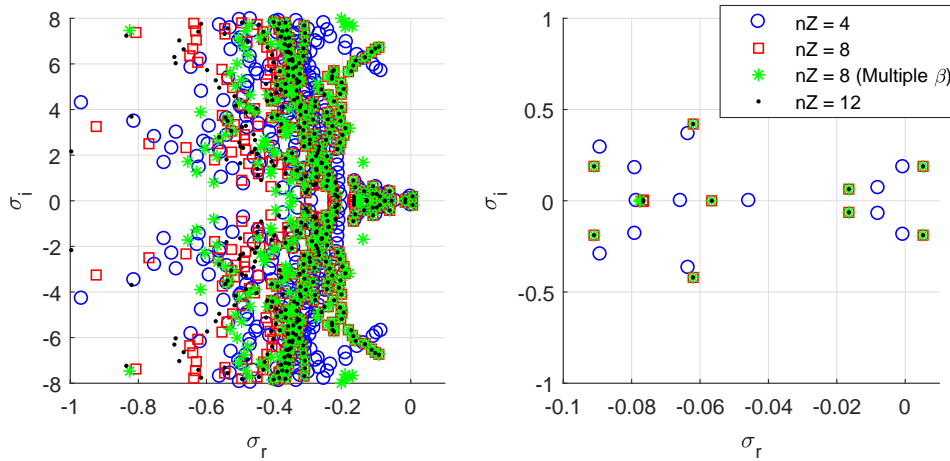


Figure 45 – Eigenvalues computed for the mesh convergence analysis for various counts of span-wise nodes.

Next, the real part of first mode from each case was plotted and is shown in Fig. 46. Note that the phases were adjusted to match. Once more, apart from the coarsest mesh, the results agree with each other. Figure 47 shows the density eigenfunction in the form of isosurfaces.

Back to Tab. 7, in the multiple β case, the complex conjugate modes 12 and 13 have matched modes 14 and 15, respectively. By plotting their respective eigenfunctions in Fig. 48, it can be seen that it has shifted in the span-wise direction from one mode to the other. This happens because, in this case, the phase in this direction is not fixed. On the other hand, when the spectral treatment is used in this direction, this kind of phase shift is not possible.

Table 7 – Eigenvalues from the 3D mesh convergence analysis.

| Mode | nZ = 4 | nZ = 8 | nZ = 8 (Multiple β) | nZ = 12 |
|------|------------------|------------------|----------------------------|------------------|
| 1 | -0.0006 +0.1850i | 0.0052 +0.1886i | 0.0052 +0.1886i | 0.0052 +0.1886i |
| 2 | -0.0006 -0.1850i | 0.0052 -0.1886i | 0.0052 -0.1886i | 0.0052 -0.1886i |
| 3 | -0.0079 +0.0706i | -0.0165 +0.0636i | -0.0165 +0.0636i | -0.0165 +0.0636i |
| 4 | -0.0079 -0.0706i | -0.0165 -0.0636i | -0.0165 -0.0636i | -0.0165 -0.0636i |
| 5 | -0.0457 | -0.0566 | -0.0566 | -0.0566 |
| 6 | -0.0634 +0.3666i | -0.0620 +0.4203i | -0.0620 +0.4203i | -0.0621 +0.4202i |
| 7 | -0.0634 -0.3666i | -0.0620 -0.4203i | -0.0620 -0.4203i | -0.0621 -0.4202i |
| 8 | -0.0657 | -0.0766 +0.0042i | -0.0776 +0.0040i | -0.0766 +0.0046i |
| 9 | -0.0786 | -0.0766 -0.0042i | -0.0776 -0.0040i | -0.0766 -0.0046i |
| 10 | -0.0790 +0.1801i | -0.0910 +0.1888i | -0.0910 +0.1888i | -0.0910 +0.1887i |
| 11 | -0.0790 -0.1801i | -0.0910 -0.1888i | -0.0910 -0.1888i | -0.0910 -0.1887i |
| 12 | -0.0869 +5.6948i | -0.0937 +6.7295i | -0.0937 +6.7295i | -0.0937 +6.7562i |
| 13 | -0.0869 -5.6948i | -0.0937 -6.7295i | -0.0937 -6.7295i | -0.0937 -6.7562i |
| 14 | -0.0892 +0.2928i | -0.1001 +0.2928i | -0.0937 +6.7295i | -0.1001 +0.2928i |
| 15 | -0.0892 -0.2928i | -0.1001 -0.2928i | -0.0937 -6.7295i | -0.1001 -0.2928i |

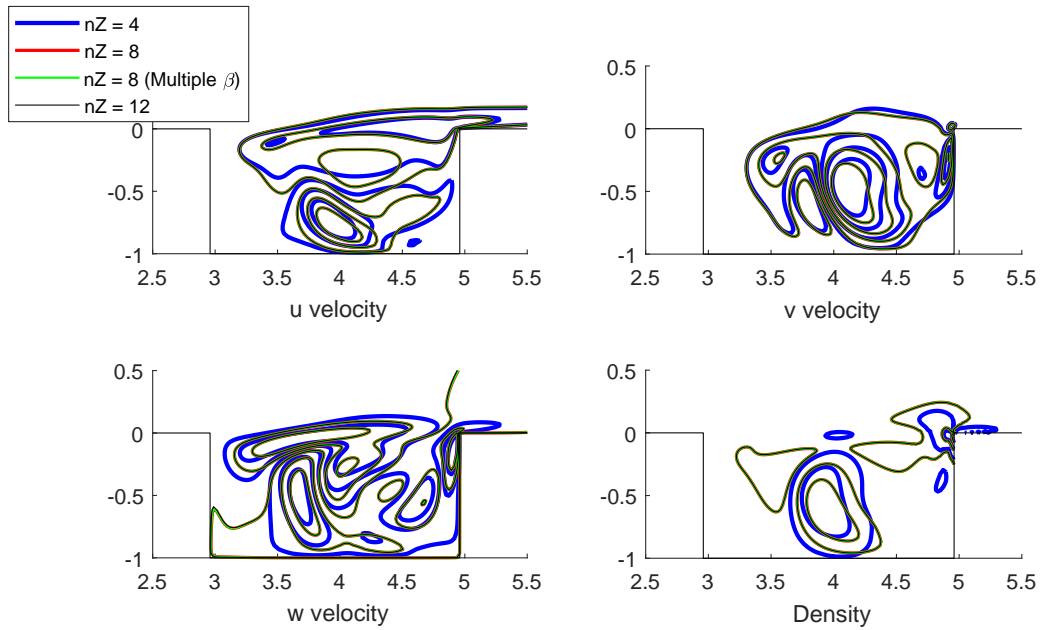


Figure 46 – Eigenfunction of mode 1 for mesh convergence analysis in 3D.

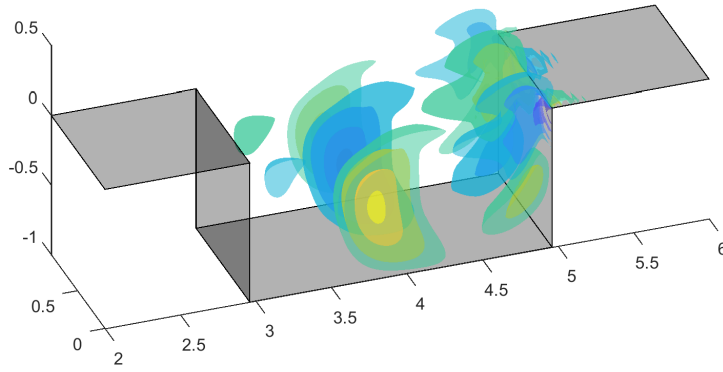


Figure 47 – Isosurfaces of density fluctuation of mode 1 at $\beta = 5.62$.

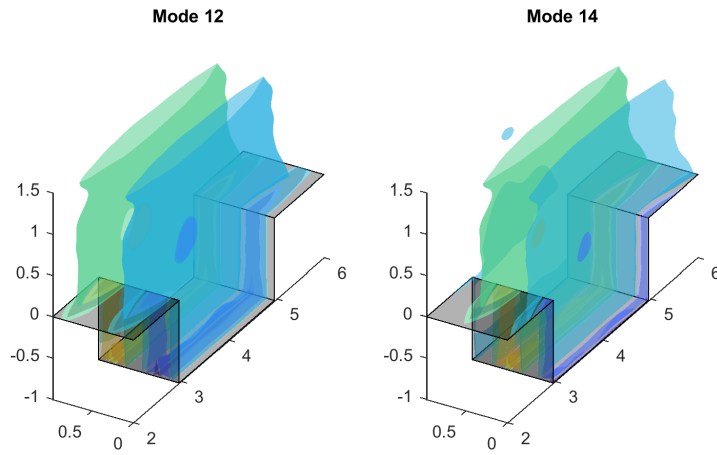


Figure 48 – Isosurfaces of density fluctuation of modes 12 and 14 at $\beta = 5.62$ when the phase in the span-wise direction is not fixed.

4.7 Arnoldi method convergence in three-dimensional analysis

When the domain was changed to three dimensions, a considerable increase in the number of variables happened. Apart from the extra variable for the span-wise velocity, the number of nodes was also increased. The spectral treatment for the span-wise direction was able to take the number of variables in the Arnoldi iteration back to what it was with two dimensions.

Figure 49 shows the evolution of the least stable eigenvalues as the method is iterated for the case with 8 span-wise nodes from the mesh convergence analysis with the spectral treatment.

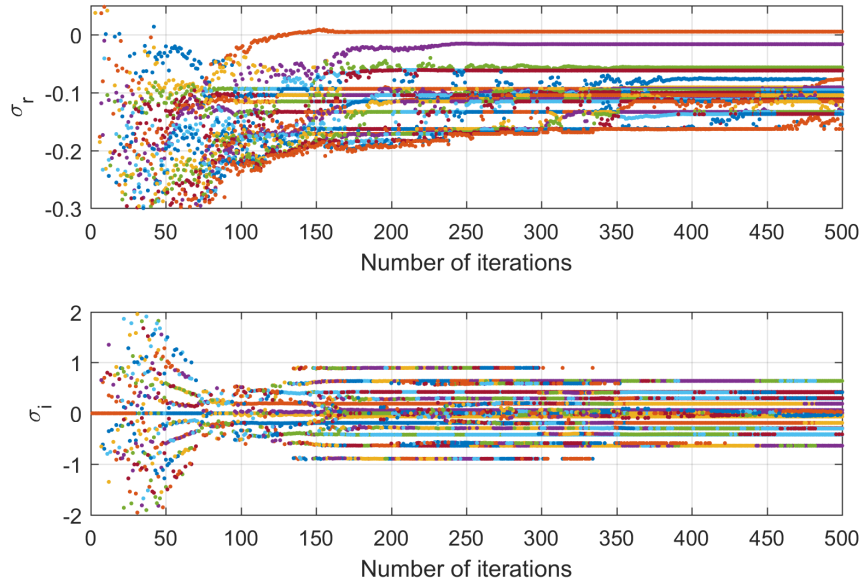


Figure 49 – Evolution of eigenvalues as the Arnoldi method is iterated for the 3D case.

Figure 50 brings this same data, but without the spectral treatment. Notice that, besides the slightly slower convergence, some modes start collapsing to the same value after a number of iterations, as was observed with modes 12 and 14 in Tab. 7. This happens when two modes that only differ by the span-wise phase are found.

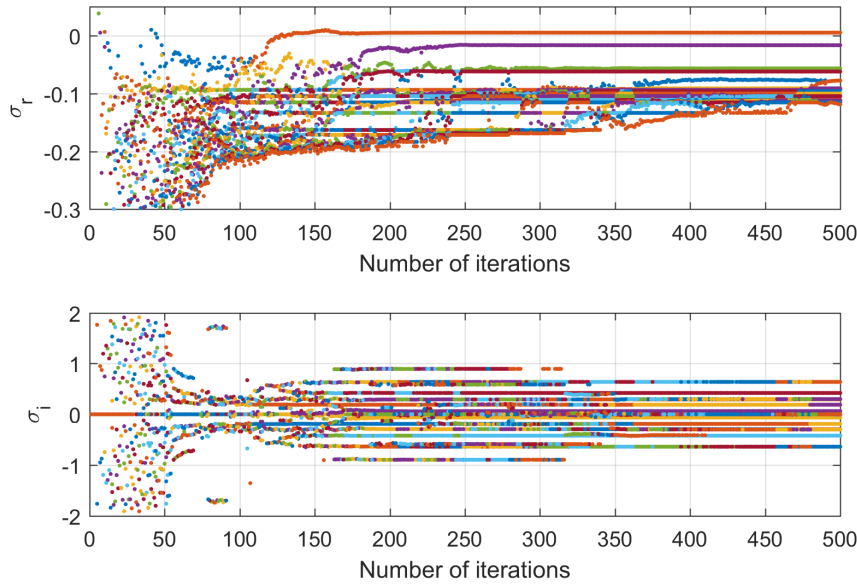


Figure 50 – Evolution of eigenvalues as the Arnoldi method is iterated for the 3D spectral case.

4.8 Comparison with the residual algorithm

The residual algorithm (RA) was used to make sure the eigenvalues and eigenfunctions found by the Arnoldi iterations matched the ones present in the code. As mentioned earlier, this algorithm is only capable of retrieving the least stable mode.

Mesh 2 from Tab. 3 was used for the comparison in two dimensions. The time series from the uniform initial condition towards the converged base flow was used as input for the residual algorithm.

35 probes were placed in the domain, both inside and outside the cavity. They stored the value of each variable every 1000 time steps. Data from time steps 1 to 2×10^6 was used. The initial condition for this run was a uniform flow outside the cavity.

Figure 51 shows the results obtained by the well-placed probes for each time sample, as well as the mean value and standard deviation.

This algorithm has computed the eigenvalue to be $\sigma = -0.0179$. Adding and subtracting one standard deviation, it is somewhere between -0.0178 and -0.0180. This matches the Arnoldi method, which has computed this value to be $\sigma = -0.01781$. These values were extracted from samples 1000 to 1200, just before the numerical noise started growing.

Figure 52 compares the eigenfunctions found by the Arnoldi method and by the residual algorithm. Two samples of the RA's eigenfunction are plotted, extracted from

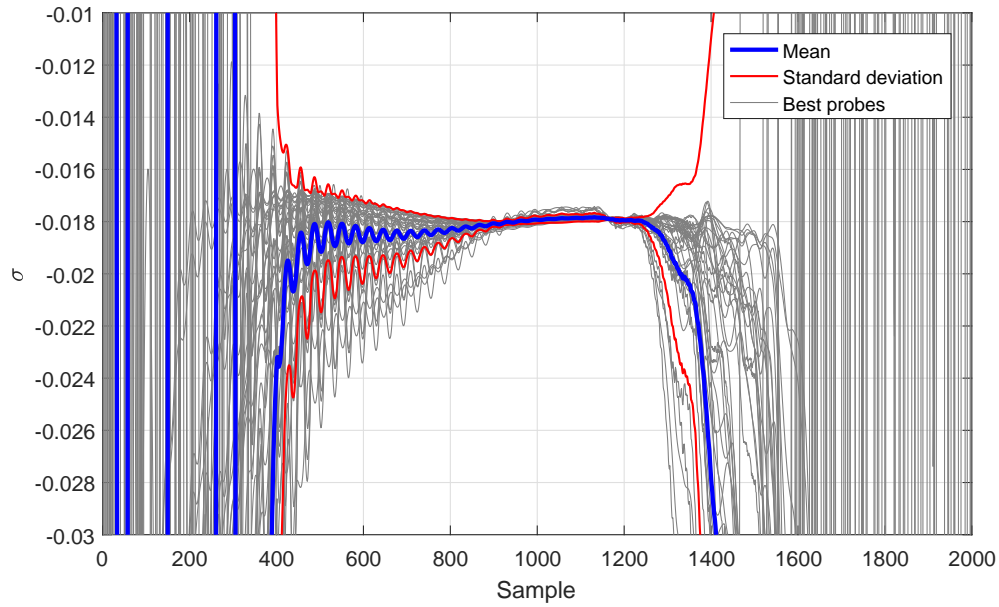


Figure 51 – Least stable eigenvalue as computed by the residual algorithm.

distinct time steps. The probes positions are also shown.

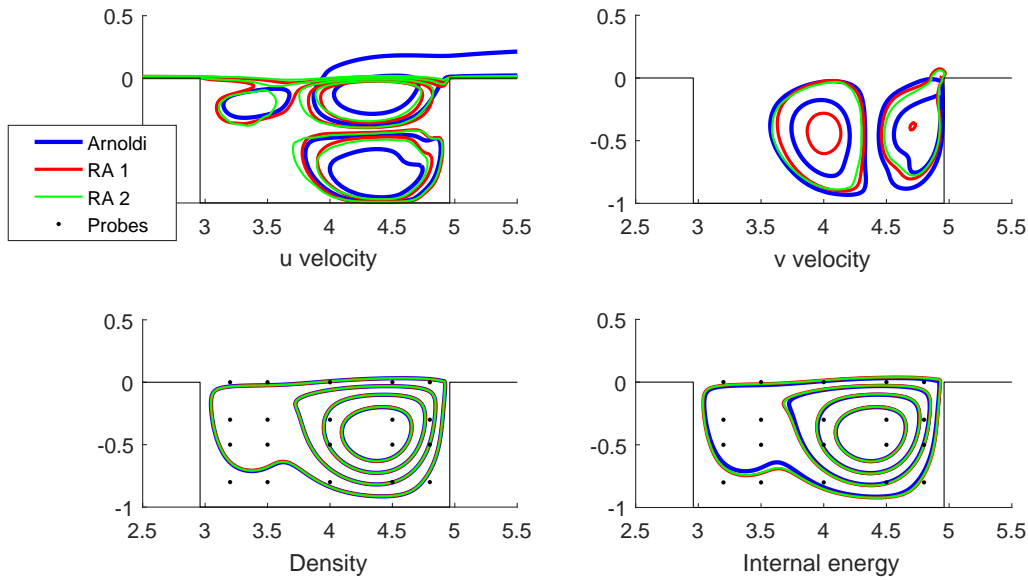


Figure 52 – The first eigenfunction as computed by the residual algorithm.

The eigenfunction matches for the density and the internal energy. For both velocities, the RA has not converged to a single eigenfunction as both samples yielded distinct results, especially just outside of the cavity. All 40 probes used were monitoring both the density and the internal energy inside the cavity. The probes outside the cavity or monitoring the velocities did not produce consistent results.

The three-dimensional case was also checked with the residual algorithm. A smaller value of $\beta = 0.504$ was used so only stable modes would be present. Instead of creating a time series from the uniform initial condition to the final flow, as was done in the two-dimensional case, a small Gaussian disturbance was added to a previously converged flow, this has considerably reduced the number of time steps needed to obtain the results.

Figure 53 shows the results obtained by the well-placed probes for each time sample, and the mean value plus and minus a standard deviation.

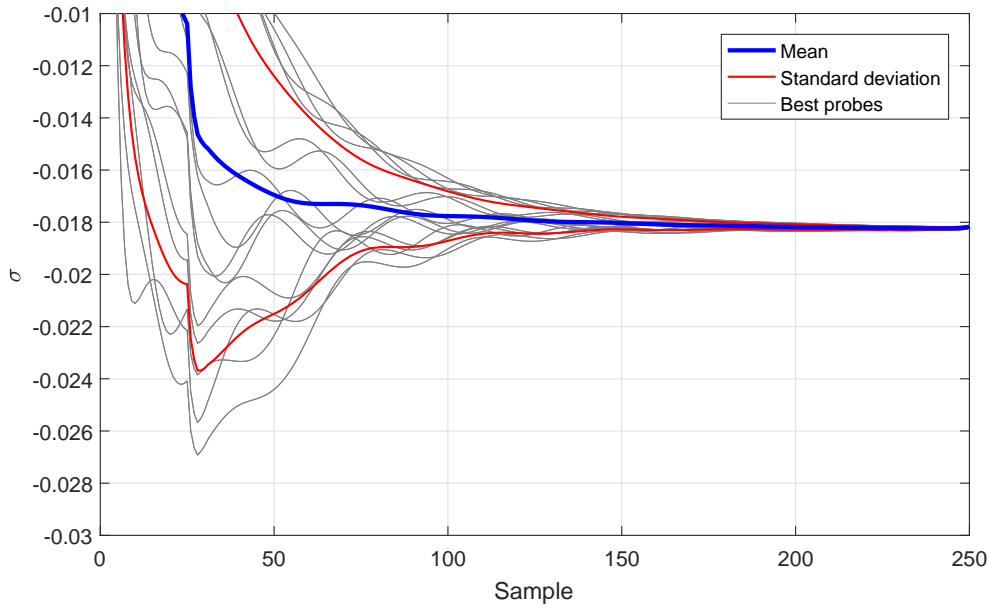


Figure 53 – Least stable eigenvalue as computed by the residual algorithm for the 3D case.

Averaging the computed σ value from samples 200 to 250, the RA has resulted in $\sigma = -0.0182 \pm 0.001$, while the Arnoldi method has retrieved $\sigma = -0.01813$.

Figure 54 compares the eigenfunctions found by the Arnoldi method and by the residual algorithm. Two samples of the RA's eigenfunction are plotted, extracted from distinct time steps.

Once more, both methods match for density and internal energy and there is a visible difference for the velocities.

Figures 55 to 58 compare the isosurfaces of mode 1 for both algorithms.

In terms of computational cost, the residual algorithm took just over a million iterations to converge to a solution in the two-dimensional case, which started with an uniform flow. The three-dimensional case, which was given a head start by having the base flow plus a small disturbance as initial solution, took about 250 thousand iterations. As shown in Fig 44 the Arnoldi iteration is capable of converging to the four decimal places given by the RA in about 250 thousand iterations.

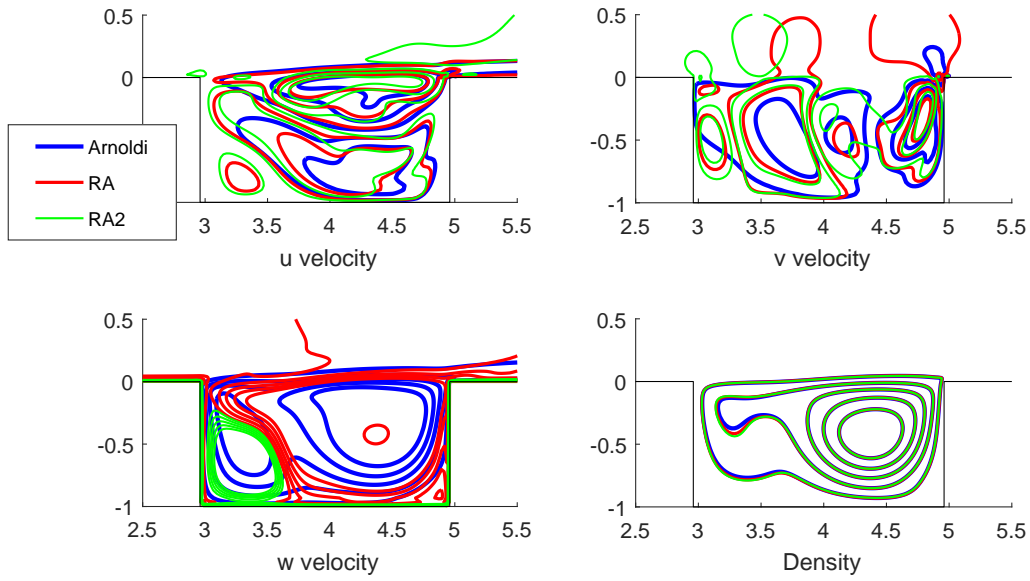


Figure 54 – The first eigenfunction as computed by the residual algorithm.

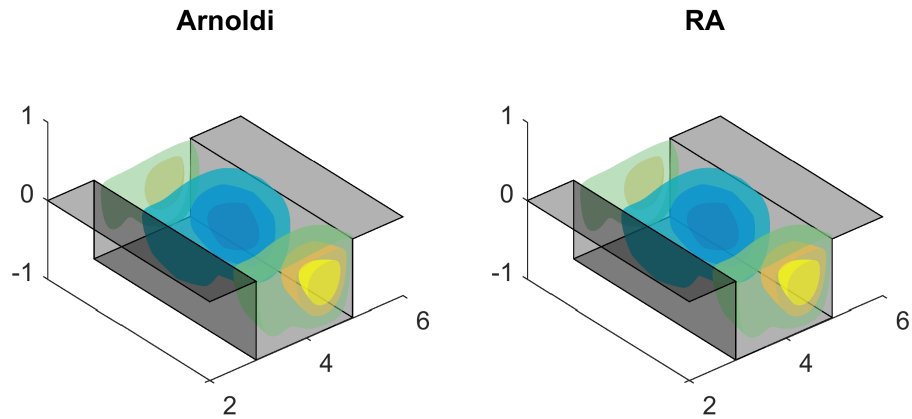


Figure 55 – Isosurfaces of density of mode 1, comparing the Arnoldi method to the Residual Algorithm

Therefore, both methods are roughly on par when retrieving the first eigenmode. But the Arnoldi method has the advantage of retrieving many more modes.

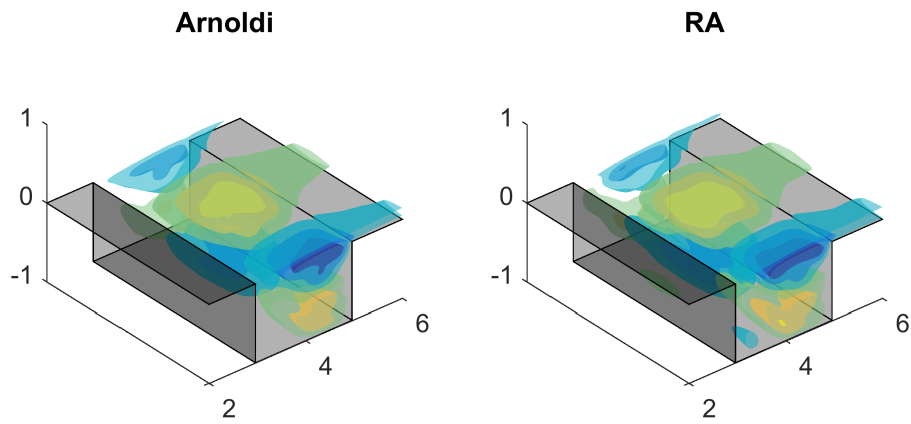


Figure 56 – Isosurfaces of stream-wise velocity of mode 1, comparing the Arnoldi method to the Residual Algorithm

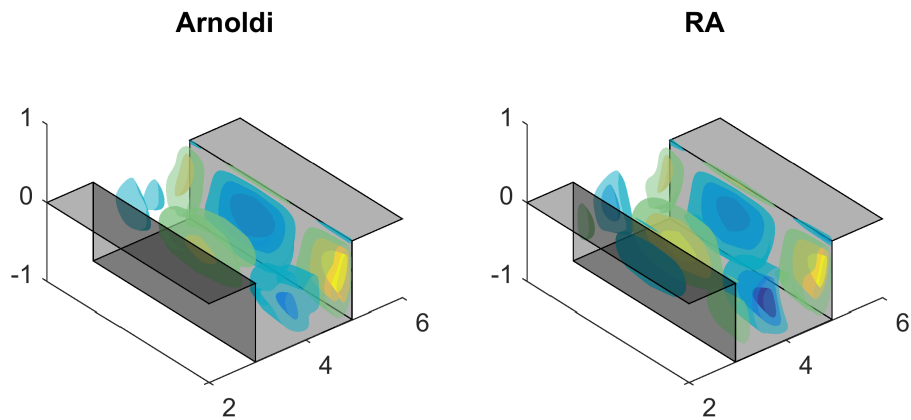


Figure 57 – Isosurfaces of wall-normal velocity of mode 1, comparing the Arnoldi method to the Residual Algorithm

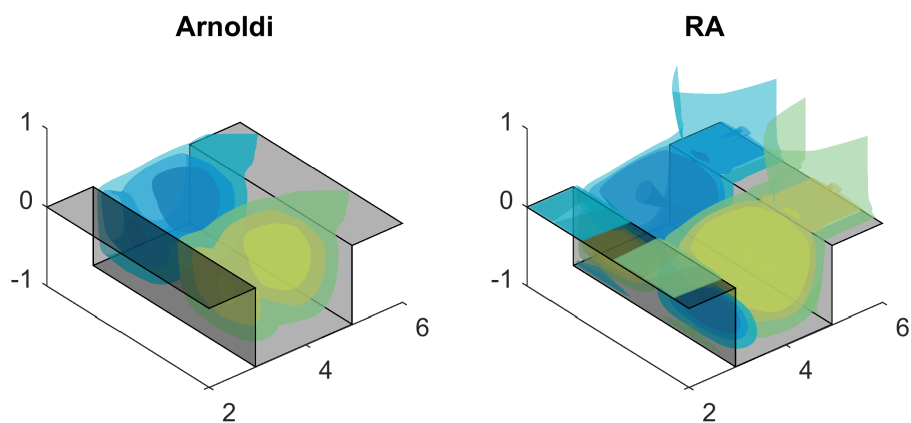


Figure 58 – Isosurfaces of span-wise velocity of mode 1, comparing the Arnoldi method to the Residual Algorithm

4.9 Two-dimensional lid-driven cavity

For further validation, the algorithm was also used to compute the modes of the lid-driven cavity used for the DNS validation. It is square and the Reynolds number is set to 1000, normalized by the edge length. The eigenvalues found are presented in Fig. 59. The values for the least stable modes are shown in Tab 8.

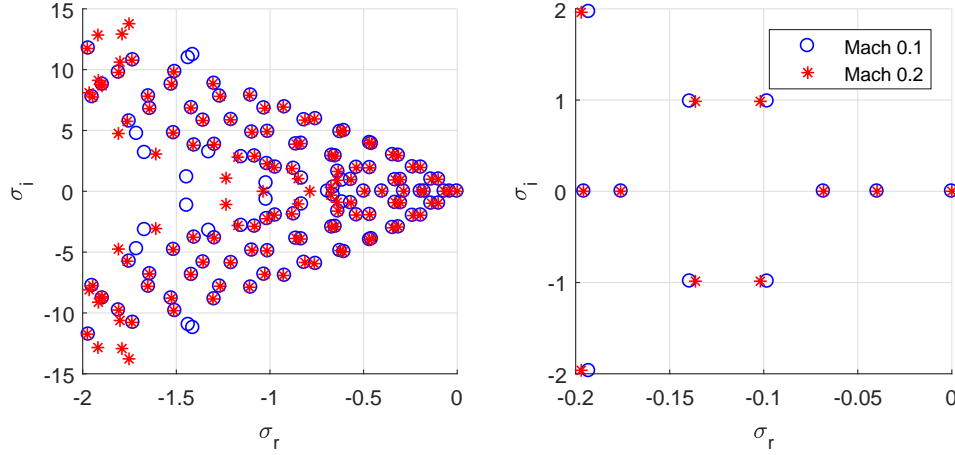


Figure 59 – Eigenvalues computed for the square lid-driven cavity at $Re = 1000$ and $Ma = 0.1, 0.2$.

Table 8 – Eigenvalues computed for the square lid-driven cavity.

| Mode | Ma = 0.1 | Ma = 0.2 |
|------|-------------------|-------------------|
| 1 | -0.0000 + 0.0000i | -0.0000 + 0.0000i |
| 2 | -0.0396 + 0.0000i | -0.0397 + 0.0000i |
| 3 | -0.0681 + 0.0000i | -0.0682 + 0.0000i |
| 4 | -0.0981 + 0.9874i | -0.1018 + 0.9855i |
| 5 | -0.0981 - 0.9874i | -0.1018 - 0.9855i |
| 6 | -0.1393 + 0.9860i | -0.1363 + 0.9856i |
| 7 | -0.1393 - 0.9860i | -0.1363 - 0.9856i |
| 8 | -0.1757 + 0.0000i | -0.1761 + 0.0000i |
| 9 | -0.1930 + 1.9682i | -0.1959 + 0.0000i |
| 10 | -0.1930 - 1.9682i | -0.1970 + 1.9622i |

Note that the first mode has a null eigenvalue, which means it is neutral. This mode is only possible because the DNS does not explicitly force a constant mass inside the cavity. It represents mass getting in or out of the cavity.

The residual algorithm was also ran for this case. Fig 60 shows the most unstable modes as the baseflow was generated. Each color corresponds to a different variable recorded by the probes. The thick lines indicate the average of each variable. The dashed lines are the modes computed by the Arnoldi iteration.

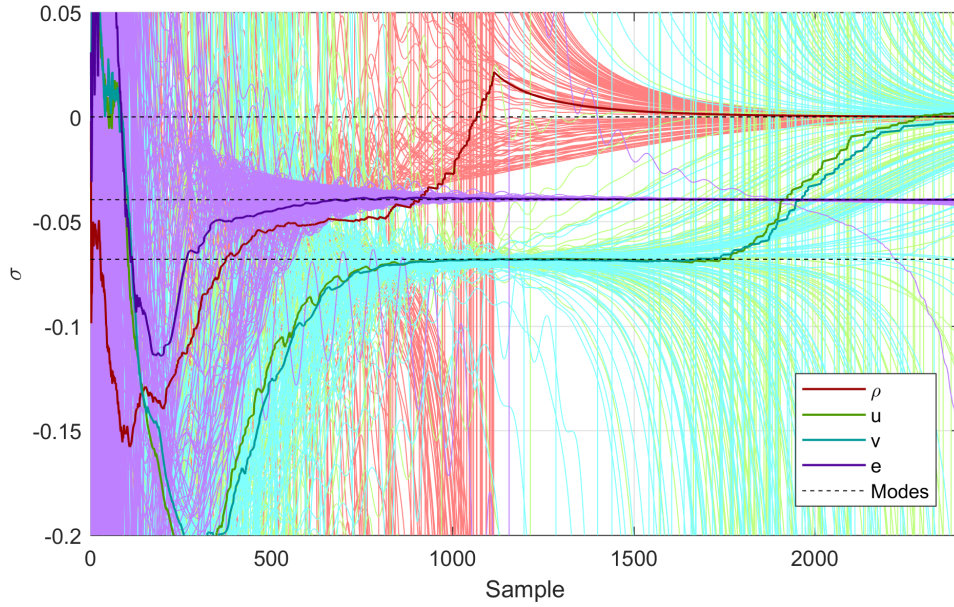


Figure 60 – Evolution of the modes computed by the residual algorithm.

It is interesting to note how the variables converge to different modes. The density probes have only agreed to a single value at the neutral mode. The internal energy probes are very well converged to the second mode. Both velocities have converged to the third mode before its magnitude became too small when compared to the computer rounding error.

Merle, Alizard and Robinet (2010) has used a matrix-forming method for an incompressible square lid-driven cavity at this same Reynolds number and computed the least stable eigenvalue at $\sigma = -0.06807$. Which is consistent to the third mode found by both the Arnoldi iteration and the residual algorithm.

The first mode retrieved by the Arnoldi iteration, at $Ma = 0.1$, is depicted in Fig. 61. Note how the density fluctuation is negative across whole the domain, meaning that this mode represents mass flowing into the domain or out of it. This is due to the weak boundary conditions used, which do not impose a constant mass inside the cavity. During the simulation, the total mass has decreased by 4.1×10^{-5} from its unitary initial condition.

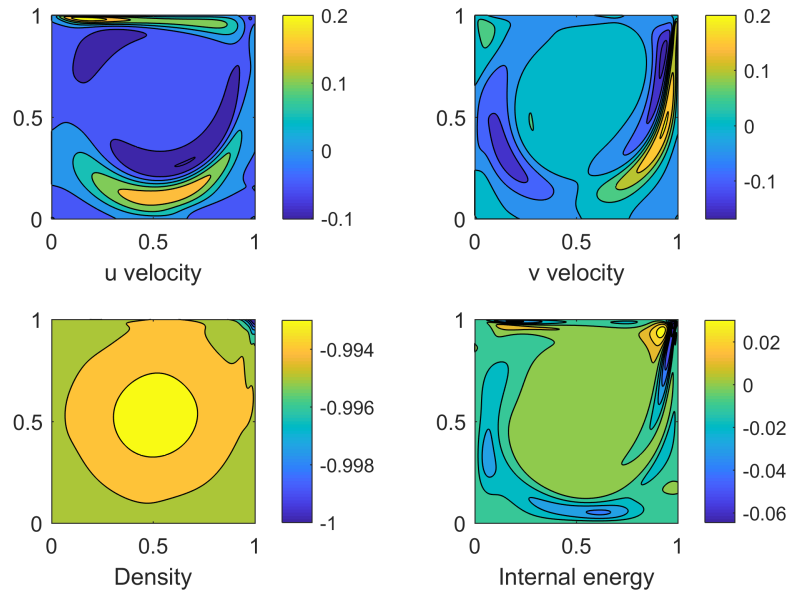


Figure 61 – The first eigenfunction of the lid-driven cavity.

The second most unstable mode is shown in Fig. 62. It can be seen that the fluctuation of internal energy in this mode is about 3 orders of magnitude larger than the fluctuation of the other variables. This explains why the residual algorithm could only retrieve this mode with the internal energy probes and not the others.

This also explains why the incompressible analysis by Merle, Alizard and Robinet (2010) has not found this mode. Physically, this mode corresponds to the temperature diffusion inside the cavity, a phenomenon that is not accounted for in the incompressible equations.

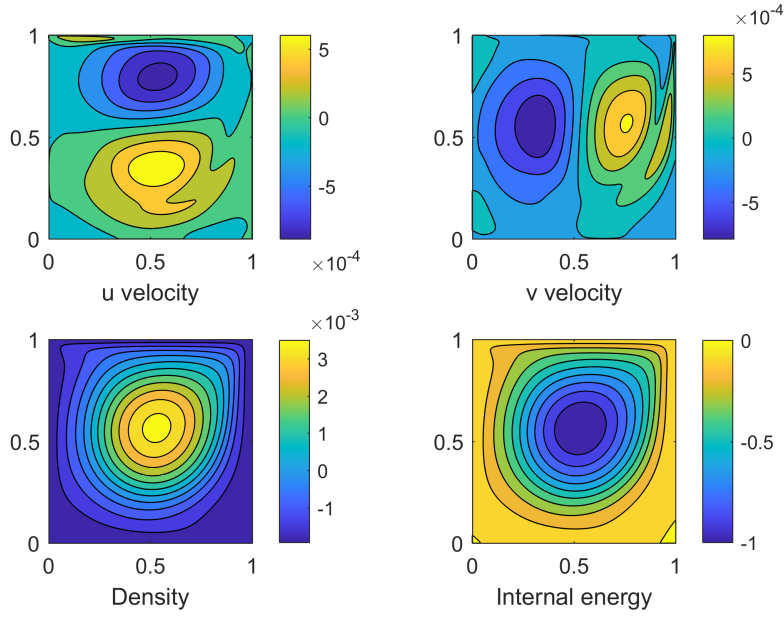


Figure 62 – The second eigenfunction of the lid-driven cavity.

The third most unstable mode is illustrated in Fig. 63. Note how the velocities present the greatest fluctuation magnitudes.

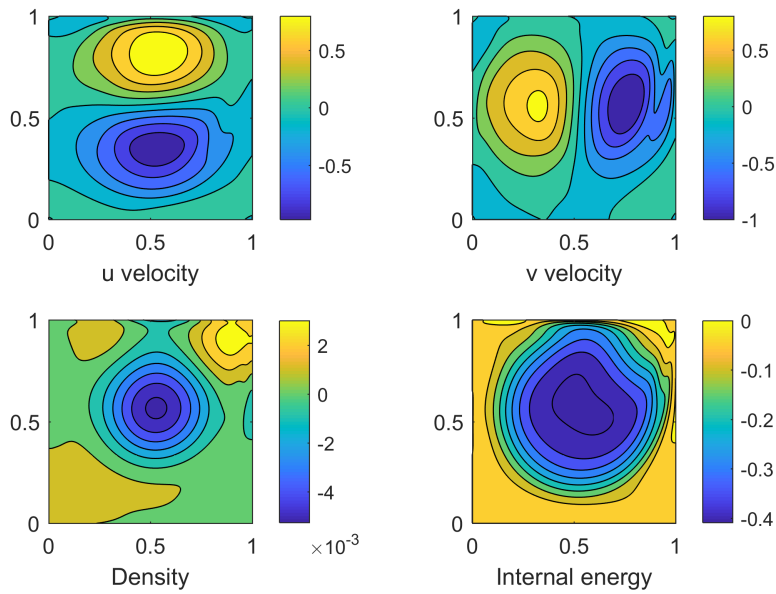


Figure 63 – The third eigenfunction of the lid-driven cavity.

By integrating the density fluctuation on the domain for modes 2 and 3, it can be seen that the net mass change can be considered null as it is about 6 orders of magnitude smaller than the greatest fluctuations.

To check the hypothesis that the first two modes found are caused by the compress-

ibility effects, a closed cavity with a static lid was run in the algorithm. As expected, both the first and the second modes were also present in this case, but not the third. Which confirms the hypothesis, explaining why the incompressible analysis has not retrieved the first two modes found in the compressible case.

The first mode has a null eigenvalue. The eigenfunction is roughly constant for the density and almost null for the other three variables. It can be seen in Fig. 64. The noise is about seven orders of magnitude smaller than the computed density eigenfunction.

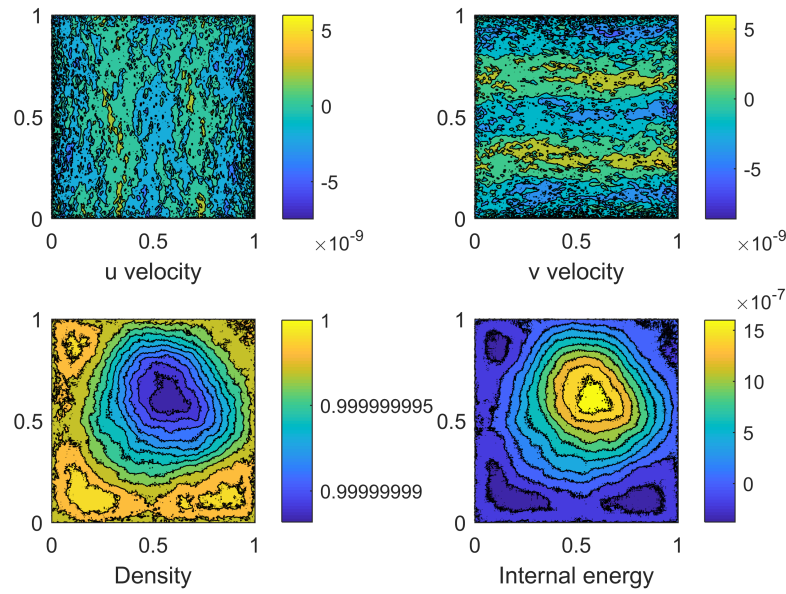


Figure 64 – The first eigenfunction of the static cavity.

The second eigenvalue has shifted from $\sigma = -0.0396$ in the moving lid case to $\sigma = -0.0341$ in the static case. Its eigenfunction is shown in Fig. 65.

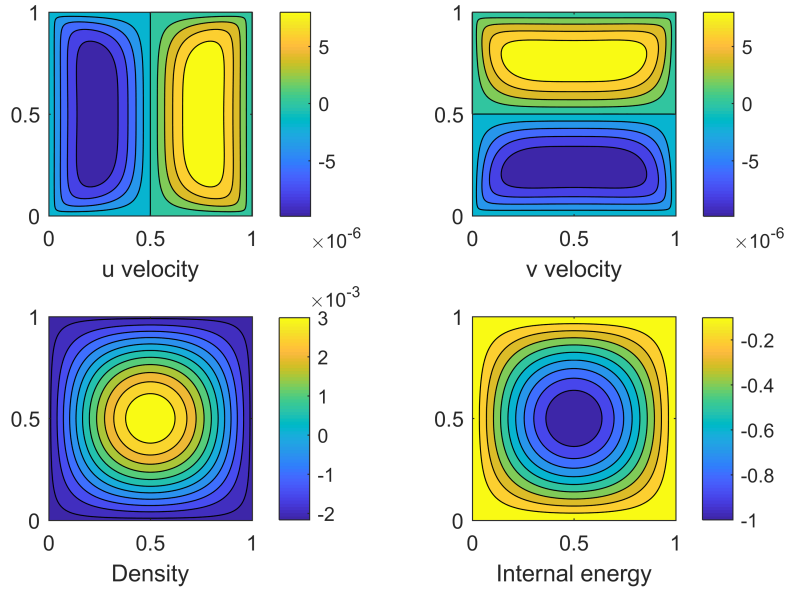


Figure 65 – The second eigenfunction of the static cavity.

4.10 Three-dimensional lid-driven cavity

A case from Bergamo (2014) was used to validate span-wise periodical results in a compressible lid-driven cavity.

The parameters for this case are: cavity aspect ratio, $L/D = 1$; Reynolds number, $Re = 900$; Mach number, $Ma = 0.1$; span-wise wavenumber, $\beta = 7.35$.

A mesh with 120×120 nodes is used. The Arnoldi method was run for 500 iterations, each being run for 500 DNS time steps. In the span-wise direction, 4, 8 and 12 nodes were used.

Figure 66 compares the results from these meshes to the eigenvalues available in the reference. The coarsest mesh was not able to reproduce any of the modes. Both other meshes have accurately retrieved all eigenvalues available. Table 9 compares the modes found in the reference to the ones retrieved.

Table 9 – Eigenvalues computed for the three dimensional square lid-driven cavity at $Re = 900$, $Ma = 0.1$ and $\beta = 7.35$.

| Reference | $nz = 8$ | $nz = 12$ |
|-----------------------|-------------------------|-------------------------|
| $-0.0035 \pm 0.4925i$ | $-0.00348 \pm 0.49340i$ | $-0.00349 \pm 0.49350i$ |
| $-0.1058 \pm 0.6855i$ | $-0.10571 \pm 0.68696i$ | $-0.10566 \pm 0.68672i$ |
| $-0.1061 \pm 1.3691i$ | $-0.10650 \pm 1.37161i$ | $-0.10648 \pm 1.37138i$ |
| -0.1405 | -0.14072 | -0.14046 |

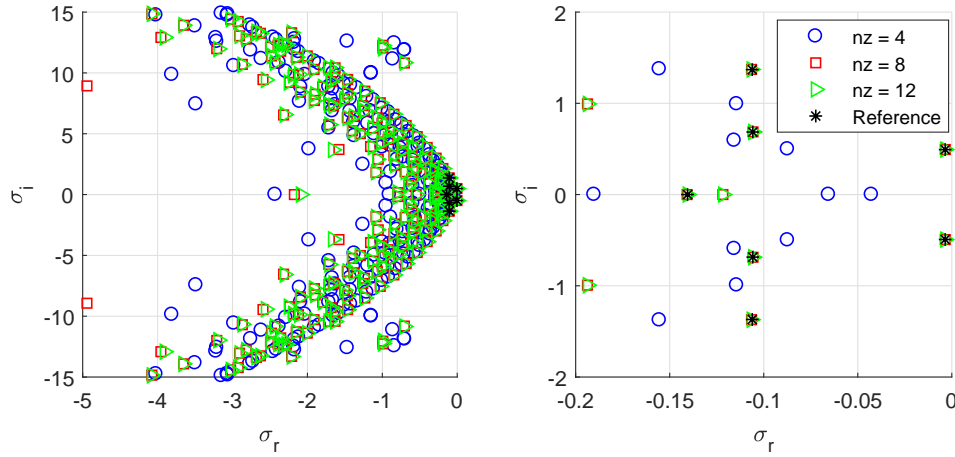


Figure 66 – Eigenvalues computed for the three dimensional square lid-driven cavity at $Re = 900$, $Ma = 0.1$ and $\beta = 7.35$.

4.11 Comparison to the literature for open cavities

Finally, the method was checked against the literature on two and three-dimensional open cavities.

Vicente et al. (2014) provide the most unstable eigenvalue for the $\beta = 5.62$ case at $Re_D = 1149$, $\theta_0 = 0.0337$ and $Ma = 0$. Figure 67 compares this value to the ones obtained by the present method. The reference eigenvalue is $\sigma_{ref} = 0.00011 \pm 0.17208i$, while the first eigenvalue computed by the method ($nz = 12$, $Ma = 0.1$) was $\sigma_1 = 0.00521 \pm 0.1886i$. The amplification rates differ in the third decimal digit, while the frequencies differ in the second decimal digit. It is worth noting that while the values may look off relative to each other, they must be compared to the typical value of eigenvalues present, which is in the first decimal order for the instability modulus and in the units order for the frequencies.

A second case was used for validation, it was run by both Brès and Colonius (2008) and Sun et al. (2016). Reynolds number is $Re_D = 1500$, incoming boundary layer thickness is $\theta_0 = 0.0379$, the cavity aspect ratio is $L/D = 2$. Brès has run this case at Mach number $Ma = 0.325$, while Sun has used $Ma = 0.3$. The later value was used in this work. The span-wise wave number was set to $\beta = \pi$, 2π and 4π . This time, the walls are considered adiabatic instead of isothermal. Figure 68 shows the results obtained.

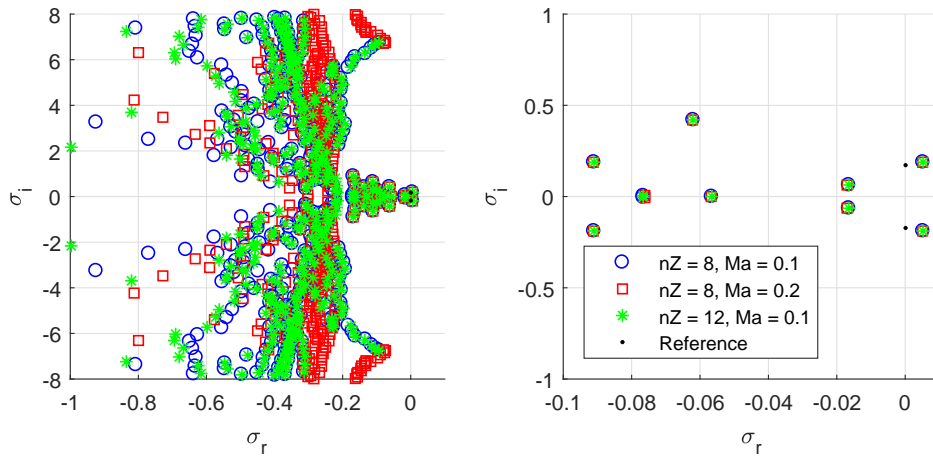


Figure 67 – Eigenvalues computed for the $\beta = 5.62$ case and compared to the reference.

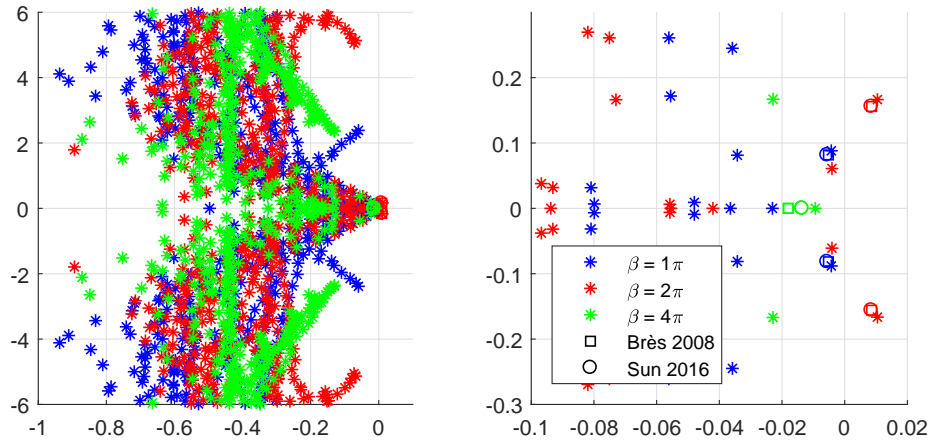


Figure 68 – Eigenvalues computed for the $\beta = 1, 2$ and 4 cases and compared to the references.

4.12 Code performance

For the code performance analysis, a sample case was created. Its mesh has a total of 380 nodes in the stream-wise direction, 170 nodes in the wall-normal direction and 10 nodes in the span-wise direction, including both the physical domain and the buffer zones.

The 4th order compact spectral-like finite differences were used for the spatial derivatives. The 4th order Runge-Kutta method was used for time integration. Numerical filtering was turned on for all directions at every step. Selective Frequency Damping was turned on only at the buffer zones.

A server running the Ubuntu¹ 14.04 operating system was used. It features 4 Intel®

¹ <<https://www.ubuntu.com/>>

Xeon® E7-4820 v3 processors, each with 10 cores at 1.90 GHz. A total of 128 GB of DDR3 RAM is available.

The Intel® FORTRAN Compiler² is used in all cases.

4.12.1 Flow simulation

For the two-dimensional performance analysis, the code was run for 1000 time steps. About 60 MB of RAM were used for the simulation. Table 10 brings the results for different types of parallel execution.

In the three-dimensional case, the code was run for 100 steps, using about 600 MB of RAM. The results are in Tab. 11.

Table 10 – Computation time for the two-dimensional case.

| Domain slices | OpenMP workers | Total threads | Runtime (s) | Time per node per step (s) | Speed up | Efficiency |
|---------------|----------------|---------------|-------------|----------------------------|----------|------------|
| 1 | 1 | 1 | 288.9 | 4.47e-6 | - | - |
| 2 | 1 | 2 | 144.9 | 2.24e-6 | 99% | 99% |
| 1 | 4 | 4 | 122.4 | 1.89e-6 | 136% | 59% |
| 2 | 4 | 8 | 67.5 | 1.05e-6 | 328% | 53% |

Table 11 – Computation time for the three-dimensional case.

| Domain slices | OpenMP workers | Total threads | Runtime (s) | Time per node per step (s) | Speed up | Efficiency |
|---------------|----------------|---------------|-------------|----------------------------|----------|------------|
| 1 | 1 | 1 | 622.7 | 9.64e-6 | - | - |
| 2 | 1 | 2 | 328.2 | 5.08e-6 | 89% | 95% |
| 4 | 1 | 4 | 169.6 | 2.63e-6 | 267% | 92% |
| 8 | 1 | 8 | 93.8 | 1.45e-6 | 564% | 83% |

It can be noted that the parallel execution by slicing the domain and using MPI is much more efficient than simply increasing the number of OpenMP workers.

4.12.2 Instability analysis

During the instability analysis, the vast majority of the computational time is spent by the DNS.

The main concern of this routine is memory usage as it must store multiple states of the domain at once in the ζ matrix of Fig. 17.

² <<https://software.intel.com/en-us/fortran-compilers>>

This matrix has each value stored as a double, which takes 8 bytes of memory. Therefore, its size is given by the amount of nodes in the domain times the number of variables times the number of Arnoldi iterations times 8 bytes.

In this $380 \times 170 \times 10$ domain, for example, this matrix would take 2.6 GB of RAM if 1000 Arnoldi iterations are performed.

Chapter 5

Results

In this chapter, three different parameter sweeps are performed. First, various Mach numbers are run for two different incoming boundary layer thicknesses. One with a thicker layer, which is the same case used in the validation chapter. And one with a thinner layer.

Later, for a fixed Mach number of 0.5, many different incoming boundary layer thicknesses are tried.

Finally, the results observed are related to the physical phenomena that may cause them. Three types of phenomena are checked for their influence:

1. Resonance with standing waves
2. Spatial amplification at the mixing layer
3. Energy transfer from flow disturbances to acoustic modes

At the end, the linear stability results are compared to DNS runs, which include non-linear effects.

Figure 69 illustrates the three sweeps performed.

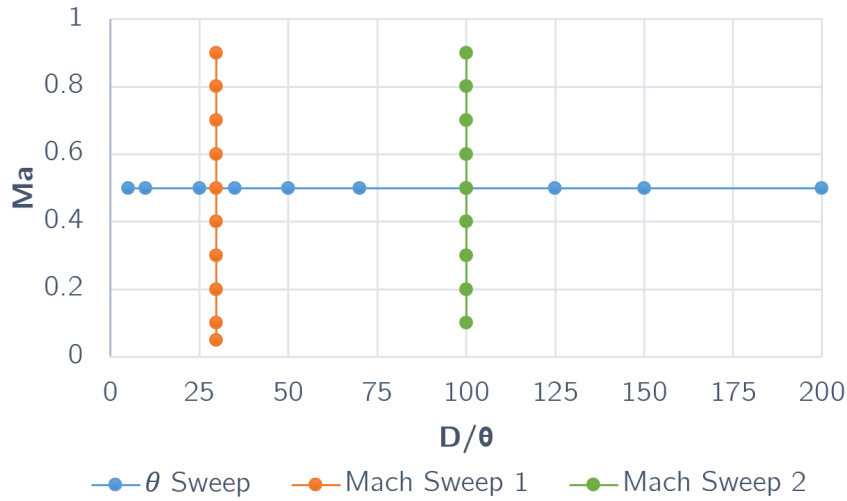


Figure 69 – Parametric space investigated.

5.1 Influence of Mach number

The incompressible case from Vicente et al. (2014), used for validation at $Ma = 0.1$, was extended to a range of subsonic Mach numbers. The cavity's aspect ratio is $L/D = 2$, the Reynolds number is $Re_D = 1149$ and the boundary layer thickness at the cavity's leading edge is $\theta = 0.0337$.

There is little change in the baseflow velocity field in the observed range of Mach numbers, from 0.05 to 0.9.

Figure 70 shows the eigenvalues found for this case as the Mach number increases. Most modes remain mostly unchanged. The exception are Rossiter-like modes (see Figs. 74 and 75).

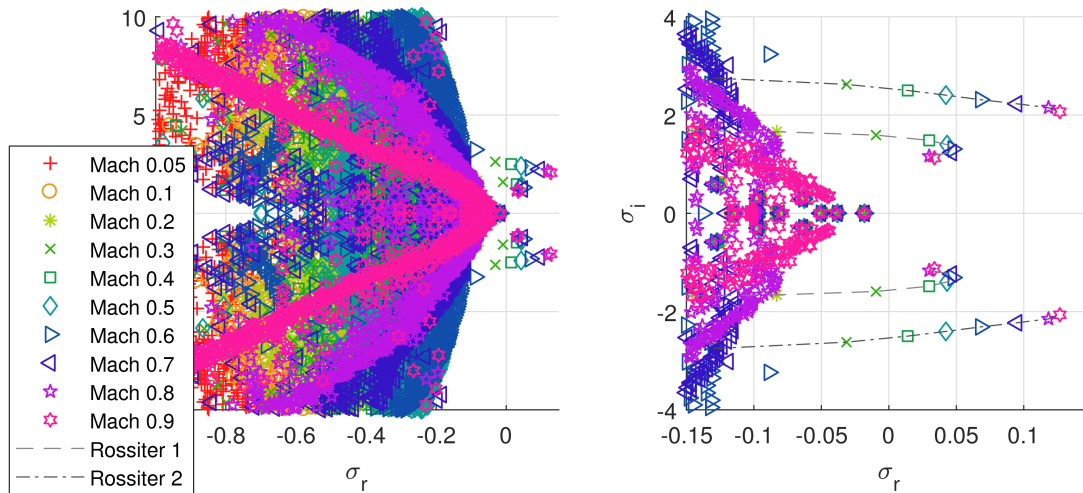


Figure 70 – Eigenvalues of the open cavity flow for various Mach numbers.

Figure 71 shows how the eigenvalues of both Rossiter branches change with the Mach number. By interpolating the available values, branch 1 becomes unstable above Mach 0.32 and branch 2, above Mach 0.36. Rossiter 2 becomes the most unstable just above Mach 0.5.

The instability of Rossiter mode 1 reaches a peak between Machs 0.6 and 0.7, becoming slightly more stable above these values.

The frequency reduces as the Mach number is increased. This is due to the reduced speed of sound when compared to the unitary free stream velocity. For example, at Mach 0.1, the feedback acoustic waves travel at a velocity of 10, while at Mach 0.5, this velocity is reduced to 2.

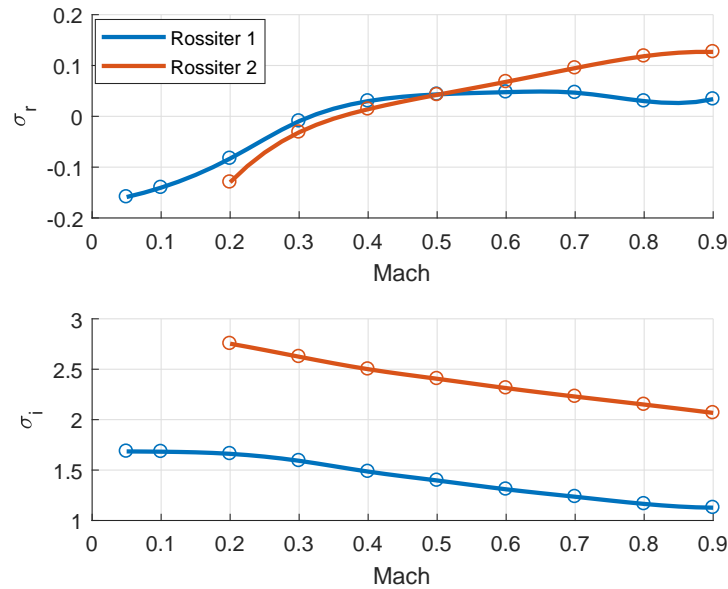


Figure 71 – Effect of Mach number on the eigenvalues of both Rossiter modes.

Figures 72 and 73 show both the real and the imaginary parts of the internal energy eigenfunction.

By plotting multiples phases of the pressure in the eigenfunctions, one can verify they resemble Rossiter modes. Figure 74 shows the first branch, corresponding to the first Rossiter mode and Fig. 75 shows branch 2, corresponding to the second mode.

In both figures, disturbances at the cavity entrance can be seen traveling from the leading edge to the trailing edge. As they interact with the trailing edge, a wave is generated inside the cavity, that travels back to the leading edge, causing a new disturbance at the shear layer.

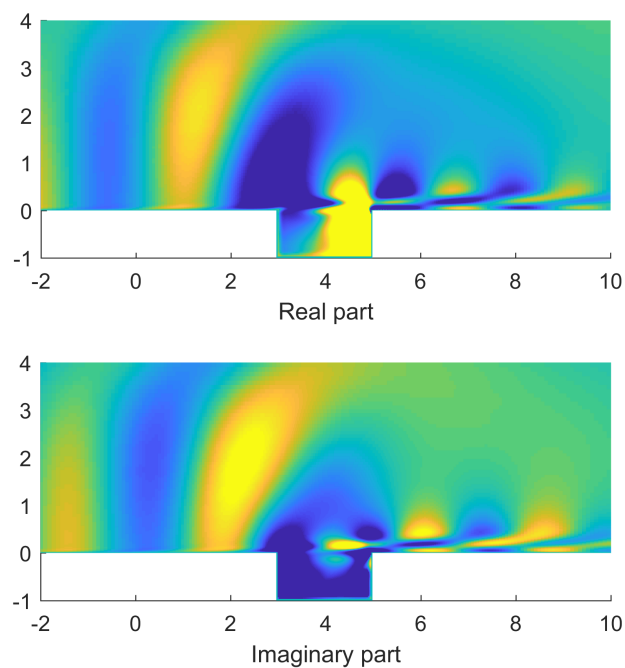


Figure 72 – Real and imaginary parts of internal energy eigenfunction of branch 1 at Mach 0.6.

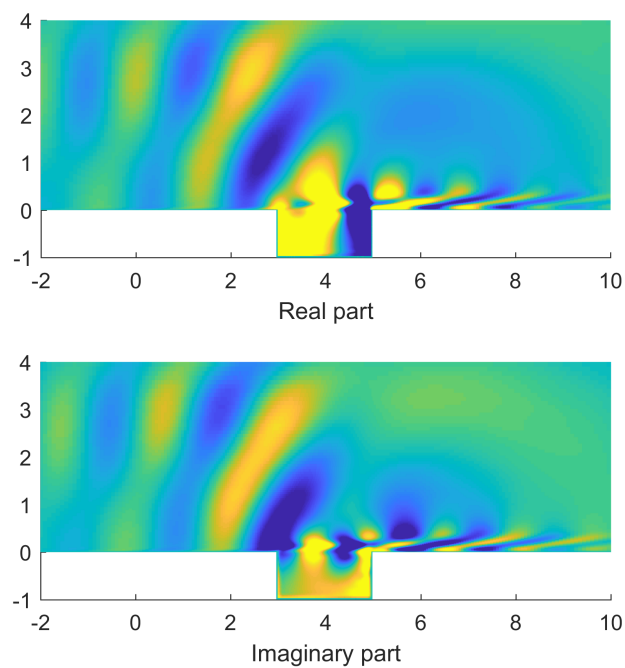


Figure 73 – Real and imaginary parts of internal energy eigenfunction of branch 2 at Mach 0.6.

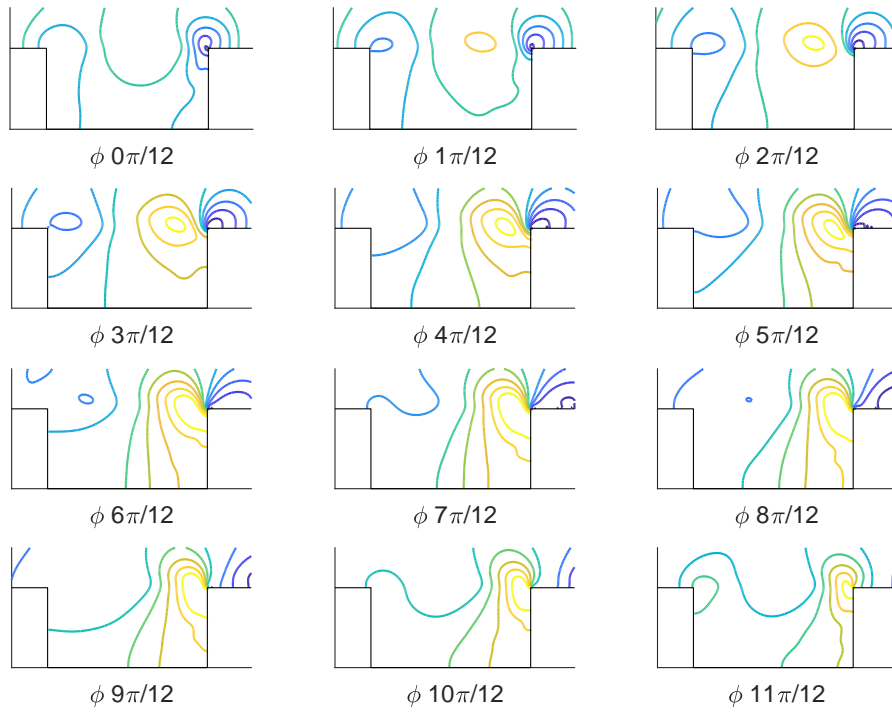


Figure 74 – Multiple phases of the pressure eigenfunction of Rossiter mode 1 at Mach 0.6

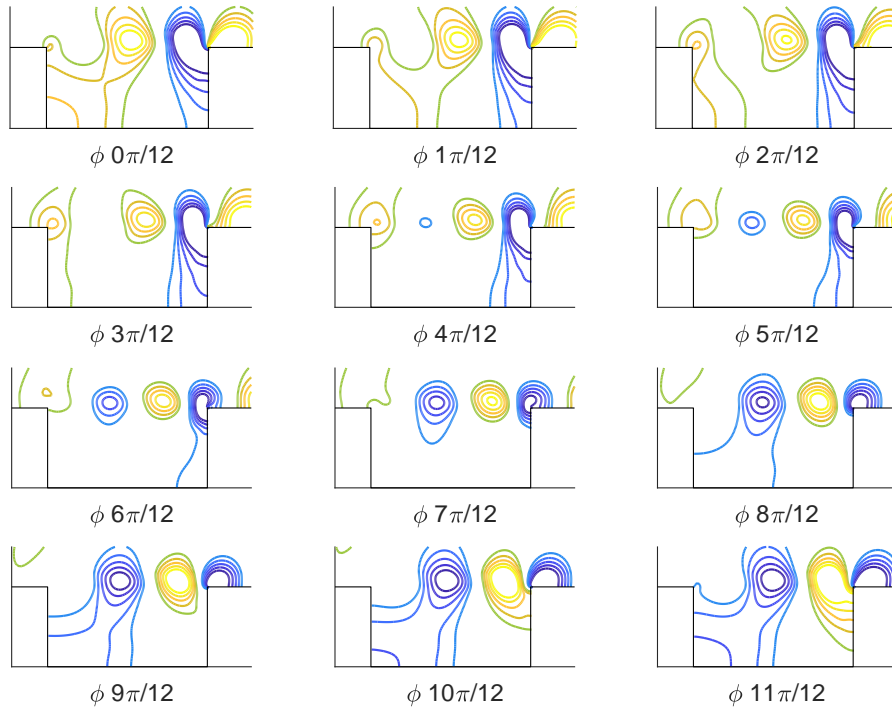


Figure 75 – Multiple phases of the pressure eigenfunction of Rossiter mode 2 at Mach 0.6

A second Mach number sweep was performed for a thinner incoming boundary layer. The following parameters were used: Cavity aspect ratio $L/D = 2$, Reynolds number $Re_D = 1000$, Incoming boundary layer thickness $\theta = 0.01$.

This time, up to four Rossiter modes were retrieved by the method, as shown in Fig. 76.

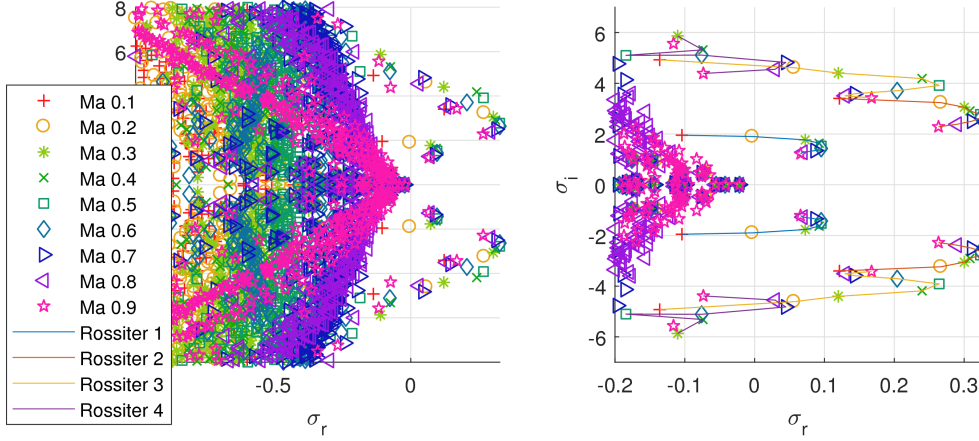


Figure 76 – Eigenvalues of the open cavity flow for various Mach numbers (thinner boundary layer).

Figure 77 shows that, in this case, Rossiter mode 2 is always the most unstable, reaching its peak instability around Mach 0.6. Rossiter mode 3 has a peak instability just below Mach 0.4. Mode 4 has two peaks, one just before Mach 0.4 and the other just above Mach 0.7. The oscillation frequency has a much more uniform behavior, usually reducing slightly as the Mach number increases.

One phenomenon that may cause this behavior is the frequency matching between different flow mechanisms. In this case, these peaks are suspected to happen when the Rossiter mode frequency matches the standing wave modes, predicted by Plumblee, Gibson and Lassiter (1962).

This would mean that in the case of Rossiter mode 4, the two peaks observed would match two different acoustic harmonics in the cavity, with a switching somewhere around Mach 0.5.

Figure 78 compares the modes predicted by Rossiter (1964) (Eq. 5.1) to the modes from Plumblee, Gibson and Lassiter (1962) (Eq. 5.2).

$$\omega = \frac{2\pi(N_R - \gamma)/L}{1/\kappa + Ma} \quad (5.1)$$

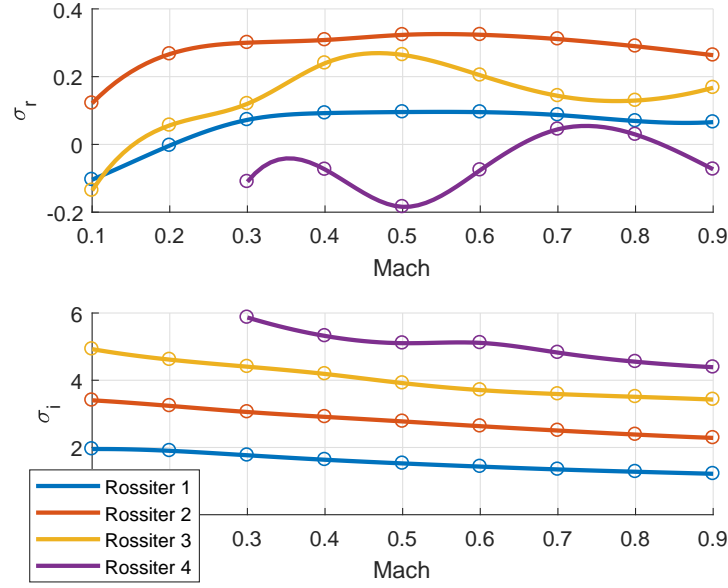


Figure 77 – Effect of Mach number on the eigenvalues of the Rossiter modes (thinner boundary layer).

N_R is the Rossiter mode number. $\gamma = 0.25$ and $\kappa = 1/1.75$ are empirical constants.

$$\omega = \frac{\pi}{2Ma} \left[\left(\frac{M_p}{L} \right)^2 + \left(\frac{N_p}{D} \right)^2 \right] \quad (5.2)$$

M_P is the number of standing waves in the stream-wise direction and N_P , in the wall-normal direction. The modes are identified by (M_P, N_P) . In the case of a cavity with aspect ratio $L/D = 2$, modes $(2,0)$ and $(0,1)$ coincide in frequency.

There is a considerable difference in the frequency from the Rossiter equation to the global analysis, especially at the first and second modes, this may be attributed to the fact the Rossiter empirical constants were extracted from a fully non-linear case, while the global analysis is linear.

Note how curves $P(2,0)$ and $P(1,1)$ cross curve $R4$ at around the first peak instability Machs observed in Fig. 77. $P(2,1)$ cross $R4$ at around its second peak instability. The same is valid for curves $P(2,0)$ and $P(1,1)$ and $R3$.

The eigenfunction phase of the pressure was plotted for each of the cases observed, as seen in Fig 79.

It can be seen that for Rossiter mode 4, a single acoustic node is present up to Mach 0.5, with a second node appearing above Mach 0.6. A similar phenomenon can be observed for Rossiter mode 3, around Mach 0.6.

It can be concluded that, while matching frequencies of Rossiter modes and standing

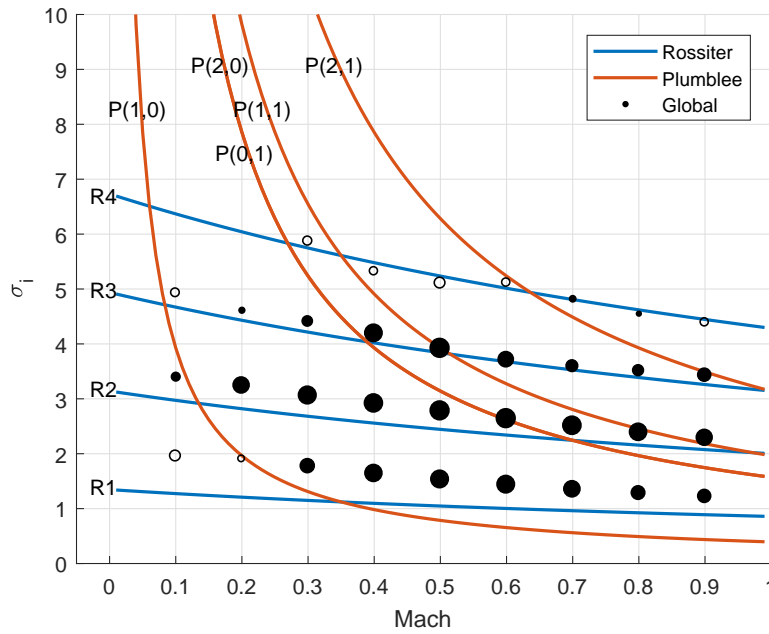


Figure 78 – Rossiter modes compared to standing wave modes and to the global modes. Filled markers indicate unstable modes, the size relate to the magnitude of the eigenvalue's real part.

wave mode do play a role in the global stability, other factors may be more important to the overall instability of the global modes. They are covered in the following sections.

Yamouni, Sipp and Jacquin (2013) has found this effect to be of greater magnitude in their parametric space, this was attributed to his relatively smaller mixing layer when compared to the cavity size, which causes cavity-related pressure oscillations to have a larger magnitude comparatively. This is also the reasoning behind the fact the standing waves have had a greater effect over larger Rossiter modes: the oscillations they cause in the mixing layer are smaller in magnitude, allowing the cavity pressure fluctuations to have a larger role overall.

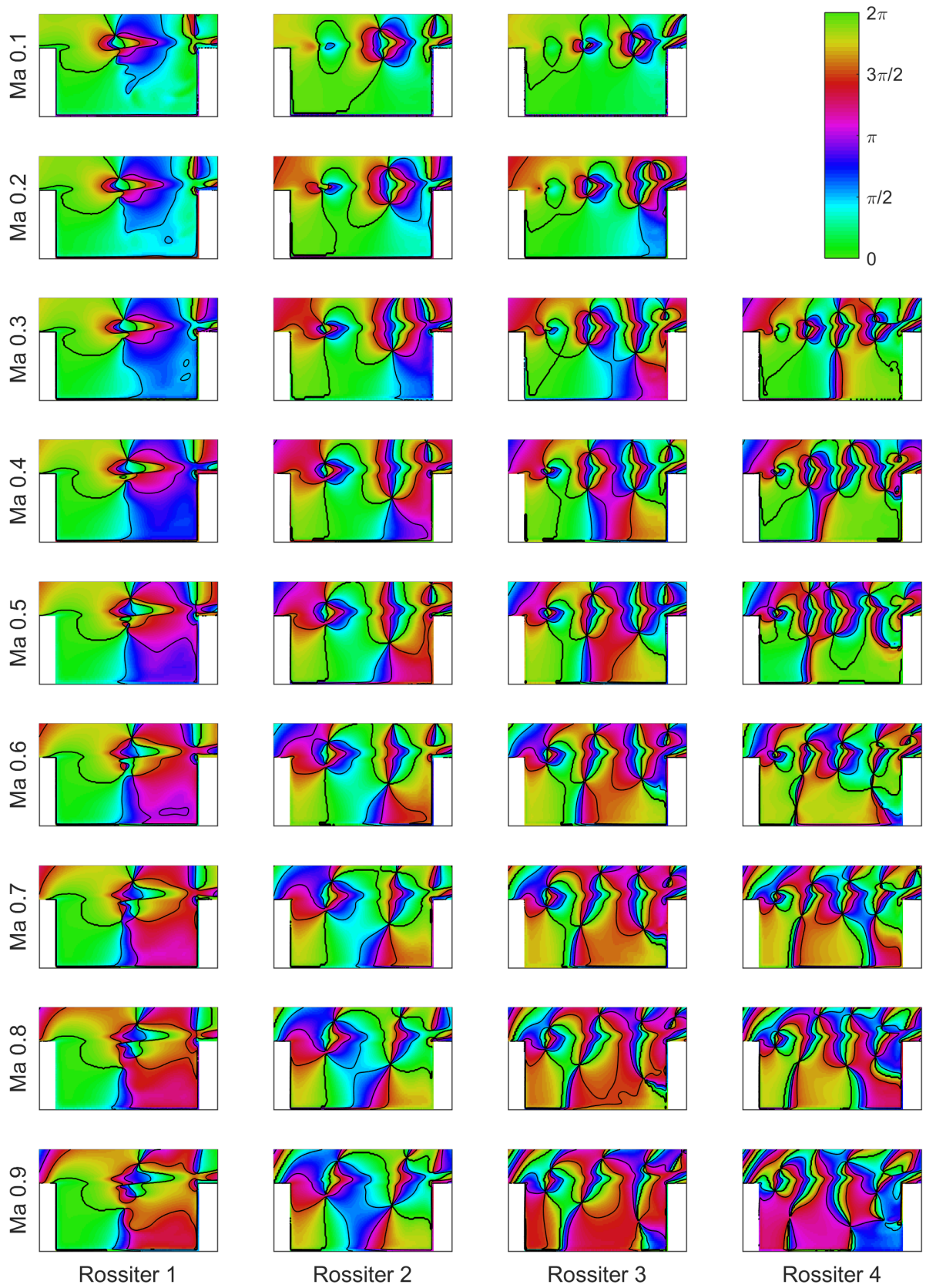


Figure 79 – Eigenfunction phases for pressure for various Rossiter modes and Mach numbers.

5.2 Influence of the boundary layer thickness

Another parameter sweep was performed for the incoming boundary layer thickness at the cavity. This time, the following parameters were used, based on the second Mach number sweep: Cavity aspect ratio $L/D = 2$, Reynolds number $Re_D = 1000$, Mach number $Ma = 0.5$.

The boundary layer thickness was defined by its relation to the cavity depth, in the range of $5 \leq D/\theta \leq 200$. In other words, changing the incoming boundary layer thickness while maintaining all other parameters means moving the cavity position in the flat plate. For the thinnest layer ($D/\theta = 200$), the cavity leading edge was positioned only 0.0567 depth units downstream from the flat plate leading edge. For the thickest boundary layer ($D/\theta = 5$), this distance was increased all the way to 90.72 depth units.

Figure 80 shows the eigenvalue maps for various boundary layer thicknesses. Rossiter modes 1 to 5 are indicated by the lines.

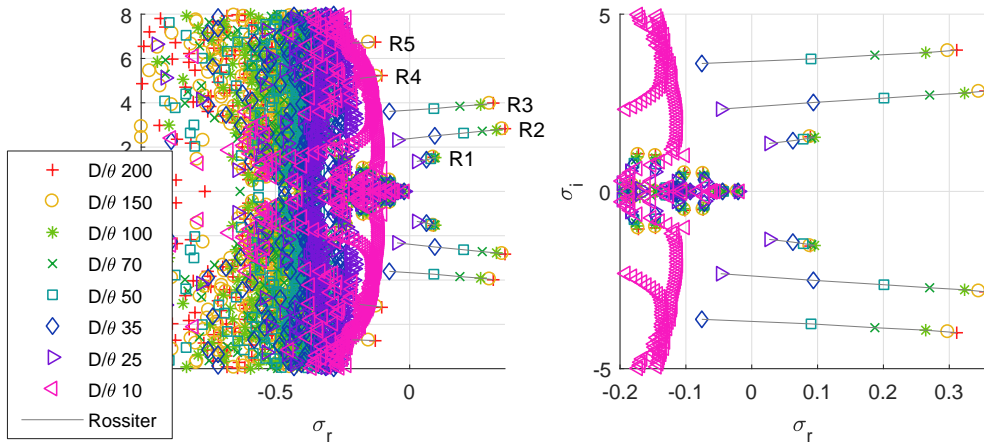


Figure 80 – Eigenvalues of the open cavity flow for various incoming boundary layer thicknesses.

Figure 81 depicts the effect of the boundary layer thickness on the three first Rossiter modes, both the the stability and the frequency. Thinner boundary layers tend to be less stable and oscillate faster. The increased frequency is due to the faster mean velocity the disturbances are convected through the mixing layer. The stability will be discussed at the next section.

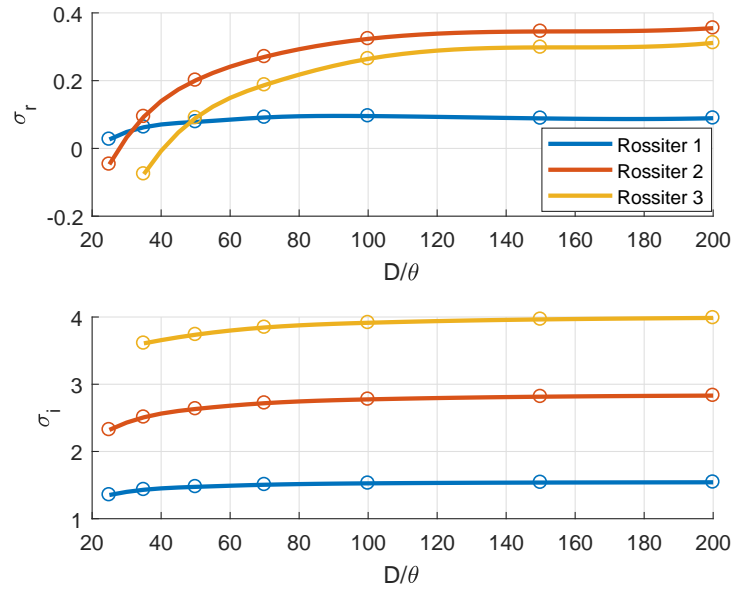


Figure 81 – Effect of the incoming boundary layer thickness on the eigenvalues of the Rossiter modes.

5.3 Relation to mixing layer instability

In both sweeps of Mach numbers and boundary layer thicknesses, the modes that presented the greatest sensitivity to these parameters were Rossiter-like modes i.e. eigenfunctions that resemble Rossiter modes at a linear stage.

This sensitivity can be related to two physical phenomena. The first is the spatial amplification at the mixing layer at the cavity opening, which takes small disturbances at the leading edge and amplify them on the way to the trailing edge. Thinner mixing layers tend to increase this amplifications, while higher Mach numbers tend to attenuate it. (CRIMINALE; JACKSON; JOSLIN, 2003)

The second phenomenon is the amount of acoustic feedback generated by the disturbance at the trailing edge that travels back to the leading edge. The mixing layer disturbance transfers part of its energy to acoustic waves inside the cavity, the amount of energy transfered may be called the sound emission. When this wave reaches the upstream side of the cavity, part of its energy is transfered back to the mixing layer disturbance, which may be called the flow receptivity. Higher Mach numbers tend to increase this (HOWE, 2004). Figure 82 illustrates both phenomena.

This section compares the spatial amplification at the mixing layer from the Orr-Sommerfeld equation to the results from the global instability analysis. The next section analyzes the acoustic receptivity influence.

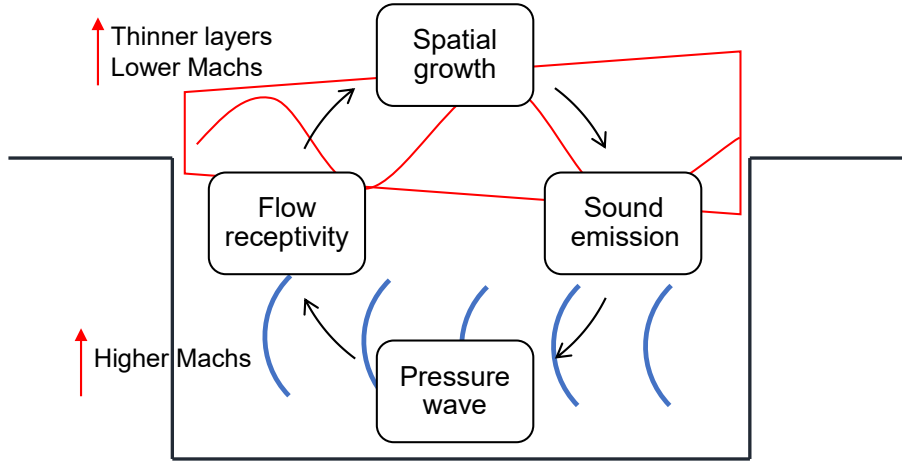


Figure 82 – Scheme of energy transfer phenomena in a Rossiter mode and its sensitivity to Mach number and mixing layer thickness.

5.3.1 Spatial instability analysis

The Orr-Sommerfeld equation is given by:

$$\frac{i}{Re} \left[\hat{v}^{(4)} - 2k^2 \hat{v}^{(2)} + \alpha^4 \hat{v} \right] + (\alpha \bar{u} - \omega) \left[\hat{v}^{(2)} - k^2 \hat{v} \right] - \alpha \bar{u}^{(2)} \hat{v} = 0 \quad (5.3)$$

Where $k = \sqrt{\alpha^2 + \beta^2}$, with α being the stream-wise wavenumber and β , the span-wise wavenumber. ω is the temporal frequency. \bar{u} is the base flow stream-wise velocity and \hat{v} , the disturbance. All derivatives are with respect to y , the wall-normal direction.

Both α and ω may be complex numbers, they relate to the flow disturbance in the following manner:

$$\tilde{v}(x, y, z, t) = \hat{v}(y) e^{i(\alpha x + \beta z - \omega t)} \quad (5.4)$$

In this analysis, the disturbances are two-dimensional, therefore, β is set to zero. The real parts of α and ω relate to the spatial and temporal frequencies, respectively. If the imaginary part of α is negative, the disturbance grows spatially and if the imaginary part of ω is positive, the disturbance grows with time.

For an spatial analysis, the imaginary part of ω is fixed to zero, causing the flow to be simply periodic in time. While in a temporal analysis, the imaginary part of α is null.

Equation 5.3 can be reorganized into a generalized eigenvalue problem, in the following manner. D is a derivative operator. (JUNIPER; HANIFI; THEOFILIS, 2014)

$$\mathbf{A} \hat{v} = \omega \mathbf{B} \hat{v} \quad (5.5)$$

$$\mathbf{A} = \frac{i}{Re} (D^4 - 2k^2 D^2 + \alpha^4) + \alpha \bar{u} (D^2 - k^2) - \alpha D^2 \bar{u} \quad (5.6)$$

$$\mathbf{B} = D^2 - k^2 \quad (5.7)$$

To obtain the spatial amplification of a certain frequency, one must integrate the imaginary part of α at a fixed ω through the mixing layer, which leads to:

$$\ln \frac{a}{a_0} = - \int_0^L \alpha_i dx \quad (5.8)$$

a_0 and a are the disturbance magnitude at the beginning (0) and at the end (L) of the mixing layer region, respectively. α_i is a function of both stream-wise position (x) and temporal frequency (ω_r).

5.3.2 Numerical implementation

The numerical solution of this equation is done as in the paper by Juniper, Hanifi and Theofilis (2014). In summary, the domain is discretized with the spectral collocation method using Chebychev polynomials.

By solving the eigenvalue problem, one retrieves a set of complex ω values for a given α , which is useful for an temporal analysis, as α can be chosen as a real value.

For the spatial analysis, Eq. 5.3 cannot be rearranged in a way to be solved as an eigenvalue problem with α in the place of ω , which would be very convenient, as real values of ω would be chosen and complex values of α would be retrieved.

The solution implemented in this work involves iterating imaginary parts of α until the imaginary part of ω is null in the most unstable mode retrieved.

This process is repeated for multiple velocity profiles from the cavity leading edge to its trailing edge.

Finally, for each temporal frequency ω_r , the spatial amplification α_i is integrated in the stream-wise direction. The flowchart in Fig. 83 summarizes the process. This algorithm was implemented and run in MATLAB®.

A quick mesh convergence analysis was run, 201 nodes were found to be enough. In this analysis, the domain boundaries were disregarded, it was made large enough so that the domains could be considered effectively infinite.

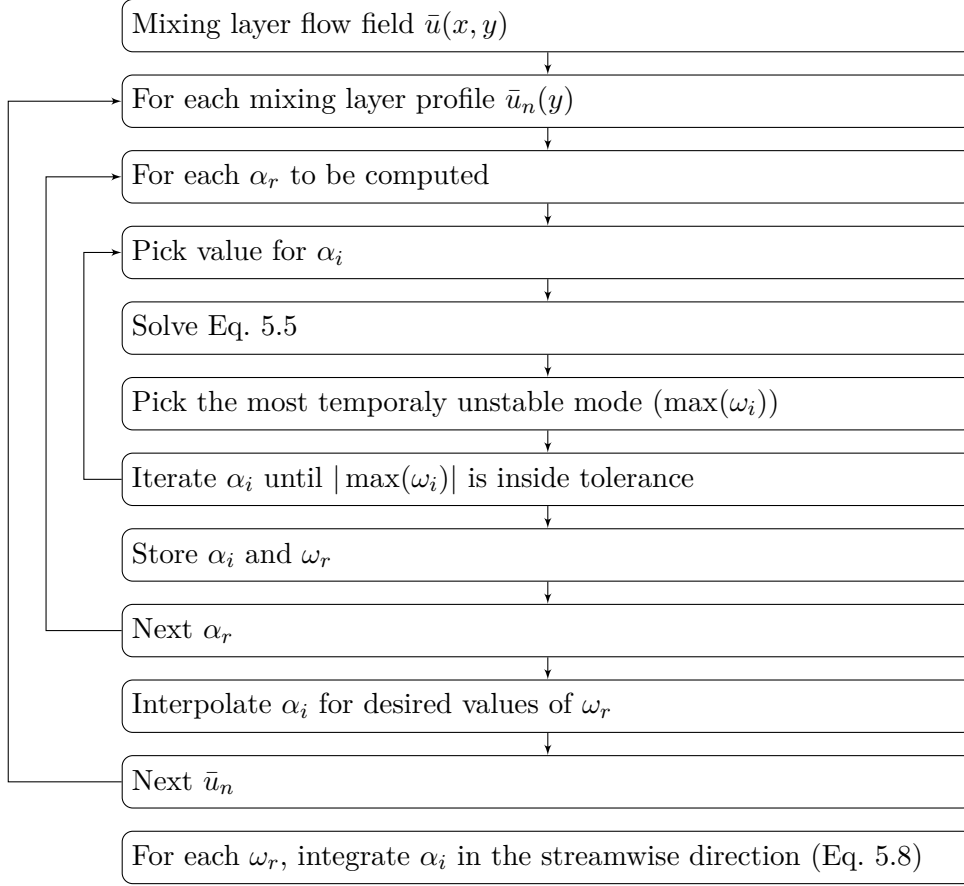


Figure 83 – Flowchart of mixing layer spatial instability analysis.

5.3.3 Comparison to the global instability

A series of cases at $Re_D = 1000$ was considered. The cavity's aspect ratio is fixed at $L/D = 2$. The global analysis was run at $Ma = 0.5$. The spatial instability analysis does not account for the compressibility. Various boundary layer thicknesses were run in the range $10 \leq D/\theta \leq 100$.

The mixing layer thickness is defined as:

$$T(x) = \frac{\Delta u}{\max\left(\frac{\partial \bar{u}}{\partial y}\right)} \quad (5.9)$$

Figure 84 shows the computed mixing layer thickness for various incoming boundary layer thicknesses.

Two types of cases were considered. In one, the stream-wise velocity directly from the DNS was used in the instability analysis, in the other, it was approximated by a hyperbolic tangent function. Figure 85 shows both velocity profiles for an incoming boundary layer thickness of $D/\theta = 10, 25, 100$.

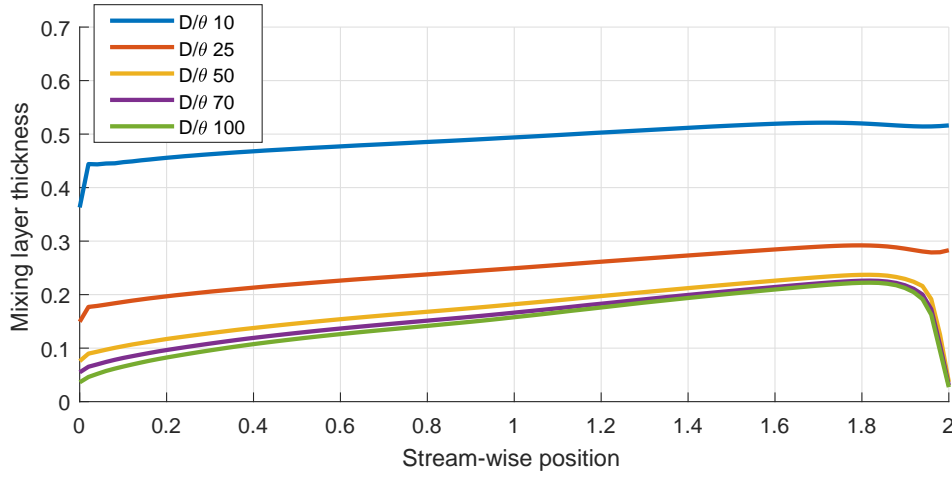


Figure 84 – Mixing layer thickness for various incoming boundary layer thicknesses.

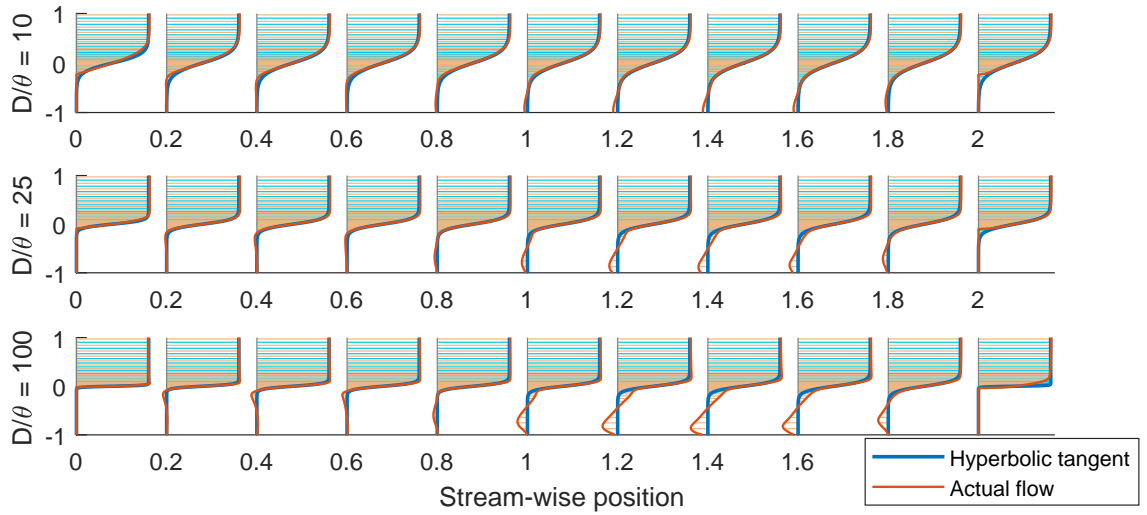


Figure 85 – Mixing layer profile and its hyperbolic tangent approximation for an incoming boundary layer thicknesses of $D/\theta = 10, 25, 100$.

The greatest difference between both profiles happens closer to the end of the cavity, where the recirculation is strongest, especially at thinner mixing layers. The last 5% of the cavity length in the stream-wise direction were left out of this analysis, as the parallel-flow approximation is not valid there and the stream-wise derivatives get too large.

Figure 86 compares the spatial amplification for the mixing layers to the temporal amplification rate from the global analysis. The full lines were obtained with the actual flow profiles, while dashed lines come from the hyperbolic tangent approximation. The asterisks are the global modes eigenvalues of Rossiter modes and the dots are other eigenvalues. $R1$ to $R5$ indicate Rossiter modes 1 to 5, respectively.

It can be seen there is a clear relation between the most amplified global mode

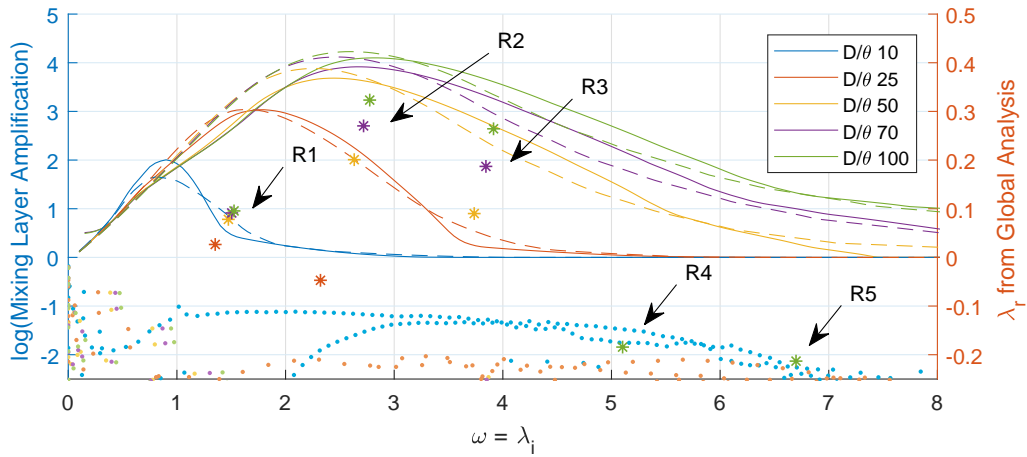


Figure 86 – Mixing layer spatial amplification compared to the global instability results.

and its respective spatial amplification at the mixing layer. The mixing layer instabilities favor a certain range of frequencies, which ends up selecting which of the Rossiter modes become the most unstable. In the case presented here, at D/θ ratios of 50 and above, the second Rossiter mode is the most favored by the mixing layer, closely followed by the third mode.

This analysis also sheds a light on the reason the first mode did not become increasingly more unstable as the incoming boundary layer got thinner. The mixing layer amplification around this frequency reaches a plateau after $D/\theta = 50$.

Note that Rossiter modes 4 and 5 do not become unstable at any point of this sweep, but they start becoming apparent for larger values of D/θ , as can also be seen in the left hand side of Fig. 80.

Figure 87 shows Rossiter modes 1 to 5 obtained by the global stability analysis at $Ma = 0.5$ and $D/\theta = 100$. In this case, the Reynolds number based on the mixing layer thickness is about 50 at the leading edge.

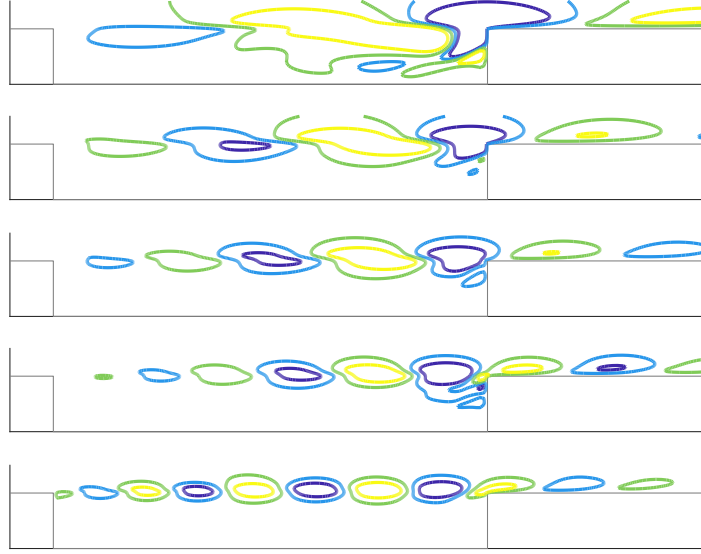


Figure 87 – Wall-normal velocity isocontours of Rossiter modes 1 to 5 from the global stability analysis at $Ma = 0.5$ and $D/\theta = 100$.

5.4 Cavity aeroacoustic emissions

As mentioned in the previous section, the second physical phenomenon that relates to the Rossiter modes' sensitivity to the Mach number is the acoustic receptivity at the cavity's trailing edge and the flow receptivity at its leading edge.

Greater receptivities result in more energy transferred by the acoustic waves to the beginning of the shear layer, which translates into more energy being released at its end.

One way of measuring the energy transfer into acoustic is to compare the disturbance magnitude at the shear layer, just before the cavity trailing edge, to the acoustic energy released. Instead of measuring the acoustic waves inside the cavity, where many other fluctuations are present, they are measured at the far-field, where a cleaner signal is found.

The cases from the Mach number sweep were used for this analysis: Reynolds number is $Re_D = 1149$. The cavity's aspect ratio is fixed at $L/D = 2$. The incoming boundary layer thickness is $\theta = 0.0337$. Mach number is in the range $0.05 \leq Ma \leq 0.9$.

The analysis was performed by picking the eigenfunctions corresponding to Rossiter modes for each Mach number and placing a series of probes. As shown in Fig. 88, shear layer probes were placed at three quarters across the cavity opening, ranging from -0.25 to 0.5 in the wall-normal direction, where zero is the flat-plate height. All lengths are normalized by the cavity depth. Various positions for the probes were tried with similar results.

Pressure fluctuation probes were placed in a semi-circumference centered at the cavity trailing edge with radius 2. This radius was chosen to be into the acoustic far-field but still away from interference by the boundary conditions.

Some near-field probes were also placed inside the cavity around the leading edge, to measure incoming acoustic waves.

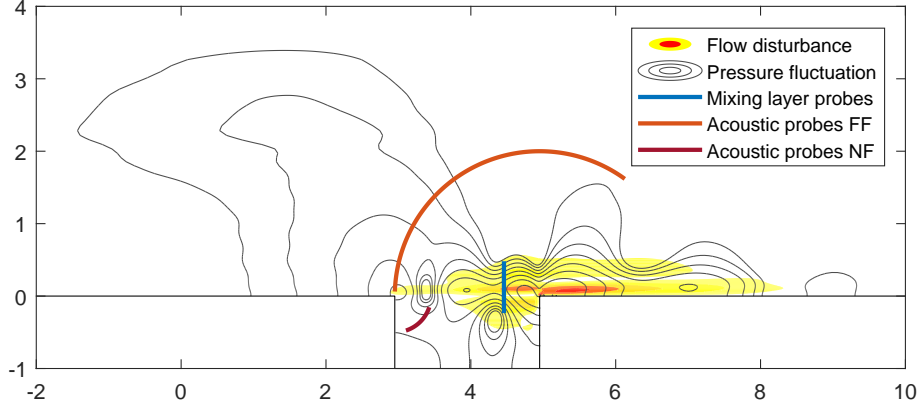


Figure 88 – Placement of probes for the acoustic receptivity analysis.

Isocontours of pressure and velocity disturbances from Rossiter mode 1 at Mach 0.6 were overlayed in Fig. 88 to better illustrate the flow.

The eigenfunction's absolute value is measured at each probe. The acoustic energy transfer is computed as the ratio of acoustic power in the far-field to the acoustic source term in the shear layer (HOWE, 2004), as in the following equations:

$$E_{SL} = \int_{P_{SL}} |\nabla \cdot (\boldsymbol{\omega} \wedge \mathbf{v})| dx \quad (5.10)$$

$$E_{Ac} = \int_{P_{Ac}} |p|^2 dx \quad (5.11)$$

$$ET_{Ac} = \frac{E_{Ac}}{E_{SL}} \quad (5.12)$$

P_{SL} and P_{Ac} are the shear layer and acoustic probes. p , \mathbf{v} and $\boldsymbol{\omega}$ are respectively pressure, velocity and vorticity from the eigenfunctions. Pressure and velocities are normalized by their respective far-field values, the vorticity is computed from the velocities.

Figure 89 shows the transfer into acoustic calculated for various Mach numbers, for Rossiter modes 1 and 2.

Howe (2004) implies that at most frequencies, a dipole dominates the acoustic emission of the open cavity. Physically, it relates to the aerodynamic drag oscillations.

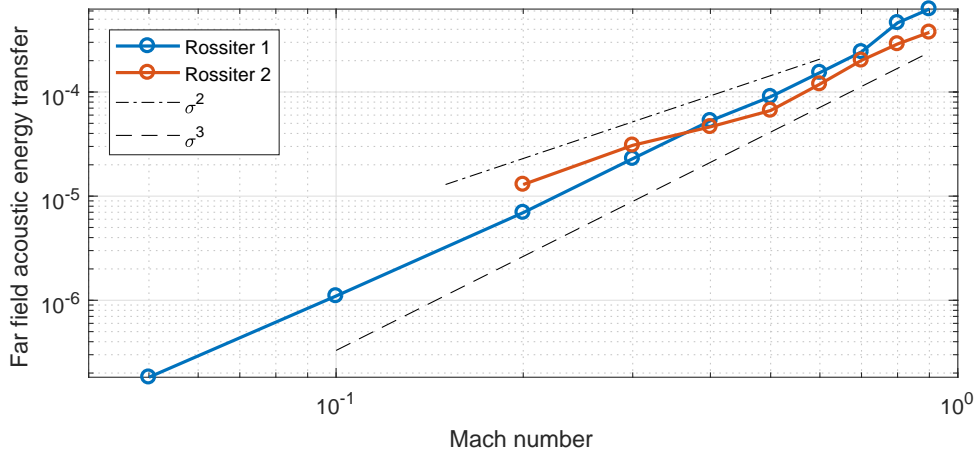


Figure 89 – Far field acoustic receptivity measured for various Mach numbers for Rossiter modes 1 and 2.

The dipole acoustic intensity varies with $\sigma(\rho_0 U^3 Ma^3)$, which matches the scaling to Ma^3 found in Fig. 89 for most frequencies, as both ρ_0 and U are fixed.

Around the frequencies of the second Rossiter mode and low Mach numbers ($Ma \approx 0.1$), Howe's results show there is a peak in monopole acoustic emission, which explains the increased receptivity observed for this mode at $Ma \leq 0.3$ and why this region varies with $\sigma(Ma^2)$. Figure 90 shows the acoustic pressure spectrum at Mach 0.1, the monopole peak occurs around $fL/U = 1$, which corresponds to the second Rossiter mode. This monopole peak moves to lower frequencies as the Mach number is increased. This spectra

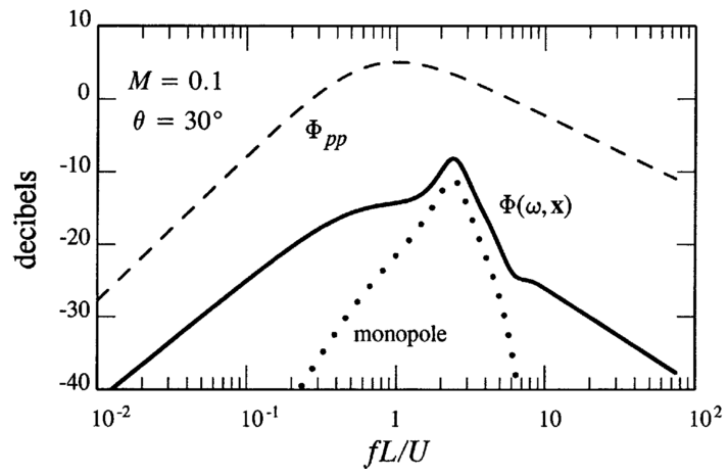


Figure 90 – Acoustic pressure spectrum for Mach 0.1. (HOWE, 2004)

By using the near-field probes, one can estimate how much of the shear-layer oscillation at the trailing edge translates into acoustic power near the leading edge, which will generate new shear-layer oscillations. This time, the acoustic power to Mach number

relation has varied from $\sigma(Ma^3)$ to $\sigma(Ma^1)$ as either the Mach number or the frequency were increased, as shown in Fig. 91.

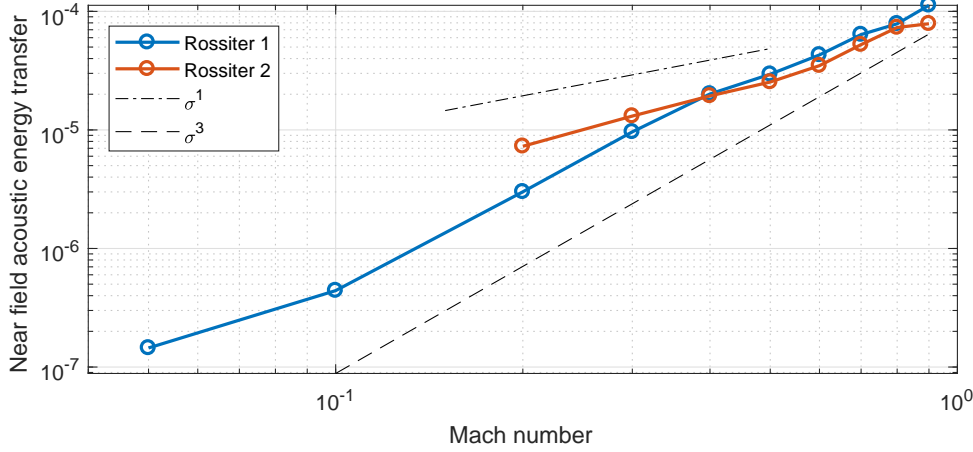


Figure 91 – Near field acoustic receptivity measured for various Mach numbers for Rossiter modes 1 and 2.

This analysis has always considered the oscillation magnitude at the end of the shear layer to be constant. In a global analysis, as the Mach number increases, a larger acoustic pressure reaching the leading edge will trigger greater oscillations in the shear layer, adding up the effects. Therefore, if other phenomena are disregarded, one may expect the overall acoustic emission to increase with up to $\sigma(\rho_0^2 U^6 Ma^6)$. In a real flow, considering the Mach number to scale linearly with the velocity, one may observe the acoustic emission to increase with powers as high as $\sigma(U^{12})$ or $\sigma(Ma^{12})$.

Increasing the Mach number has a stabilizing effect in the shear layer, which reduces the overall sound emission, causing some situations where the instability does not increase with Mach, as observed back in Figs 71 and 77.

5.5 Comparison to simulation results

So far, all results were focused on small disturbances around the base flow, where non-linear effects are negligible. This section compares the previous linear stability results to fully non-linear simulations by the DNS code.

In these runs, the second Mach number sweep was used as base. Cavity aspect ratio $L/D = 2$, Reynolds number $Re_D = 1000$, Incoming boundary layer thickness $\theta = 0.01$, Mach number $0.1 \leq Ma \leq 0.9$. The initial condition for the simulations was the base-flow, from which the numerical residuals would grow due to the flow instabilities.

The time series obtained for each case is shown in Fig. 92. The stream-wise velocity

was recorded at an arbitrary point chosen in the middle of the cavity, at the flat plate height. All cases start at a linear regime, where the frequency and the growth rate match those of the linear analysis, before non-linear effects kick in, causing the mean flow to differ from the base flow, shifting the frequencies and causing all cases to reach a limit-cycle.

Note that the y axis in this figure was shifted, to improve visualization. The different times before reaching the limit-cycle in this figure cannot be compared from case to case, as the initial disturbance, caused by numerical residuals in the base flow, was not the same for all cases.

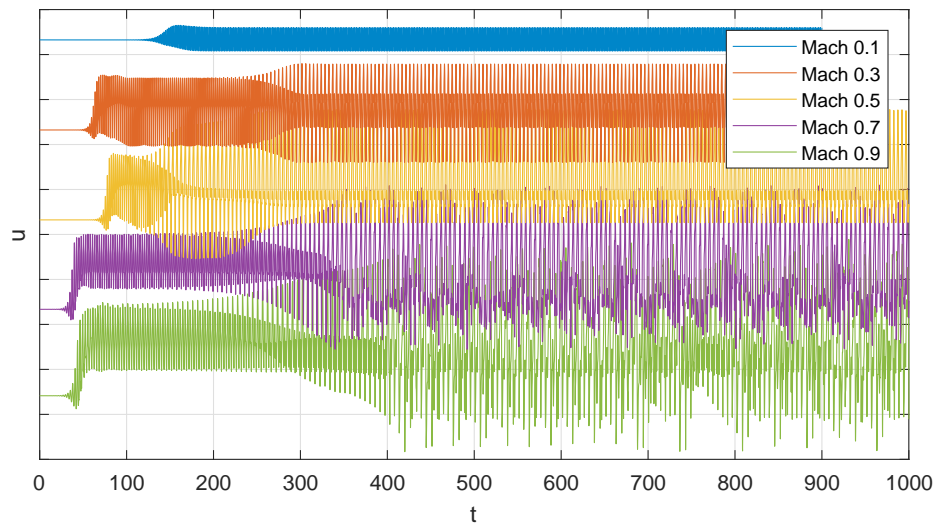


Figure 92 – Time series of stream-wise velocity for various Mach numbers. Each vertical tick represents a quarter of the free flow velocity. Note that the plots were vertically shifted.

The Mach 0.1 case has reached a periodic state correspondent to Rossiter mode 2. Mach 0.3 and 0.5 cases have also settled for Rossiter mode 2, but with a subharmonic present, likely indicating an instability at Rossiter mode 1, which is not large enough to outgrow mode 2. This subharmonic, physically, means that the vortex street is composed of alternating stronger and weaker vortices. This strength difference is greater in the Mach 0.5 case.

Mach 0.7 and 0.9 cases did not settle for a single Rossiter mode, instead, they kept switching between modes 1 and 2. Figure 93 shows a close up at the beginning of the series. Note that the time axis was manually shifted for each case. Figure 94 shows a shorter portion of time after the limit cycle has been reached, where both higher Mach numbers can be seen switching modes. Figure 95 shows snapshots of the pressure fluctuation at arbitrary times after the initial transient.

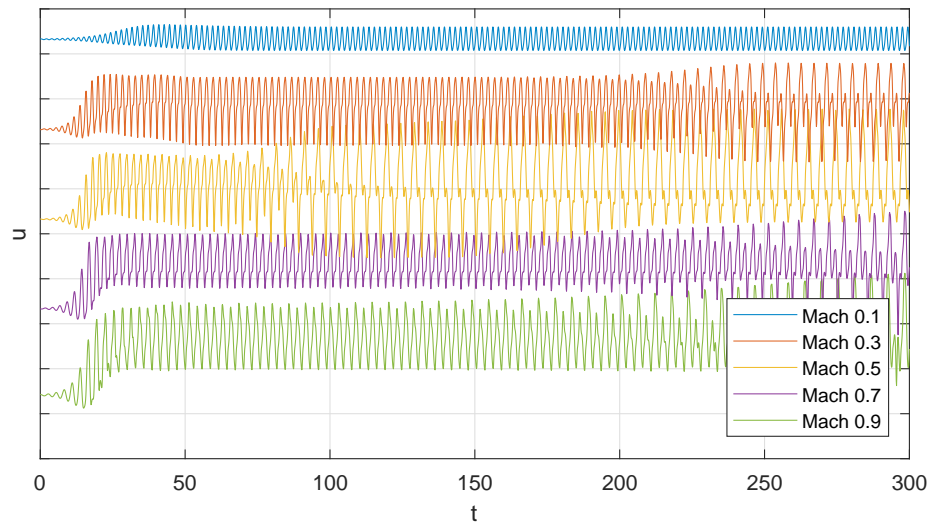


Figure 93 – Close up at the beginning of the time series of stream-wise velocity for various Mach numbers. Each vertical tick represents a quarter of the free flow velocity. Note that the plots were horizontally and vertically shifted.

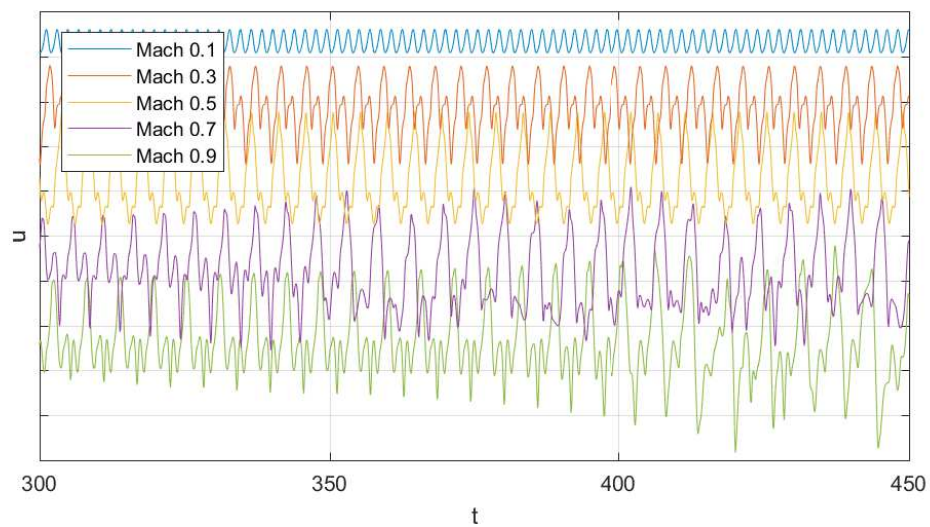


Figure 94 – Close up of time series of stream-wise velocity for various Mach numbers. Each vertical tick represents a quarter of the free flow velocity. Note that the plots were vertically shifted.

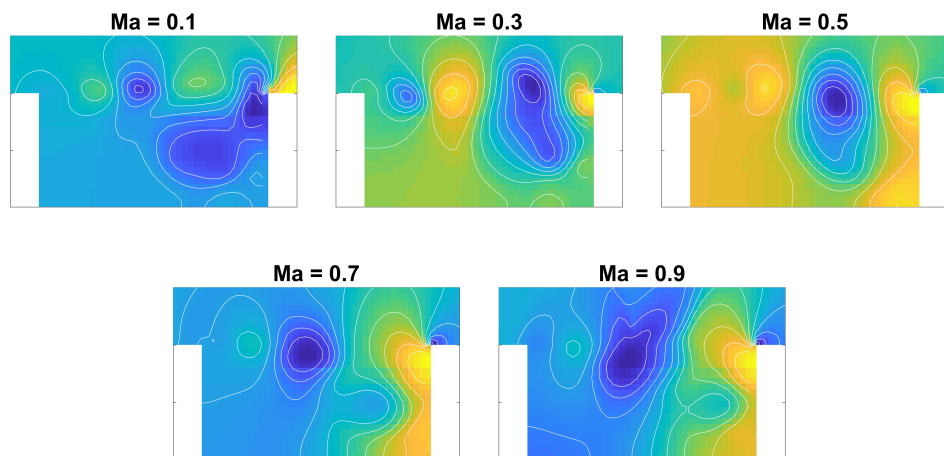


Figure 95 – Snapshots of the pressure fluctuation in the DNS for various Mach numbers.

The spectra was computed by Welch's power spectral density estimate. The transient phase was ignored. It is shown in Fig. 96.

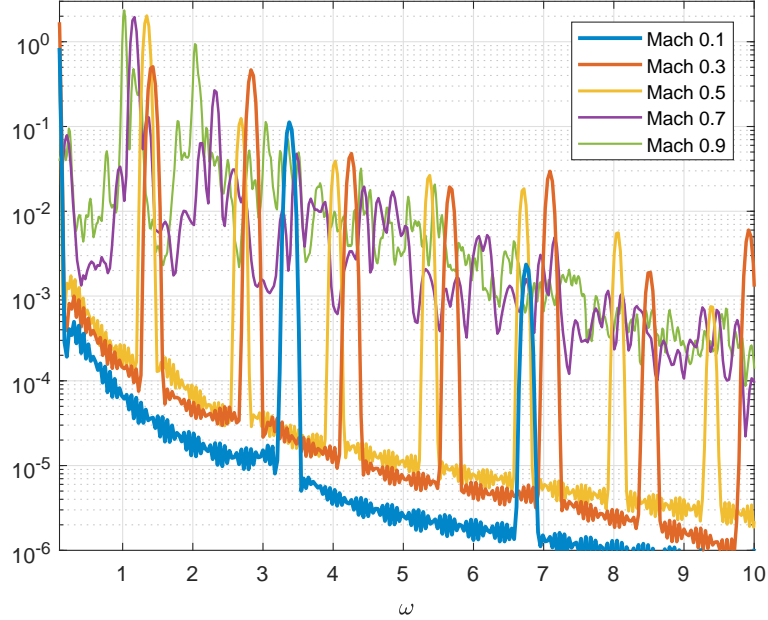


Figure 96 – Spectra of the stream-wise velocity for various Mach numbers.

The peaks from the Fourier transform were organized in Tab. 12. Cells shaded in blue indicate Rossiter mode 2.

For all cases, Rossiter mode 2 is dominant. At Mach 0.3 and above, its subharmonic is also present, likely excited by Rossiter mode 1, which has a similar frequency and is also unstable, albeit at a lower rate. The harmonics of both Rossiter mode 2 and its first subharmonic are also visible, but with smaller magnitudes.

As predicted by the linear stability theory, the second Rossiter mode was the first to appear in all cases, but it was not sustained as the only mode for long at the higher Mach numbers. This may be caused because the mean flow for those cases became significantly different from the base flow.

At lower Mach numbers, the prediction by the global stability analysis is closer

Table 12 – Peaks from the Fourier transform of DNS data compared to Rossiter modes and global modes

| Mach | DNS 1 | DNS 2 | DNS 3 | Ross. 1 | Ross. 2 | Global 1 | Global 2 |
|------|-------|-------|-------|---------|---------|----------|----------|
| 0.1 | 3.38 | 6.77 | 10.13 | 1.27 | 2.97 | 1.95 | 3.40 |
| 0.3 | 1.42 | 2.83 | 4.26 | 1.15 | 2.68 | 1.77 | 3.05 |
| 0.5 | 1.34 | 2.68 | 4.03 | 1.05 | 2.44 | 1.53 | 2.77 |
| 0.7 | 1.17 | 2.31 | 3.48 | 0.96 | 2.24 | 1.35 | 2.50 |
| 0.9 | 1.02 | 2.03 | 3.04 | 0.89 | 2.07 | 1.22 | 2.28 |

than Rossiter's equation, while the opposite is true at higher Mach numbers. This is attributed to the fact that, at lower Mach numbers, the oscillation amplitude at the DNS is smaller than at higher Mach numbers, meaning that it is still close to the linear regime assumed by the global stability analysis.

The vortex street at the cavity opening causes the mean thickness of the shear layer to increase, which, in turn, causes the amplification at higher frequencies to decrease. The analysis used to generate Fig. 86 was run again, with the mean flows from the simulation.

Figure 98 shows how the mean mixing layer thickness increases with the Mach number. The profiles can be seen in Fig. 98. Also note the increased back-flow magnitude, up to 50% of the free flow. The base flow from the Mach 0.5 case is shown, its sensibility to the Mach number is negligible.

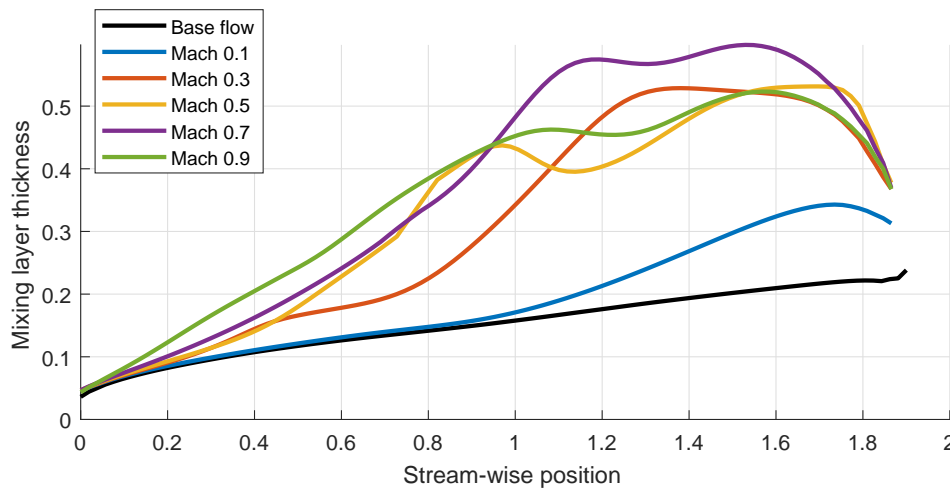


Figure 97 – Mean mixing layer thickness for various Mach numbers.

Figure 99 compares the spatial amplification for the mixing layers to the temporal amplification rate from the global analysis. The full lines were obtained with the actual flow, while dashed lines come from the hyperbolic tangent approximation. The asterisks are the global modes eigenvalues of Rossiter modes and the dots are other eigenvalues, run at Mach 0.5. $R1$ to $R5$ indicate Rossiter modes 1 to 5, respectively. It is very important to note that this spatial instability analysis does not consider the Mach number directly, only its effect to the mean flow. An increasing Mach number is expected to further lower the amplification rate.

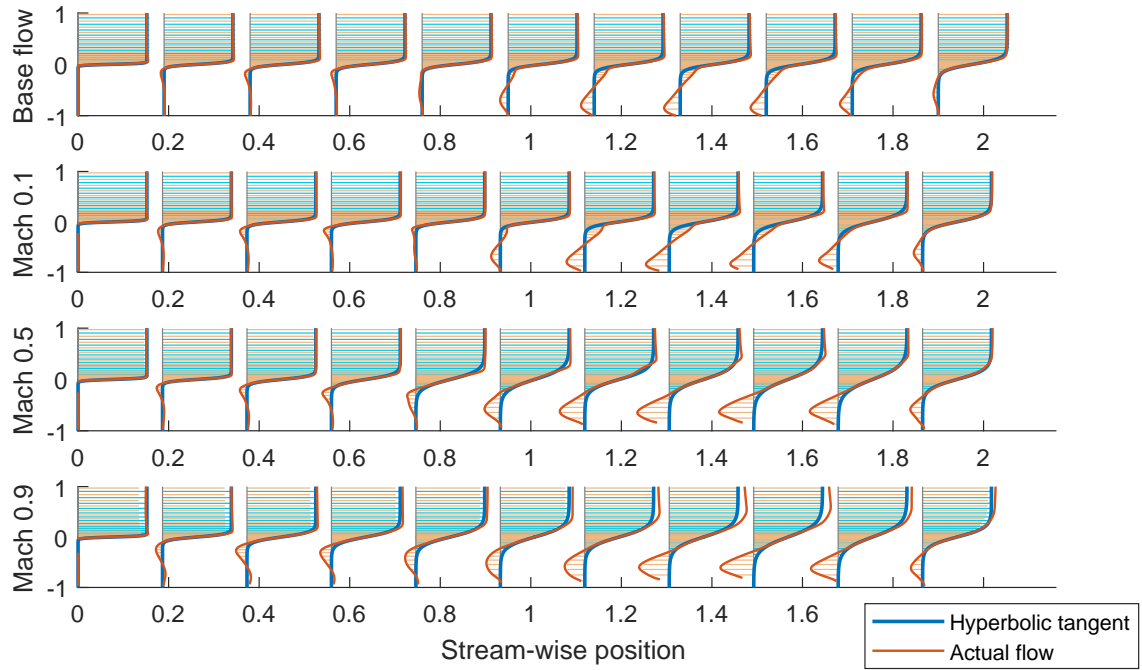


Figure 98 – Mean mixing layer profile and its hyperbolic tangent approximation for various Mach numbers and the respective base flow.

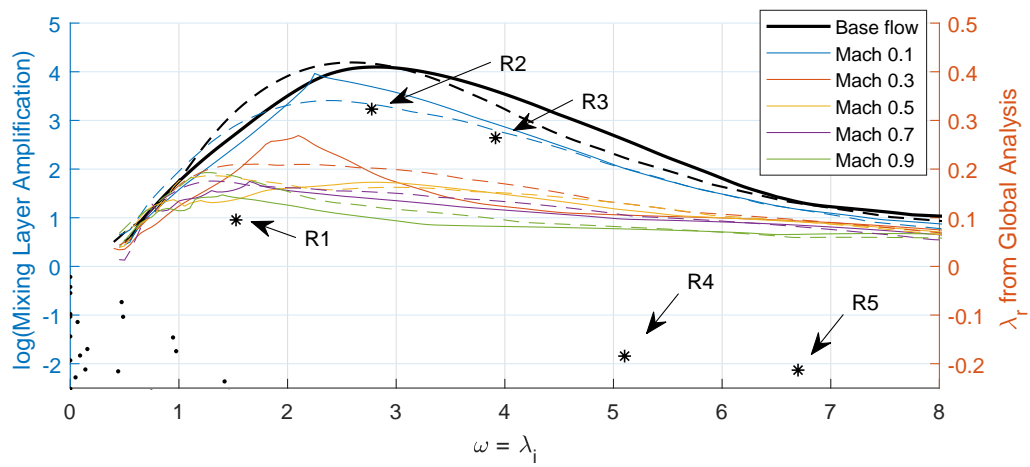


Figure 99 – Mixing layer spatial amplification compared to the global instability results for mean flows of various Mach numbers.

Chapter 6

Discussion

6.1 Conclusion

This work was divided in two main parts. First, the DNS was adapted for the open cavity flow and the Jacobian-free instability method was implemented and validated. Later, these tools were used to analyze the stability of two-dimensional flows and their respective modes, looking for physical explanations for the observed phenomena.

6.1.1 Method implementation

The DNS code from the work of Martinez (2016) was used as base and adapted to support Cartesian geometry features such as steps and rectangular cavities. All parallel processing features by domain decomposition were kept and OpenMP capability was added.

The compact numerical derivatives by Lele (1992) allowed to mesh convergence to happen with a few hundred nodes in the stream-wise and wall-normal directions and from 8 to 12 nodes in the span-wise direction.

The Selective Frequency Damping method, by Åkervik et al. (2006), works as a low pass filter in the time domain and allows a base flow to be found even if the physical flow is unstable. It has also allowed the buffer zones close to the domain boundaries to work properly.

The Jacobian-free instability analysis method by Eriksson and Rizzi (1985) and Chiba (1998) was successful in retrieving the most unstable modes, as confirmed when comparing to the Residual Algorithm by Theofilis (2000b). Its memory usage was very low when compared to storing the Jacobian matrix.

Total computing time for generating a base flow is in the order of some hours to a day or two. The instability analysis for a 2D case takes some hours, while a 3D analysis scales into a few days.

Three dimensional runs could be optimized if the DNS was capable of considering the span-wise direction as spectral, instead of spatial. As the work has focused on 2D flows, it was decided that it was not worth investing time to implement this feature.

Convergence analysis were performed for all relevant parameters. The mesh and the domain for the DNS and the time span, the number of iterations and the disturbance magnitude for the instability analysis algorithm. An interesting relation between the number of DNS steps for each Arnoldi iteration and the total number of Arnoldi iterations was found and confirmed by the literature.

6.1.2 Main findings

Three types of physical phenomena were investigated for their influences on the Rossiter modes (ROSSITER, 1964).

The resonance between standing wave modes (PLUMBLEE; GIBSON; LASSITER, 1962) and Rossiter modes was found to only have a limited influence. It was more easily visible in Rossiter mode 4 of the second Mach number sweep, which was stable in most cases. More unstable modes were not significantly affected by the standing wave modes. See Fig. 78. This effect is expected to be of greater importance if the cavity is larger when compared to the mixing layer.

The mixing layer instability at the cavity opening has a clear relation to which Rossiter modes are amplified. See Fig. 86. Thinner mixing layers are more unstable spatially, which means even small disturbances at the leading edge may cause large fluctuations at the trailing edge.

This effect is attenuated by an increasing Mach. First, a larger Mach number causes a same velocity profile to become more stable spatially. Second, in a real case, instabilities will cause vortices to form, widening the mixing layer of the mean flow, causing them to be more stable. See Figs. 97 and 99.

On the other hand, and increasing Mach number causes the flow to acoustic energy transfer to be more efficient, reducing losses in the acoustic feedback of the Rossiter modes. See Fig. 89. As noted by Howe (2004), the acoustic source may be a dipole or a monopole, for which the energy transfer efficiencies increase with the Mach number with powers of 2 and 3, respectively.

6.2 Suggestion for future works

This work has focused on cases in which the boundary layer thickness is at least one order of magnitude smaller than the cavity. It was also limited to a cavity aspect ratio of two in the parameter sweeps. It is expected that the cavity depth may reach a point where it no longer plays an important role in the stability, therefore the D/θ parameter would not be relevant anymore, only the L/θ value. There may also be a point where the cavity length becomes so great that it behaves as two separate steps rather than as a single cavity.

On the other side of the parameter spectrum, shallow cavities may be studied, in which the cavity depth is comparable to or smaller than the boundary layer thickness. In some cases, the cavities may be so small that, instead of being defined geometrically, small changes to the boundary conditions may suffice to represent them.

Bibliography

ÅKERVIK, E. et al. Steady solutions of the Navier-Stokes equations by selective frequency damping. **Physics of Fluids**, v. 18, n. 6, p. 068102, 2006. ISSN 10706631. Available from Internet: <<http://scitation.aip.org/content/aip/journal/pof2/18/6/10.1063/1.2211705>>.

ARNOLDI, W. E. The principle of minimized iterations in the solution of the matrix eigenvalue problem. **Quarterly of Applied Mathematics**, v. 9, n. 1, p. 17–29, 1951.

BARKLEY, D. Linear analysis of the cylinder wake mean flow. **EPL (Europhysics Letters)**, v. 75, n. 5, p. 750, 2006. Available from Internet: <<http://stacks.iop.org/0295-5075/75/i=5/a=750>>.

BERGAMO, L. F. **Instabilidade hidrodinâmica linear do escoamento compressível em uma cavidade**. apr 2014. Tese (Master Thesis) — Universidade de São Paulo, São Carlos, apr 2014. Available from Internet: <<http://www.teses.usp.br/teses/disponiveis/18/18148/tde-28052014-164324/>>.

BLOCK, P. J. W. **Noise response of cavities of varying dimensions at subsonic speeds**. [S.l.], 1976. 1–36 p.

BOTELLA, O.; PEYRET, R. Benchmark spectral results on the lid-driven cavity flow. **Computers and Fluids**, v. 27, n. 4, p. 421–433, may 1998. ISSN 00457930. Available from Internet: <<http://linkinghub.elsevier.com/retrieve/pii/S0045793098000024>>.

BOUTHIER, M. Stabilité linéaire des écoulements presque parallèles. **Journal de Mécanique**, v. 11, n. 4, p. 75–95, 1972.

BRÈS, G. A.; COLONIUS, T. Three-dimensional instabilities in compressible flow over open cavities. **Journal of Fluid Mechanics**, v. 599, p. 309–339, mar 2008. ISSN 0022-1120. Available from Internet: <http://www.journals.cambridge.org/abstract_S0022112007009925>.

CATTAFESTA, L. N.; GARG, S.; KEGERISE, M. A.; JONES, G. Experiments on compressible flow-induced cavity oscillations. In: **29th AIAA, Fluid Dynamics Conference**. Reston, Virigina: American Institute of Aeronautics and Astronautics, 1998. Available from Internet: <<http://arc.aiaa.org/doi/abs/10.2514/6.1998-2912>>.

CATTAFESTA, L. N.; WILLIAMS, D. R.; ROWLEY, C. W.; ALVI, F. S. Review of Active Control of Flow-Induced Cavity Resonance. **33rd AIAA Fluid Dynamics Conference**, p. 1–20, 2003.

CHIBA, S. Global Stability Analysis of Incompressible Viscous Flow. **Journal of Japan Society of Computational Fluid Dynamics**, v. 7, n. 1, p. 20–48, 1998.

COLONIUS, T. An overview of simulation, modeling, and active control of flow/acoustic resonance in open cavities. In: **39th Aerospace Sciences Meeting and Exhibit**. Reno, NV, USA: [s.n.], 2001. p. 1 – 12. Available from Internet: <<http://arc.aiaa.org/doi/abs/10.2514/6.2001-76>>.

COLONIUS, T.; BASU, A. J.; ROWLEY, C. W. Computation of sound generation and flow-acoustic instabilities in the flow past an open cavity. In: **Proceedings of the Joint Fluids Engineering Conference**. San Francisco, USA: [s.n.], 1999.

CRIMINALE, W. O.; JACKSON, T. L.; JOSLIN, R. D. **Theory and Computation of Hydrodynamic Stability**. 1. ed. [S.l.]: Cambridge University Press, 2003. ISBN 0521632005.

DIX, R. E.; BAUER, R. C. **Experimental and Theoretical Study of Cavity Acoustics**. [S.l.], 2000.

DRELA, M.; GILES, M. B. Viscous-inviscid analysis of transonic and low Reynolds number airfoils. **AIAA Journal**, v. 25, n. 10, p. 1347–1355, 1987. ISSN 0001-1452.

EAST, L. Aerodynamically induced resonance in rectangular cavities. **Journal of Sound and Vibration**, v. 3, n. 3, p. 277–287, 1966. ISSN 0022460X.

EDWARDS, W. S.; TUCKERMAN, L. S.; FRIESNER, R. A.; SORENSEN, D. C. Krylov Methods for the Incompressible Navier-Stokes Equations. **Journal of Computational Physics**, v. 110, n. 1, p. 82–102, 1994. ISSN 00219991. Available from Internet: <<http://www.sciencedirect.com/science/article/B6WHY-45P0TV7-64/2/cad045b7eaecfacc4e6ac09fb79d14c8>>.

EMMONS, H. W. The Laminar-Turbulent Transition in a Boundary Layer-Part I. **Journal of the Aeronautical Sciences**, American Institute of Aeronautics and Astronautics, v. 18, n. 7, p. 490–498, jul 1951. Available from Internet: <<http://arc.aiaa.org/doi/abs/10.2514/8.2010>>.

ERIKSSON, L. E.; RIZZI, A. Computer-aided analysis of the convergence to steady state of discrete approximations to the euler equations. **Journal of Computational Physics**, v. 57, n. 1, p. 90–128, 1985. ISSN 10902716.

FFOWCS-WILLIAMS, J. E. Aeroacoustics. **Annual Review of Fluid Mechanics**, v. 9, n. 1, p. 447–468, 1977.

_____. Aeroacoustics. **Journal of Sound and Vibration**, v. 190, n. 3, p. 387–398, 1996. ISSN 0022460X. Available from Internet: <<http://www.sciencedirect.com/science/article/pii/S0022460X9690070X>>.

GAITONDE, D. V.; VISBAL, M. R. **High-Order Schemes for Navier-Stokes Equations: Algorithm and Implementation Into FDL3DI**. [S.l.], 1998.

GASTER, M. A note on the relation between temporally-increasing and spatially-increasing disturbances in hydrodynamic stability. **Journal of Fluid Mechanics**, v. 14, n. 02, p. 222, oct 1962. ISSN 0022-1120. Available from Internet: <http://www.journals.cambridge.org/abstract_S0022112062001184>.

_____. On the generation of spatially growing waves in a boundary layer. **Journal of Fluid Mechanics**, v. 22, n. 03, p. 433, jul 1965. ISSN 0022-1120. Available from Internet: <http://www.journals.cambridge.org/abstract_S0022112065000873>.

GHARIB, M.; ROSHKO, A. The effect of flow oscillations on cavity drag. **Journal of Fluid Mechanics**, v. 177, n. -1, p. 501, apr 1987. ISSN 0022-1120. Available from Internet: <http://www.journals.cambridge.org/abstract_S002211208700106X>.

GHIA, U.; GHIA, K. N.; SHIN, C. T. High-Re Solutions for incompressible flow using the Navier-Stokes equations and a Multigrid Method. **Journal of Computational Physics**, v. 48, p. 387–411, 1982.

GLOERFELT, X. Cavity noise. **von Karman Instiut Lecture Notes on Aerodynamic Noise from Wall-Bounded Flows**, Citeseer, v. 3, p. 1–169, 2009.

GÓMEZ, F.; CLAINCHE, S. L.; PAREDES, P.; HERMANN, M.; THEOFILIS, V. Four Decades of Studying Global Linear Instability: Progress and Challenges. **AIAA Journal**, v. 50, n. 12, p. 2731–2743, dec 2012. ISSN 0001-1452. Available from Internet: <<http://arc.aiaa.org/doi/abs/10.2514/1.J051527>>.

GÓMEZ, F.; GÓMEZ, R.; THEOFILIS, V. On three-dimensional global linear instability analysis of flows with standard aerodynamics codes. **Aerospace Science and Technology**, Elsevier Masson SAS, v. 32, n. 1, p. 223–234, jan 2014. ISSN 12709638. Available from Internet: <<http://dx.doi.org/10.1016/j.ast.2013.10.006http://linkinghub.elsevier.com/retrieve/pii/S1270963813001879>>.

GÓMEZ, F.; PÉREZ, J. M.; BLACKBURN, H. M.; THEOFILIS, V. On the use of matrix-free shift-invert strategies for global flow instability analysis. **Aerospace Science and Technology**, v. 44, p. 69–76, jul 2015. ISSN 12709638. Available from Internet: <<http://linkinghub.elsevier.com/retrieve/pii/S1270963814002284>>.

HELLER, H. H.; HOLMES, D. G.; COVERT, E. E. Flow-induced pressure oscillations in shallow cavities. **Journal of Sound and Vibration**, v. 18, n. 4, p. 545–553, 1971. ISSN 10958568.

HOUGHTON, E. L.; CARPENTER, P. W.; COLLICOTT, S.; VALENTINE, D. **Aerodynamics for Engineering Students**. Elsevier Science, 2012. ISBN 9780080966335. Available from Internet: <<https://books.google.com.br/books?id=rA6mIXaF69kC>>.

HOWE, M. S. Edge, cavity and aperture tones at very low Mach numbers. **Journal of Fluid Mechanics**, v. 330, p. S0022112096003606, jan 1997. ISSN 00221120. Available from Internet: <http://www.journals.cambridge.org/abstract_S0022112096003606>.

_____. Mechanism of sound generation by low Mach number flow over a wall cavity. **Journal of Sound and Vibration**, v. 273, n. 1-2, p. 103–123, 2004. ISSN 0022460X. Available from Internet: <<http://linkinghub.elsevier.com/retrieve/pii/S0022460X03006448>>.

INGEN, J. L. van. A suggested semi-empirical method for the calculation of the boundary layer transition region. In: TECHNISCHE HOGESCHOOL. **Second European Aeronautical Congress, Scheveningen, Netherlands**. Delft, Netherlands, 1956.

JUNIPER, M. P.; HANIFI, A.; THEOFILIS, V. Modal Stability Theory Lecture notes from the FLOW-NORDITA Summer School on Advanced Instability Methods for Complex Flows, Stockholm, Sweden, 2013 1. **Applied Mechanics Reviews**, v. 66, n. 2, p. 021004, mar 2014. ISSN 0003-6900. Available from Internet: <<http://appliedmechanicsreviews.asmedigitalcollection.asme.org/article.aspx?doi=10.1115/1.4026604>>.

KEGERISE, M. A.; SPINA, E. F.; GARG, S.; Cattafesta III, L. N. Mode-switching and nonlinear effects in compressible flow over a cavity. **Physics of Fluids**, v. 16, n. 3, p. 678–687, 2004. ISSN 10706631.

KLEBANOFF, P. S.; TIDSTROM, K. D. **Evolution of amplified waves leading to transition in a boundary layer with zero pressure gradient**. Washington, 1959. Available from Internet: <<http://hdl.handle.net/2060/19890068568>>.

KNISELY, C.; ROCKWELL, D. Self-sustained low-frequency components in an impinging shear layer. **Journal of Fluid Mechanics**, v. 116, n. -1, p. 157, mar 1982. ISSN 0022-1120. Available from Internet: <http://www.journals.cambridge.org/abstract_S002211208200041X>.

KOLMOGOROV, A. N. **The Local Structure of Turbulence in Incompressible Viscous Fluid for Very Large Reynolds Numbers**. 1991. 9–13 p.

KOOK, H.; MONGEAU, L. Analysis of the periodic pressure fluctuations induced by flow over a cavity. **Journal of Sound and Vibration**, v. 251, n. 5, p. 823–846, apr 2002. ISSN 0022460X. Available from Internet: <<http://linkinghub.elsevier.com/retrieve/pii/S0022460X01940131>>.

KRISHNAMURTY, K. **Acoustic Radiation from Two-dimensional Rectangular Cutouts in Aerodynamic Surfaces**. Washington, 1956. 1 – 36 p.

LANDAU, L. D. On the problem of turbulence. **Doklady Akademii Nauk SSSR**, v. 44, p. 339–342, 1944.

LEHOUCQ, R. B.; SORENSEN, D. C. Deflation Techniques for an Implicitly Restarted Arnoldi Iteration. **SIAM Journal on Matrix Analysis and Applications**, v. 17, n. 4, p. 789–821, 1996. ISSN 0895-4798.

LELE, S. K. Compact finite difference schemes with spectral-like resolution. **Journal of Computational Physics**, v. 103, n. 1, p. 16–42, 1992. ISSN 00219991.

LI, N.; LAIZET, S. 2DECOMP & FFT-A Highly Scalable 2D Decomposition Library and FFT Interface. **Cray User Group 2010 conference**, p. 1–13, 2010.

LIEPMANN, H. W. Investigations on Laminar Boundary-Layer Stability and Transition on Curved Boundaries. **NACA Wartime Report W107 (ACR3H30)**, n. Naca Wartime Report - W109, p. 68, 1943. Available from Internet: <<http://hdl.handle.net/2060/19930093709>>.

LIGHTHILL, M. J. On Sound Generated Aerodynamically. I. General Theory. **Proceedings of the Royal Society A: Mathematical, Physical and Engineering Sciences**, v. 211, n. 1107, p. 564–587, mar 1952. ISSN 1364-5021. Available from Internet: <<http://rspa.royalsocietypublishing.org/cgi/doi/10.1098/rspa.1952.0060>>.

_____. On Sound Generated Aerodynamically. II. Turbulence as a Source of Sound. **Proceedings of the Royal Society A: Mathematical, Physical and Engineering Sciences**, v. 222, n. 1148, p. 1–32, feb 1954. ISSN 1364-5021. Available from Internet: <<http://rspa.royalsocietypublishing.org/cgi/doi/10.1098/rspa.1954.0049>>.

LIN, C. C. **The Theory of Hydrodynamic Stability**. [S.l.: s.n.], 1955. 155 p.

LIU, Q.; GÓMEZ, F.; THEOFILIS, V. Linear instability analysis of low- incompressible flow over a long rectangular finite-span open cavity. **Journal of Fluid Mechanics**, v. 799, p. R2, 2016. ISSN 0022-1120. Available from Internet: <http://www.journals.cambridge.org/abstract_S0022112016003918>.

MACK, C. J.; SCHMID, P. J. A preconditioned Krylov technique for global hydrodynamic stability analysis of large-scale compressible flows. **Journal of Computational Physics**, v. 229, n. 3, p. 541–560, 2010. ISSN 00219991.

MARTINEZ, A. **Towards natural transition in compressible boundary layers**. 2016. Tese (PhD. thesis) — University of São Paulo, 2016.

MARTINEZ, A.; MEDEIROS, M. F. Direct numerical simulation of a wavepacket in a boundary layer at Mach 0.9. In: **46th AIAA Fluid Dynamics Conference**. Reston, Virginia: American Institute of Aeronautics and Astronautics, 2016. v. 414, p. 1–33. ISBN 978-1-62410-436-7. ISSN 00221120. Available from Internet: <<http://arc.aiaa.org/doi/10.2514/6.2016-3195>>.

MCGREGOR, O. W.; WHITE, R. Drag of rectangular cavities in supersonic and transonic flow including the effects of cavity resonance. **AIAA Journal**, v. 8, n. 11, p. 1959–1964, nov 1970. ISSN 0001-1452. Available from Internet: <<http://arc.aiaa.org/doi/abs/10.2514/3.6032>>.

MERLE, X.; ALIZARD, F.; ROBINET, J.-C. Finite difference methods for viscous incompressible global stability analysis. **Computers and Fluids**, v. 39, n. 6, p. 911–925, 2010. ISSN 00457930. Available from Internet: <<http://dx.doi.org/10.1016/j.compfluid.2009.12.002>>.

MESEGUER-GARRIDO, F.; VICENTE, J. de; VALERO, E.; THEOFILIS, V. On linear instability mechanisms in incompressible open cavity flow. **Journal of Fluid Mechanics**, v. 752, p. 219–236, 2014. ISSN 0022-1120. Available from Internet: <http://journals.cambridge.org/abstract_S0022112014002535>.

ORR, W. M. F. The Stability or Instability of the Steady Motions of a Perfect Liquid and of a Viscous Liquid. Part II: A Viscous Liquid. **Proceedings of the Royal Irish Academy. Section A: Mathematical and Physical Sciences**, v. 27, p. 69–138, 1909.

OWEN, T. B. **Techniques of pressure fluctuation measurements**. [S.l.], 1958. 1 – 75 p.

PLUMBLEE, H. E.; GIBSON, J. S.; LASSITER, L. W. **Theoretical and Experimental Investigation of The Acoustic Response of Cavities In An Aerodynamic Flow**. [S.l.], 1962. 1–167 p.

PRANDTL, L. Motion of Fluids with Very Little Viscosity. In: **Internationalen Mathematiker-Kongresses**. Heidelberg: [s.n.], 1904. p. 1–8.

QADRI, U. A.; SCHMID, P. J. Frequency selection mechanisms in the flow of a laminar boundary layer over a shallow cavity. **Physical Review Fluids**, v. 2, n. 1, p. 013902, 2017. ISSN 2469-990X. Available from Internet: <<http://link.aps.org/doi/10.1103/PhysRevFluids.2.013902>>.

RADKE, R. J. **A Matlab Implementation of the Implicitly Restarted Arnoldi Method for Solving Large-Scale Eigenvalue Problems**. 1996. 100 p. Tese (Master Thesis) — Rice University, 1996.

RAYLEIGH, J. W. S. **The Theory of Sound. Vol. 1**. London: Macmillan and co., 1877. Available from Internet: <<http://hdl.handle.net/1908/3980>>.

_____. **The Theory of Sound. Vol. 2**. London: Macmillan and co., 1878. Available from Internet: <<http://hdl.handle.net/1908/3981>>.

_____. On the stability, or instability, of certain fluid motions. **Proceedings of the London Mathematical Society**, x, p. 57–72, 1879. ISSN 0024-6115. Available from Internet: <<http://onlinelibrary.wiley.com/doi/10.1112/plms/s1-11.1.57/epdf>>.

REYNOLDS, O. An Experimental Investigation of the Circumstances Which Determine Whether the Motion of Water Shall Be Direct or Sinuous, and of the Law of Resistance in Parallel Channels. **Proceedings of the Royal Society of London**, v. 35, p. 84–99, 1883.

_____. On the Dynamical Theory of Incompressible Viscous Fluids and the Determination of the Criterion. **Proceedings of the Royal Society of London**, 1894.

ROCKWELL, D.; NAUDASHER, E. Self Sustained Oscillations of Impinging Free Shear Layers. **Ann. Rev. Fluid Mech.**, v. 11, p. 67–94, 1979.

ROSHKO, A. **Some Measurements of Flow in a Rectangular Cavity**. [S.l.], 1955. 1 – 22 p.

ROSSITER, J. E. **Wind-tunnel experiments on the flow over rectangular cavities at subsonic and transonic speeds**. London, 1964. 1 – 36 p. Available from Internet: <<http://repository.tudelft.nl/view/aereports/uuid:a38f3704-18d9-4ac8-a204-14ae03d84d8c/>>.

ROWLEY, C. W.; COLONIUS, T.; BASU, A. J. On self-sustained oscillations in two-dimensional compressible flow over rectangular cavities. **Journal of Fluid Mechanics**, v. 455, p. 315–346, 2002. ISSN 0022-1120.

ROWLEY, C. W.; WILLIAMS, D. R. Dynamics and Control of High-Reynolds-Number Flow Over Open Cavities. **Annual Review of Fluid Mechanics**, v. 38, n. 1, p. 251–276, 2006. ISSN 0066-4189.

SCHLICHTING, H. Laminare Strahlausbreitung. **Z. angew. Math. Mech.**, v. 13, p. 260–263, 1933.

SCHLICHTING, H.; GERSTEN, K. **Boundary Layer Theory**. 8th. ed. [S.l.]: Springer-Verlag Berlin Heidelberg, 2000.

SCHREIBER, R.; KELLER, H. B. Drive cavity flows by efficient numerical techniques. **Journal of Computational Physics**, v. 49, n. 2, p. 310–333, 1983. ISSN 0021-9991/83/020310-24. Available from Internet: <<http://linkinghub.elsevier.com/retrieve/pii/0021999183901298>>.

SCHUBAUER, G. B.; SKRAMSTAD, H. K. Laminar boundary-layer oscillations and transition on a flat plate. **Journal of Research of the National Bureau of Standards**, v. 38, n. 2, p. 251, 1943. ISSN 0091-0635.

SIPP, D.; LEBEDEV, A. Global stability of base and mean flows: a general approach and its applications to cylinder and open cavity flows. **Journal of Fluid Mechanics**, v. 593, 2007. ISSN 0022-1120.

SOMMERFELD, A. Ein Beitrag zur hydrodynamischen Erkl  rung der turbulenten Fluessigkeitsbewegungen. In: **Proceedings of the 4th International Congress of Mathematicians**. [S.l.: s.n.], 1908. p. 116–124.

SUN, Y.; TAIRA, K.; CATTAFESTA, L. N.; UKEILEY, L. S. Spanwise effects on instabilities of compressible flow over a long rectangular cavity. **Theoretical and Computational Fluid Dynamics**, p. 1–11, nov 2016. ISSN 0935-4964. Available from Internet: <<http://link.springer.com/10.1007/s00162-016-0412-y>>.

_____. Biglobal instabilities of compressible open-cavity flows. **Journal of Fluid Mechanics**, v. 826, p. 270–301, sep 2017. ISSN 0022-1120. Available from Internet: <https://www.cambridge.org/core/product/identifier/S0022112017004165/type/journal_article>.

TAM, C. K. W. The acoustic modes of a two-dimensional rectangular cavity. **Journal of Sound and Vibration**, v. 49, n. 3, p. 353–364, 1976. ISSN 10958568.

TEZUKA, A.; SUZUKI, K. Three-dimensional global linear stability analysis of flow around a spheroid. **AIAA journal**, v. 44, n. 8, p. 1697–1708, 2006. ISSN 0001-1452. Available from Internet: <<http://arc.aiaa.org/doi/pdf/10.2514/1.16632>>.

THEOFILIS, V. Globally unstable basic flows in open cavities. **AIAA Paper**, v. 2000-1965, 2000. Available from Internet: <<http://arc.aiaa.org/doi/pdf/10.2514/6.2000-1965>>.

_____. On steady-state flow solutions and their nonparallel global linear instability. **Advances in turbulence VIII**, p. 35–38, 2000.

_____. Advances in global linear instability analysis of nonparallel and three-dimensional flows. **Progress in Aerospace Sciences**, v. 39, n. 4, p. 249–315, may 2003. ISSN 03760421. Available from Internet: <<http://linkinghub.elsevier.com/retrieve/pii/S0376042102000301>>.

_____. Global Linear Instability. **Annual Review of Fluid Mechanics**, v. 43, n. 1, p. 319–352, 2011. ISSN 0066-4189. Available from Internet: <<http://www.annualreviews.org/doi/suppl/10.1146/annurev-fluid-122109-160705>>.

THEOFILIS, V.; COLONIUS, T. An Algorithm for the Recovery of 2- and 3D BiGlobal Instabilities of Compressible Flow Over 2D Open Cavities. In: **33rd AIAA Fluid Dynamics Conference and Exhibit**. Reston, Virigina: American Institute of Aeronautics and Astronautics, 2003. ISBN 978-1-62410-095-6. Available from Internet: <<http://arc.aiaa.org/doi/10.2514/6.2003-4143>>.

TIETJENS, O. Beiträge zur Entstehung der Turbulenz. **Z. angew. Math. Mech.**, v. 5, p. 200–217, 1925.

TOLLMIE, W. Über die Entstehung der Turbulenz. In: **Nachrichten der Gesellschaft der Wissenschaften zu Göttingen**. Göttingen: [s.n.], 1929. p. 21–44.

_____. **The production of turbulence**. Washington, 1932. v. 609.

VICENTE, J. de; BASLEY, J.; MESEGUER-GARRIDO, F.; SORIA, J.; THEOFILIS, V. Three-dimensional instabilities over a rectangular open cavity: from linear stability analysis to experimentation. **Journal of Fluid Mechanics**, v. 748, p. 189–220, 2014. ISSN 0022-1120. Available from Internet: <http://www.journals.cambridge.org/abstract_S0022112014001268>.

VICENTE, J. de; RODRÍGUEZ, D.; THEOFILIS, V.; VALERO, E. Stability analysis in spanwise-periodic double-sided lid-driven cavity flows with complex cross-sectional profiles. **Computers and Fluids**, Elsevier Ltd, v. 43, n. 1, p. 143–153, 2011. ISSN 00457930. Available from Internet: <<http://dx.doi.org/10.1016/j.compfluid.2010.09.033>>.

WELLER, H. G.; TABOR, G.; JASAK, H.; FUREBY, C. A tensorial approach to computational continuum mechanics using object-oriented techniques. **Computers in Physics**, v. 12, n. 6, p. 620, 1998. ISSN 08941866. Available from Internet: <<http://scitation.aip.org/content/aip/journal/cip/12/6/10.1063/1.168744>>.

WILLIAMS, D. R.; ROWLEY, C. W. Recent Progress in Closed-Loop Control of Cavity Tones. **44th AIAA Aerospace Sciences Meeting and Exhibit**, 2006. Available from Internet: <<http://arc.aiaa.org/doi/abs/10.2514/6.2006-712>>.

YAMOUNI, S.; SIPP, D.; JACQUIN, L. Interaction between feedback aeroacoustic and acoustic resonance mechanisms in a cavity flow: a global stability analysis. **Journal of Fluid Mechanics**, v. 717, p. 134–165, feb 2013. ISSN 0022-1120. Available from Internet: <http://www.journals.cambridge.org/abstract_S0022112012005630>.